University of Strathclyde

Department of Mechanical & Aerospace Engineering

Molecular Dynamics Simulations of Liquid Flow in and Around Carbon Nanotubes

William David Nicholls

A thesis presented in fulfilment of the requirements

for the degree of Doctor of Philosophy

2012

Declaration of author's rights

This thesis is the result of the author's original research. It has been composed by the author and has not been previously submitted for examination which has led to the award of a degree.

William D. Nicholls

January 2012

Abstract

The advent of carbon nanotube (CNT) synthesis has created exciting new opportunities in fluid dynamic applications as the fluid behaviour can deviate significantly from conventional continuum expectations. CNTs indicate major potential in nanotechnologies such as seawater desalination. Molecular dynamics (MD) is often the numerical method of choice for fluid dynamics at the nanoscale due to its high level of detail and accuracy.

Using the "controllers" of Borg *et al.*[1], we are able to shrink the computational domain required for molecular dynamic simulations of the external flow of liquid argon past a CNT and significantly increase the simulation's computational efficiency. We apply three pressure differences across a CNT membrane carrying liquid argon, and compare the results of the pressure-driven flow through the nanotube with hydrodynamic predictions and Navier-Stokes solutions. We find that both fail to accurately predict flow behaviour in this problem.

Non-equilibrium molecular dynamics simulations are then used to investigate water transport through (7,7) CNTs, investigating how changing the CNT length affects the internal flow dynamics. We show that, under the same applied pressure difference, an increase in CNT length has a negligible effect on the resulting mass flow rate and fluid flow velocity. Axial profiles of fluid properties demonstrate that entrance and exit effects are significant in the transport of water along CNTs. Large viscous losses in these entrance/exit regions lead into central "developed" regions in longer CNTs where the flow is effectively frictionless.

Finally, we investigate how changing the number of structural defects in the

wall of a (7,7) single-wall carbon nanotube (CNT) affects the water transport and internal fluid dynamics. Structural defects are modelled as vacancy sites (missing carbon atoms). We find that, while fluid flow rates exceed continuum expectations, increasing numbers of defects lead to significant reductions in fluid velocity and mass flow rate. The inclusion of such defects disrupts the nearly-frictionless water transport commonly attributed to CNTs.

The results presented in this thesis are crucial in the development of future nanotechnologies such as CNT membranes for selective material separation.

Acknowledgements

First and foremost I would like to thank my supervisor, Professor Jason Reese, for his unconditional support throughout my PhD and also during my undergraduate studies. I am grateful for all of the guidance and knowledge that he has given me.

I am truly indebted to Dr Matthew Borg who has been a constant source of support and inspiration. The help which he has provided has proven to be invaluable and I am sincerely grateful.

I recognise, and am thankful for, the financial support of the EPSRC and the Institution of Mechanical Engineers (IMechE). The IMechE have supported me throughout my entire time at university and I am indebted to them.

Finally, I would like to thank my friends and family, who mean more to me than anything. This work would not have been possible without their love, support and words of encouragement and I dedicate this thesis to them.

Contents

List of Figures

List of Tables

Nomenclature

A	cross-sectional area
$\mathbf{a}$	molecule acceleration
a_{cc}	carbon bond length
$\mathbf{a_1}, \mathbf{a_2}$	chiral unit vectors
$\mathbf{C_h}$	chiral vector
d	number of degrees of freedom
D	diameter
e_p	pressure error
E	statistical error
E	Young's modulus
E_s	smoothing function
$\mathbf{f}$	molecule force vector
H	hydrogen bonds
$\mathbf{I}$	moment of inertia
i, j	arbitrary pair of molecules
k_b	Boltzmann constant
K	gain term
l	bond length
L	length
L_s	slip length
(n, m)	chiral indices
m	molecule mass

N	number of molecules
N_s	number of sites
$\hat{\mathbf{n}}$	normal unit-vector
p	probability
P	normal pressure
ΔP	pressure difference
q	charge
$\mathbf{r}$	position vector
r_c	potential cut-off radius
r_m	radius of nanotube in membrane
R	radius
S	number of measurement samples
T	temperature
$\mathbf{T}$	translational vector
t_m	membrane thickness
t	time
Δt	time interval
U	potential energy
$\mathbf{u}$	bulk velocity
$\mathbf{v}$	molecule velocity
V	volume
x, y, z	spatial Cartesian co-ordinates

Greek

α	adjustable controller parameter
β	relaxation parameter
γ	ratio of specific heats
ϵ	Lennard-Jones well-depth
ϵ_f	enhancement factor

ϵ_0	electric constant
θ	chiral angle
θ, ϕ	bond angles
λ	relaxation parameter
μ	dynamic viscosity
ρ	mass density
σ	characteristic length scale
$\boldsymbol{\sigma}$	stress tensor
σ_{yield}	yield stress
τ	torque
τ_q	autocorrelation time
τ_t	time constant
ϕ	water dipole orientation angle
χ	molecule velocity scaling parameter
$\boldsymbol{\omega}$	molecule angular velocity

Superscripts

cor	correction
ext	external
o	old
n	new
req	required (target) value
rot	rotational component
$trans$	translational component

Subscripts

a, b	site indices
av	average
b	bin
C	Coulomb
cz	control zone
d	derivative
f	arbitrary face
i	integral
i, j	pair of molecule indices
k	time index
m	molecular
n	new time
p	proportional
P	arbitrary cell
r	rotational
R	sampling region
s	sample
sz	sampling zone
t	translational
x, y, z	spatial Cartesian co-ordinates

Acronyms

ADF	Axial Distribution Function
AICA	Arbitrary Interaction Cells Algorithm
BC	Boundary Condition
CFD	Computational Fluid Dynamics

CNP	Carbon Nanopipe
CNT	Carbon Nanotube
CPU	Central Processing Unit
CVD	Chemical Vapour Deposition
DD	Domain Decomposition
DSMC	Direct Simulation Monte Carlo
DWNT	Double-Wall Nanotube
GPU	Graphical Processing Unit
HMM	Heterogeneous Multiscale Method
LJ	Lennard-Jones
MD	Molecular Dynamics
MWNT	Multi-Wall Nanotube
NPBC	Non-Periodic Boundary Condition
NS	Navier-Stokes
PBC	Periodic Boundary Condition
PID	Proportional-Integral-Derivative
RDF	Radial Distribution Function
RPM	Reflective Particle Membrane
SWNT	Single-Wall Nanotube
WCA	Wetting Contact Angle

Chapter 1

Introduction

1.1 Motivation

In this thesis we investigate computationally the remarkable behaviour of fluids at the nanoscale. Nanoscale fluid dynamics is the study of fluid flows at a length scale below ∼100 nm [7, 8]. The development of advanced fabrication techniques, which enable the manufacturing of nanosized devices, has resulted in a rapid growth of the study of fluid dynamics at this scale [9].

Numerical modelling plays a crucial role in nanoscale fluid dynamics because physical experiments are often difficult to perform accurately and obtaining the necessary instrumentation can be very expensive. Computer simulation provides a cheap, detailed alternative to experiments. Mathematical models are used to predict what would happen in reality and provide a level of detail that is very often unattainable by experiments. An example of this is measuring fluid velocity profiles in a nanotube only a few nanometers in diameter; this is currently not possible in physical experiments but, by using an appropriate numerical approach, we can extract this particular profile with reasonable ease. The level of reliability of a computer simulation tool is measured by comparing results with available experimental data and benchmark cases. Based upon this comparison, the computational method (numerical procedure or physical model) may have to

be improved to obtain the desired accuracy and/or detail.

It is now widely accepted that the fundamental properties of a fluid can be significantly altered under extreme confinement [10, 11]. This thesis focuses on computational modelling of liquid flows at the nanoscale, more specifically, where hydrodynamic predictions fail to accurately predict fluid behaviour and we must rely upon atomistic simulation techniques such as molecular dynamics (MD).

Nanoscale technologies are currently addressing important issues in energy, environment, health, and transport. Examples of these are:

- superhydrophobic surfaces [12] could lead to more energy efficient ships and aircraft by reducing skin friction drag;
- lab-on-a-chip devices [13, 14] are extremely small scale systems that will help to bring cheap and efficient health care to everyone by reducing costs for faster disease detection and treatment;
- efficient nanotube membranes for water purification and desalination [15, 16];
- nanofiltration to separate uranium from seawater [17];
- advanced cooling systems for electronic circuits [9];
- sensitive flow sensors [18].

The majority of these applications use carbon nanotubes (CNTs). These rolled sheets of graphene have attracted major research and development attention since their rediscovery in 1991, and their impressive fluid transport properties feature strongly in this thesis. A full description of CNTs can be found in Chapter 2.

In the remainder of this chapter we provide an outline of this thesis and a description of MD, including the software which we use throughout this work.

1.2 Thesis outline

In Chapter 2 we discuss the properties of CNTs and how they are manufactured. The manufacturing of CNT membranes is also described. A review of recent experimental work investigating water flow through carbon nanostructures is presented, and the CNT defects which can occur during manufacturing are introduced. Finally, a novel method for generating CNTs in an MD simulation is described.

A review of MD simulations of water transport through CNTs is presented in Chapter 3. We discuss a variety of water models and interaction parameters which are used throughout the literature and their effect on simulation results. The relationship between CNT diameter, fluid structure, flow rate and hydrogen bonding is also discussed.

Measurement techniques for polyatomic molecules which have been implemented in our MD solver are described in Chapter 4. These techniques build on the measurement framework created by Borg [19]. The role of boundary conditions in MD is then discussed, with a focus on studies of liquid flow through nanotubes. Novel boundary conditions for generating pressure-driven flow for such problems are introduced.

In Chapter 5 we investigate two nanoscale fluid dynamics problems using MD simulation: a CNT in uniform fluid cross-flow, and fluid flow through a CNT membrane. The aim of the first case is to investigate the performance of our new boundary conditions and the improvement in computational efficiency which can be achieved. The second set of simulations allows us to study the behaviour of a simple fluid under extreme confinement. The accuracy of corresponding hydrodynamic predictions is assessed, and the effect of changing the molecular interaction parameters is investigated.

In Chapter 6 we focus on pressure-driven water transport in CNTs using MD simulation. First, we evaluate the effect that changing the length of a defect-free (7,7) CNT has on the fluid transport along it. By looking at fluid properties,

such as water density distributions and pressure profiles along the CNTs, we draw conclusions about the fundamental transport mechanisms of water inside small-diameter CNTs. In the later part of this chapter, vacancy site defects are included into the wall of a (7,7) CNT, in order to understand what effect this has on the contained fluid behaviour.

The main findings of this research and a discussion of how the work can be advanced in the future are presented in Chapter 7.

1.3 Molecular dynamics

Molecular dynamics (MD) is the study of a system of simulated atoms or molecules that interact with one another via specified intermolecular potentials. These potentials represent the attractive and repulsive forces between molecules (with no net electrical charge) known as Van der Waals interactions. The movement of each molecule in the system is described by the classical equations of motion, i.e. Lagrangian or Hamiltonian mechanics. When modelling a simple molecule, i, which has no rotational or internal degrees of freedom, the classical equations produce the following form of Newton's second law of motion [20]:

$$m_i \mathbf{a}_i = \mathbf{f}_i, \tag{1.1}$$

where $\mathbf{f}_i$ is the total force acting on molecule i, and m_i and $\mathbf{a}_i$ are the atomic mass and acceleration, respectively.

The force between two molecules, $\mathbf{f}_{ij}$, is calculated by differentiating the intermolecular potential, which is a function of their separation in space, r_{ij}:

$$\mathbf{f}_{ij} = -\nabla U(r_{ij}). \tag{1.2}$$

The most commonly-used potential to describe Van der Waals interactions be-

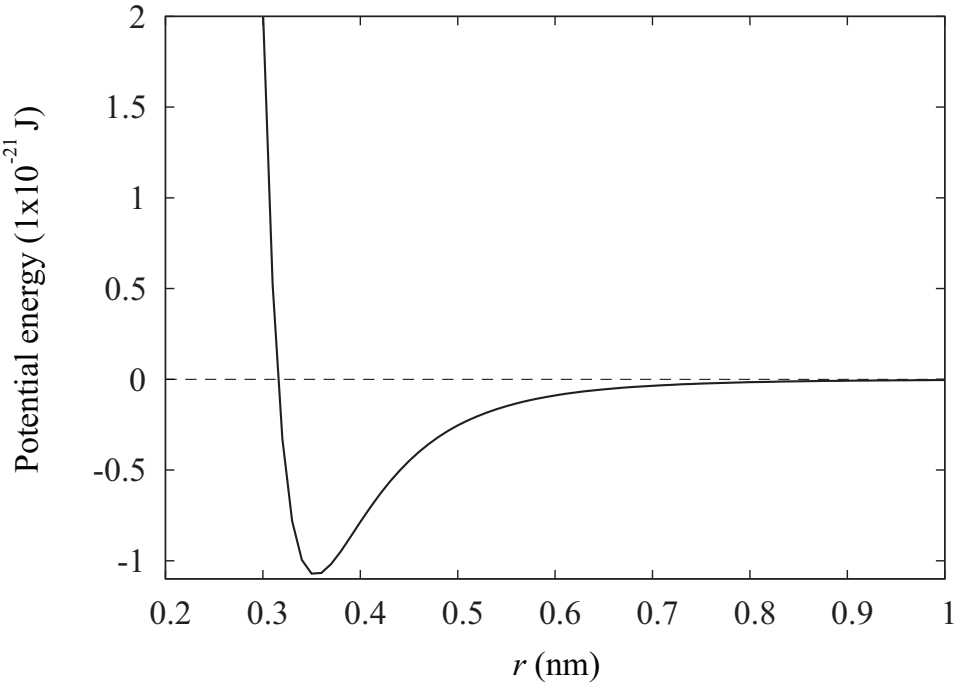

Figure 1.1: A Lennard-Jones interaction potential.

tween non-bonded molecules is the Lennard-Jones (LJ) potential:

$$U(r_{ij}) = 4\epsilon_{ij}\left(\left(\frac{r_{ij}}{\sigma_{ij}}\right)^{-12} - \left(\frac{r_{ij}}{\sigma_{ij}}\right)^{-6}\right), \tag{1.3}$$

where ϵ_{ij} is the well-depth and σ_{ij} is the collision diameter and corresponds to where the potential energy is zero. The collision diameter is based upon the Van der Waals radii of the interacting molecules. The potential is repulsive at small molecular separations and is attractive at long separations; potential energy is zero for infinite separation lengths. The shape of this potential is shown in Fig. 1.1 (where the parameters for an oxygen-oxygen interaction are used). Results from MD simulations of fluids interacting through the LJ potential have demonstrated good agreement with experimental data [21].

The net force on an individual molecule, $\mathbf{f}_i$, is the sum of all pair interactive

forces between the molecule and its N neighbours:

$$\mathbf{f}_i = \sum_{\substack{j=1 \\ j \neq i}}^{N} \mathbf{f}_{ij}. \tag{1.4}$$

A cut-off radius, r_c, is most often applied to each molecule to reduce the computational demand of the MD simulation by only allowing molecules to interact with other molecules that reside in a spherical volume defined by the cut-off radius. The equations of motion are integrated numerically using an integration algorithm, e.g. the Verlet Leapfrog scheme [22], to obtain molecule velocities and positions from their accelerations.

When simulating polyatomic molecules there is an increase in the number of molecular degrees of freedom as the molecules then possess angular momentum. To simulate polyatomic molecules, we use the symplectic splitting method of Dullweber *et al.* [23]. This models molecules as fully rigid structures that are composed of point masses, referred to as sites, which represent the individual atoms. Intramolecular interactions are neglected as the site positions are fixed and cannot move relative to one another.

The integration of each molecule is then split into two parts: translational displacement and rotational operations. Interactions between sites of one molecule and another are treated as before, and are only a function of their separation distance (and of course the interaction type). So for a polyatomic molecule, the total intermolecular force, $\mathbf{f}_i$ acting upon it is the sum of the net force of each intramolecular site:

$$\mathbf{f}_i = \sum_{a=1}^{N_s} \mathbf{f}_a, \tag{1.5}$$

where $\mathbf{f}_a$ is the total force acting on site a and N_s is the total number of sites. Translational displacement is performed by moving the centre of mass of the rigid molecule using the total force and its total mass (the sum of the individual site masses), the same as for monatomic molecules.

The rotation of a rigid polyatomic molecule is based upon the total torque acting about its centre of mass. The contribution of each site torque is calculated by multiplying the net site force by its distance from the centre of mass, r_{ia} i.e.

$$\boldsymbol{\tau}_a = \mathbf{f}_a \cdot r_{ia}. \tag{1.6}$$

Therefore the total torque acting on molecule i is:

$$\tau_i = \sum_{a=1}^{N_s} \boldsymbol{\tau}_a. \tag{1.7}$$

The total torque is then used to update the angular momentum of the molecule. A number of consecutive rotations of the molecule are performed, using its angular momentum. A full description of this technique, including instructions on its implementation in an MD solver, is available in [23].

MD can also incorporate intramolecular potentials, which represent bond stretching, bending and torsion. However, with this new level of detail comes greater computational demand as the time step size must be reduced to capture the bond dynamics. Molecules are often modelled as rigid to improve the efficiency of the MD simulation; whether or not this affects the accuracy of the simulation overall is problem-specific.

The SHAKE algorithm [24] is a popular alternative to the method described above. This technique moves all atoms of a molecule independently and then performs a number of corrections to the atom positions to ensure bond lengths and angles remain constant. The computational time associated with this iterative procedure can be significant and comes with additional complexity (in the solution of nonlinear systems). The splitting technique has been shown to conserve linear and angular momentum and remains stable over long time periods, providing an alternative, efficient rigid body scheme.

1.3.1 Molecule interactions using OpenFOAM

All MD simulations presented in this thesis are performed using OpenFOAM [25], which incorporates an MD solver known as *mdFoam*. This code is fully parallelised and can perform MD simulations in arbitrary, complex, 3D geometries [26, 27]. The MD code is based upon the Arbitrary Interacting Cells Algorithm (AICA) [27].

The MD simulation domain is split into numerical mesh cells, similar to conventional computational dynamics. The AICA uses a direct interaction list (DIL) to store a list of cells that must interact with other cells based on their cut-off radii. Molecules must interact with other molecules that reside in their cell, and the cells which are present on the DIL. The advantage of this method is that the DIL is only built once at the start of the simulation and remains valid throughout the simulation (assuming the mesh is static). Molecules always know which cell they reside in – this was adapted from OpenFOAM's particle tracking method [26] and was one of the main reasons for choosing to implement an MD solver in OpenFOAM.

1.3.2 Electrostatics

When simulating ionic or polar molecular systems, long-range electrostatic interactions must be accounted for, e.g. by the Coulomb potential:

$$U_C(r_{ij}) = \frac{1}{4\pi\epsilon_0}\frac{q_i q_j}{r_{ij}}, \tag{1.8}$$

where ϵ_0 is the electric constant and q_i and q_j are the charges of molecules i and j, respectively. The use of simple truncation (cut-off radius) methods is not recommended for systems which contain ions, as the electrostatic interaction potential decays slowly (r^{-1}). Ideally the method for computing electrostatic interactions should be no more computationally demanding than simple truncation schemes but should possess greater accuracy. For periodic systems, electrostatic interac-

tions are handled using lattice sum methods [28–31], which split the interaction into short range and long range parts. These techniques are implemented in many available MD solvers such as NAMD [32], LAMMPS [33], and Amber [34], but are not currently available in OpenFOAM. Short-range interactions are evaluated directly using molecule separation distances and the long-range part is calculated in Fourier space over all period images. The implementation of such techniques is complicated, increases the computational cost of an MD simulation, and they are restricted to fully periodic simulations. However, if the simulated system contains only water (which is polar but overall charge neutral) then we can truncate the electrostatic interaction without significantly affecting the dynamics of the system [35].

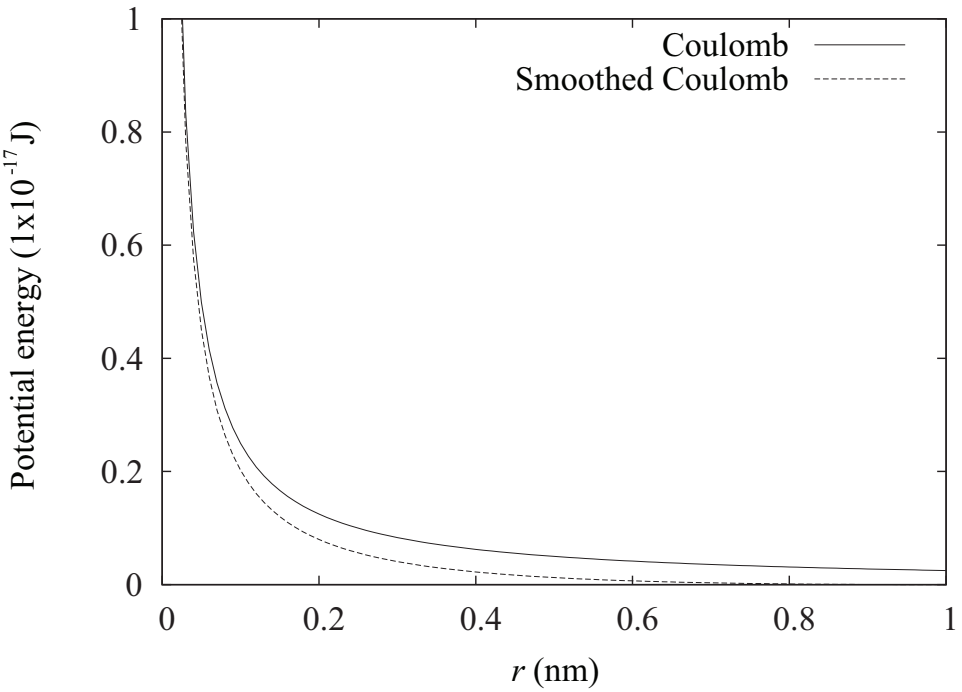

Figure 1.2: Original and smoothed Coulomb interaction potentials.

When performing simulations involving water molecules (without ions) we use the truncated, smoothed Coulomb potential:

$$U_C(r_{ij}) = \frac{1}{4\pi\epsilon_0}\left(\frac{q_i q_j}{r_{ij}} - E_s(r_{ij})\right), \tag{1.9}$$

where $E_s(r_{ij})$ is a smoothing function of the form:

$$E_s(r_{ij}) = \frac{q_i q_j}{r_c} - (r_{ij} - r_c)\frac{q_i q_j}{r_c^2}. \tag{1.10}$$

The original and smoothed Coulomb potentials are shown in Fig. 1.2. By using the smoothing function we ensure that there is no discontinuity in the potential energy at the cut-off which can introduce errors [36]. The choice of cut-off radius truncation can have a significant effect on an MD simulation and bad choices of it can lead to artifacts such as unexpected water layer formation [36], however it is accepted that a value of $\sim$1 nm is adequate.

1.4 Hybrid methods

Many of the simulation techniques (e.g. pressure boundary conditions) detailed in this thesis are derived from or inspired by hybrid methods and it is only right to briefly describe them here. The advantage of using a hybrid approach at the nano and microscales is that it combines the detail and accuracy of MD with the computational efficiency of a less detailed approach. A hybrid method uses two or more numerical descriptions in the same simulation domain, e.g. MD coupled with a computational fluid dynamics (CFD) solver.

Hybrid solvers generally use a combination of MD and CFD for liquids, but MD and direct simulation Monte Carlo (DSMC) have also been coupled for simulating gas flows [37]. The aim of this approach is to accurately capture gas-surface interactions by explicitly modelling the wall as molecules rather than using an implicit DSMC boundary condition.

Classically, the different solvers would be spatially discretised with each being responsible for separate parts of the domain [38–40], this type of hybrid technique is known as domain decomposition (DD). The DD method decouples the length scale of the problem but not the time scale, meaning that the MD and continuum solvers must advance in time by the same amount. This restricts the application

of the technique to small scale (both length and time) systems.

A second, less common hybrid technique is the heterogeneous multiscale method (HMM) [41]. The HMM solves the entire flow domain using CFD but applies small MD domains at the nodes and/or faces of the CFD mesh. The HMM is both spatially and temporally decoupled, which enables it to be used for larger scale systems than the DD technique.

While both of these hybrid techniques are different in application, they both include communication between an atomistic and a continuum solver in order to exchange boundary condition information. It is through the exploitation of the CFD to MD communication that we are able to improve existing boundary conditions for full MD simulations, as will be described in Chapter 4.

1.5 Project Objectives

In this thesis, we aim to increase understanding of fluid dynamic behaviour at the nanoscale using molecular dynamics, in particular water transport through CNTs. In addition, an important objective of this work is to improve the way in which nanoscale fluid problems are modelled using MD, e.g. users must be able to apply continuum-like boundary conditions in nanofluidic systems to enable real engineering problems to be solved. MD simulations of water transport through CNTs must be able to be simulated using OpenFOAM as the computational tool, this is of particular importance for future developments of the OpenFOAM which will enable hybrid MD-CFD simulations to be performed using water as the working fluid.

1.6 Key Developments

The MD code within OpenFOAM was created originally by Macpherson [42] and further developed by Borg [19] in recent years. Additional contributions to the MD code have been made throughout this work to enable simulations involving

CNTs and pressure driven flow of polyatomic liquids. These developments permitted OpenFOAM to be used to investigate liquid argon flow in and around CNTs and water transport through (7,7) CNTs with and without structural defects. The main contributions of this work are outlined below.

- Development of a parallelised, pre-processing tool which can create multiple CNTs of any size and structure within the OpenFOAM environment.
- Significant increase in computational efficiency of an MD simulation of liquid argon flow past a CNT using the continuum-like boundary conditions of Borg [19].
- A detailed analysis of liquid argon flow through 2 nm diameter CNTs which is compared with previously published results using a Navier-Stokes solver. Results from the MD simulations highlight the limitations of continuum-based solutions at the nanoscale and demonstrate that lower interaction energies between the liquid and surface result in less fluid resistance and higher flow rates.
- The measurement framework and boundary conditions developed by Borg [19] for monatomic fluids has been extended to include polyatomic, polar fluids, such as water.
- MD simulations of pressure driven water flow through (7,7) CNTs were performed to assess what role CNT length plays in the transport mechanism.
- Modification of the CNT pre-processing tool to enable the user to model CNTs with any number of vacancy site defects at random locations along the length of the CNT.
- MD simulations of pressure driven water flow through (7,7) CNTs with increasing numbers of vacancy site defects were performed to better understand what effect their presence has on the water transport mechanism.

1.7 Published papers

The work from this thesis has contributed to the following published research papers:

1. William D. Nicholls, Matthew K. Borg and Jason M. Reese, Molecular dynamics simulations of liquid flow in and around carbon nanotubes, *ASME 8th International Conference on Nanochannels, Microchannels, and Minichannels Proceedings*, August 2010, Montreal, Canada.

2. Matthew K. Borg, William D. Nicholls and Jason M. Reese, MD boundary conditions for pressure gradient flows: nano-mixing and nano-droplet deformation in extensional flows, *NSTI Nanotech Conference*, June 2010, Anaheim, CA, USA.

3. Matthew K. Borg, William D. Nicholls and Jason M. Reese, Hybrid molecular dynamics and navier-stokes method in complex nanoflow geometries, *NSTI Nanotech Conference*, June 2010, Anaheim, CA, USA.

4. William D. Nicholls, Matthew K. Borg and Jason M. Reese, Simulating the fast transport of water through carbon nanotubes, *NSTI Nanotech Conference*, June 2011, Boston, MA, USA.

5. Jason M. Reese and William D. Nicholls, Perspectives on the simulation of micro gas and nano liquid flows, *ASME 9th International Conference on Nanochannels, Microchannels, and Minichannels Proceedings*, June 2011, Alberta, Canada.

6. William D. Nicholls, Matthew K. Borg, Duncan A. Lockerby and Jason M. Reese, Water transport through (7,7) carbon nanotubes of different lengths using molecular dynamics, *Microfluidics and Nanofluidics*, 12:257-264, 2012.

7. William D. Nicholls, Matthew K. Borg, Duncan A. Lockerby and Jason M. Reese, Simulating water transport through carbon nanotubes with defects, *Molecular Simulation*, *accepted*, 2012.

Chapter 2

Carbon Nanotubes

2.1 Properties and synthesis

Carbon nanotubes (CNTs) are tubular structures with nanoscale diameters that can be up to centimetres in length, giving these structures extreme aspect ratios. CNTs can be thought of as rolled-up sheets of graphene, that possess a two dimensional honeycomb lattice arrangement of carbon atoms. Due to the numerous ways one can roll a two dimensional sheet, many different CNT surface structures can exist (CNTs are not in fact manufactured by rolling graphene, but this image is used to classify CNTs, and for visualisation purposes).

CNTs can be created as single-wall nanotubes (SWNTs), where there is only one nanotube with a wall thickness of one atom, or multi-wall nanotubes (MWNTs), where there are up to hundreds of concentric carbon shells comprising the structure. The majority of literature sources attribute the discovery of carbon nanotubes (MWNTs) to Iijima [43], although the original discovery has recently been traced back to two Soviet scientists from the 1950s whose work was unknown outside of Russia at the time [44]. SWNTs were first manufactured by Iijima in 1993 [45].

CNTs possess exceptional mechanical (high Young's modulus and tensile strength), electrical (high electrical conductivity), and thermal (high thermal conductiv-

ity) properties [46, 47], which has led to a wide variety of applications proposed for CNTs. They possess a pristine, nonpolar, hydrophobic inner surface which many believe is responsible for the outstanding fluid transport properties that have made them a significant contributor to the research and technology field of nanofluidics.

CNTs can have a high structural perfection [48] and SWNTs are classified by a chiral vector:

$$\mathbf{C_h} = (n, m) = n\mathbf{a}_1 + m\mathbf{a}_2, \tag{2.1}$$

where n and m are integers ($n \geqslant m$), and $\mathbf{a}_1$ and $\mathbf{a}_2$ are the chiral unit vectors. There are three types of CNTs: armchair ($n = m$), zigzag ($m = 0$), and chiral (any other values of n and m). The type of CNT is defined by the angle a graphene sheet would have to be rolled to obtain that particular atomistic arrangement, as shown in Fig. 2.1. This angle is known as the chiral angle θ and its relationship with CNT structure and chiral vector is shown in Table 2.1 and calculated using:

$$\sin\theta = \frac{\sqrt{3}m}{2\sqrt{n^2 + m^2 + nm}} \tag{2.2}$$

The three different types of CNT are illustrated in Fig. 2.2. The diameter of a CNT can be calculated using the chiral vector:

$$D = \frac{|\mathbf{C_h}|}{\pi} = \frac{a_{cc}\sqrt{3(n^2 + m^2 + nm)}}{\pi}, \tag{2.3}$$

where a_{cc} is the carbon bond length, which is 0.142 nm [44].

n	m	Structure	Chiral Angle θ (deg)
5	0	Zigzag	0
5	5	Armchair	30
6	3	Chiral	$0 < \theta < 30$

Table 2.1: Examples of different CNT structures and their corresponding chiral angles.

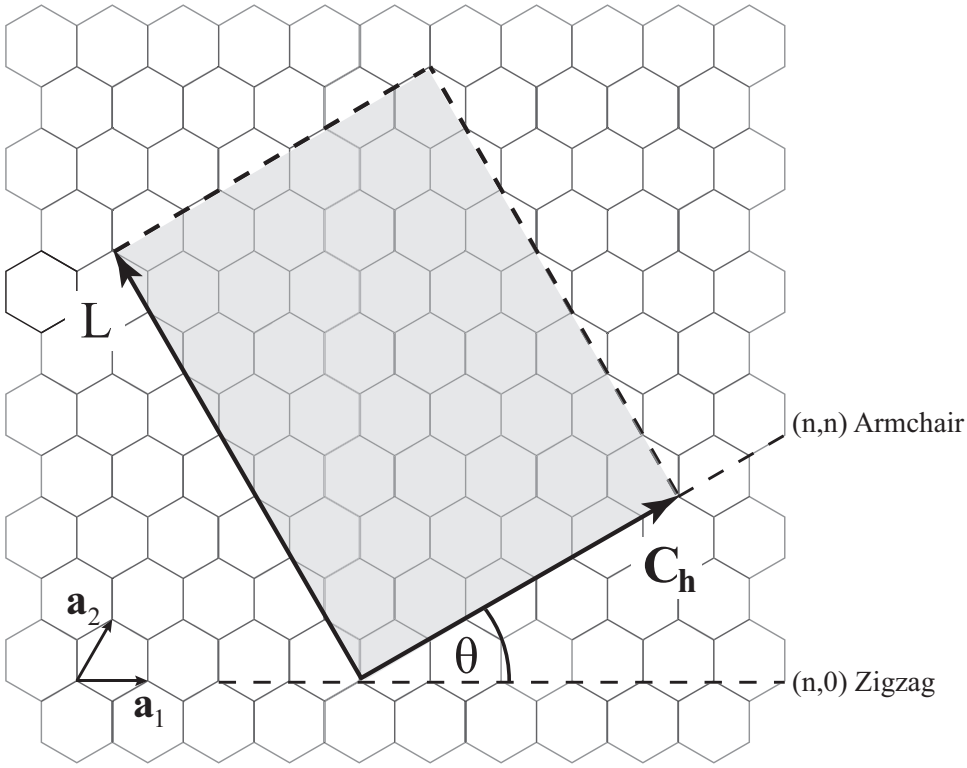

Figure 2.1: Graphene sheet with an unrolled armchair CNT shown by the grey highlighted area. L is the length of the CNT, and the chiral vector $\mathbf{C_h}$ makes the circumference of the nanotube. The chiral unit vectors, $\mathbf{a}_1$ and $\mathbf{a}_2$, are also illustrated.

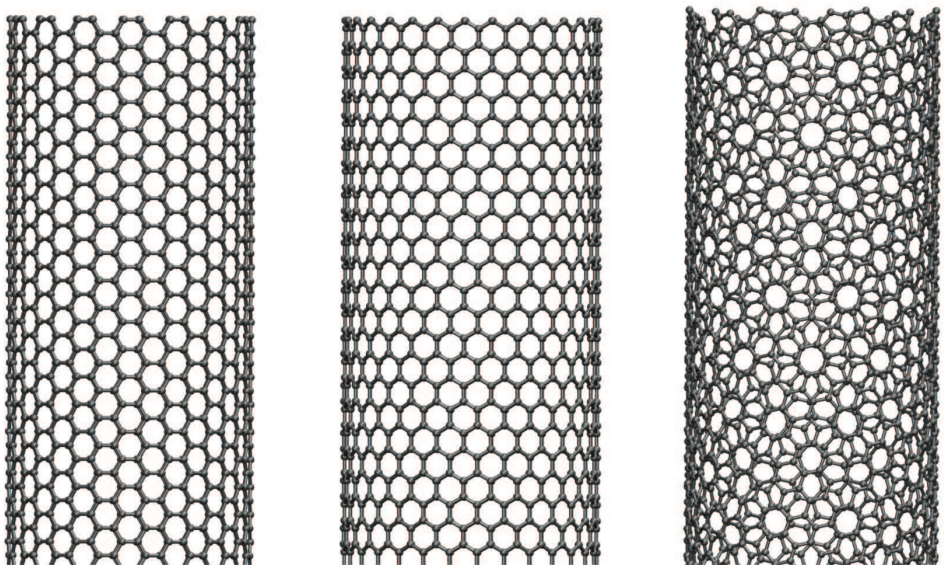

Figure 2.2: The three types of CNTs: armchair (16,16), zigzag (29,0), and chiral (22,10) which were created using OpenFOAM. These names are derived from the carbon arrangement which is most clearly demonstrated at the CNT inlet/outlet.

The structure and properties of CNTs are determined by the method of synthesis and pre/post treatment techniques. The synthesis process is the most challenging aspect of carbon nanotube research, as there is no single method that provides control over CNT chirality, growth direction and length [49, 50]. According to Joselevich *et al.* [49], the four main challenges in CNT synthesis are:

- mass production - requiring low-cost, large scale processes;
- selective production - synthesising nanotubes with the required structure (chirality);
- organisation - better control over the location and orientation of synthesised nanotubes;
- growth mechanism - greater understanding of how nanotubes grow during the synthesis procedure, e.g. whether tip or base growth is the dominant mechanism.

The three main methods of CNT production are: arc discharge, laser ablation, and chemical vapour deposition (CVD) [49, 51]. Defects present in the CNTs created during the synthesis process can have a significant effect on the properties of the nanotubes, therefore it is important to use a method or treatment which minimises or controls the production of such defects. CNT defects are discussed in Section 2.4.

Arc discharge

This method depends on the condensation of hot gaseous carbon atoms generated by the vaporisation of a graphite rod. Two high-purity graphite rods are used as electrodes, one as the anode and the other as the cathode. A direct current is supplied to the graphite rods and they are brought close enough together that arcing occurs in a helium atmosphere. The carbon atoms of the anode

are vaporised (at ∼3000°C) and deposit on the cathode, forming multi-walled nanotubes (MWNTs) and graphitic particles. This was the method used by Iijima in 1991 for his "discovery" of multi-wall carbon nanotubes. Iijima's discovery of single wall carbon nanotubes in 1993 was through using arc discharge with the addition of an iron catalyst. The SWNTs were formed as part of a bundle and had diameters ∼1 nm. Other metal catalysts often used are cobalt and nickel.

Laser ablation

This method is also based on the vaporisation of solid carbon (pure graphite). High-power lasers are used to heat a furnace to the required temperature (1200°C) to cause vaporisation of the graphite. To produce SWNTs, a mixture of graphite and metal catalysts are used. Both the arc discharge and laser ablation methods can yield large quantities of SWNTs but suffer from the same drawbacks: production cost is very high which makes mass production very expensive, and nanotubes are created as part of a bundle. Ordered structures have not yet been created using these methods.

Chemical vapour deposition (CVD)

This method involves the decomposition of carbon compounds, e.g. hydrocarbons, using metal catalysts that provide sites for the initiation of nanotube growth at temperatures below 1000°C. This method has become one of the most popular in the synthesis of MWNTs and SWNTs due to its high efficiency and purity of the nanotubes produced [51, 52]. High quality, vertically-aligned MWNTs and SWNTs can be grown on silicon wafers patterned with a metal catalyst [47], where the choice of catalyst determines whether multi-wall or single-wall nanotubes are produced. The CVD method is well developed and provides greater control over the structure of the synthesised CNTs (chirality). Other reasons for this method's popularity are: it can produce individual CNTs which are not tangled as part of a bundle; and it is easier to scale up production to industrial levels [47, 49]. There

are many different synthesis methods which are based on CVD e.g. high-pressure catalytic decomposition of carbon monoxide (HiPCO). These methods differ by the choice of catalyst and/or type of feed gas and have their own advantages, e.g. high production rate and increased purity, and disadvantages e.g. higher production costs. The mass production of MWNTs by CVD methods appears to be relatively straightforward, whereas SWNTs have more limitations during the synthesis procedure, e.g. restricted growth time, which reduces their production rate [49].

2.1.1 Post synthesis

Once the CNTs have been produced, the sample must be treated to remove any impurities or unwanted products of the synthesis procedure e.g. catalysts, amorphous carbon, etc. There are many purification techniques such as gas-phase oxidation (dry method) to remove amorphous carbon, which is more reactive than the carbon in a nanotube, and acid treatment (wet method) to dissolve the catalyst used during synthesis.

All synthesis techniques produce a mixture of nanotubes of different chiralities, so a sorting stage is required to separate the nanotubes into particular ensembles. Techniques such as size-exclusion chromatography can be used to sort nanotubes based on length, filtration based on electronic type, and electrophoresis to sort nanotubes depending on their diameter [49].

Some synthesis procedures can produce carbon structures that are amorphous and do not possess the honeycomb surface structure of graphene: these nanoscale structures are referred to as carbon nanopipes (CNPs). The fluid transport properties of carbon nanopipes are different from those of carbon nanotubes and is discussed below. An annealing procedure can be used to reduce the amorphous surface structure of CNPs: nanopipes are placed in an inert atmosphere at $\sim$2000°C and during this process the carbon in the pipes' walls graphitise to form surface structures that appear to be more like those of carbon nanotubes [53]. Mattia *et*

al. [53] demonstrated that the wetting characteristics of the nanopipe changed after the annealing process making them more hydrophobic: the wetting contact angle increased linearly with annealing temperature, from 44° to 77°.

2.2 CNT membranes

CNT membranes are formed by embedding aligned CNTs in a polymer or ceramic material through a variety of complex processes including catalytic CVD CNT synthesis. These membranes have a huge potential in selective material separation, with one of the most promising applications being sea water desalination. The most common desalination method currently being used at industrial scales is reverse osmosis. This technique involves forcing sea water through a semipermeable membrane that allows the passage of water but not salt ions. Reverse osmosis comes with very high associated costs due to the large pressure gradients required to overcome the osmotic pressure of seawater, see Fig. 2.3. Membranes used in the desalination process must remove at least 95% of the salt from the seawater for it to be fit for human consumption. CNT membranes have been proposed to replace the current polymer membranes to increase the efficiency of the entire process: for the same applied pressure difference a greater quantity of fresh water could be obtained reducing the overall costs of water production. It is through recent advances in manufacturing, e.g. reactive ion etching, that these intricate nanoscale membranes can now be fabricated.

Miller *et al.* created a CNT membrane in 2001 by CVD of carbon within the pores of an alumina membrane [54]. This produced open CNTs with diameters around 100 nm. While these sizes are too large for selective filtration purposes, this was an important development in membrane technology. The inner walls of the CNTs in the membrane were partially amorphous, and functional groups, e.g. carboxyl groups, were present on the CNT tips and walls.

Hinds *et al.* and Majumder *et al.* created CNT membranes by using a polystyrene

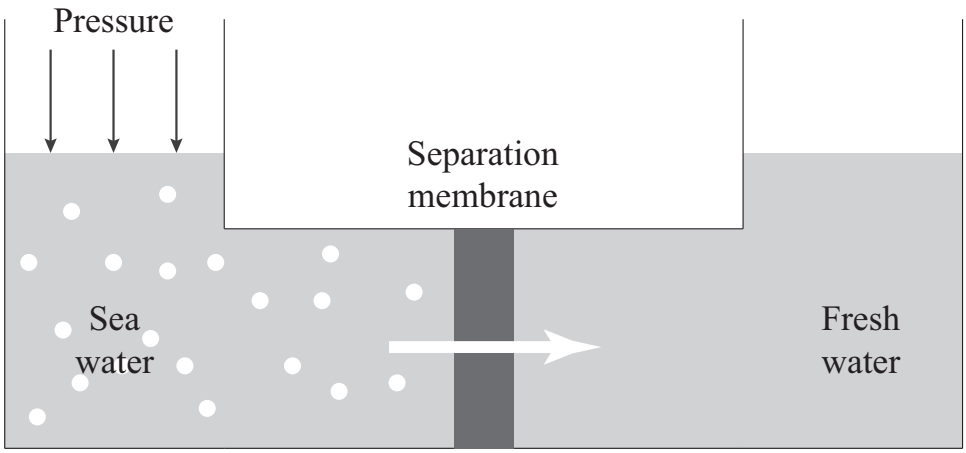

Figure 2.3: Schematic of reverse osmosis process.

solution to spin-coat aligned CNTs grown on a silica substrate by CVD [55–57]. A water plasma-oxidation process is used to open the sealed CNTs. This process can create membranes of multi-wall CNTs with diameters as small as ∼7 nm.

Holt *et al.* created a CNT membrane by catalytic chemical vapor deposition on the surface of a silicon chip [58]. This produced vertically-aligned MWNTs with an average pore diameter of 66 nm. Silicon nitride, a ceramic material, is used to fill the gaps between the CNTs by low-pressure deposition. Excess silicon nitride is removed by ion milling. The CNTs are uncapped (opened) by a reactive ion etching process using an oxygenated plasma. More recently, Holt *et al.* used this technique to produce a CNT membrane composed of double-wall nanotubes (DWNTs) with diameters less than 2 nm [2, 59]. These researchers noted the presence of carboxylic functional groups at the CNT tips.

CNT membranes will be subject to large pressure differences (5 – 7 MPa) during the reverse osmosis desalination process and their mechanical strength must be such that they are capable of withstanding these applied forces. The integrity of the membrane will be affected by the choice of packing material, i.e. ceramic or polymer. Ceramics are more brittle, and any voids present may lead to cracks and membrane failure [58]. The maximum pressure drop a CNT

Figure 2.4: Cross-section of CNT membrane created by Holt *et al.* [2].

membrane can withstand before failing is given as [58]:

$$\Delta P = 0.29 \left(\frac{t_m}{r_m}\right) \sigma_{\text{yield}} \sqrt{\frac{\sigma_{\text{yield}}}{E}}, \tag{2.4}$$

where t_m is the membrane thickness, r_m is the membrane radius, and σ_{yield} and E are the yield stress and Young‘s modulus of the membrane material, respectively. Holt calculated that his fabricated silicon nitride CNT membrane, with a thickness of 5 μm and a radius of 2 mm, could withstand a pressure drop of 0.2 MPa [58]. CNT membranes must be able to withstand much higher pressure differences than this for reverse osmosis applications, which may require a re-design of the membrane geometry.

Membrane fracture is clearly a mechanical concern but there may be associated health issues caused by CNTs in membranes becoming dislodged, leading to possible ingestion/inhalation by humans and toxic effects such as lung disease and cancer (malignant mesothelioma) [60]. Studies are ongoing to assess whether CNTs can produce toxic effects similar to those of asbestos (which has a comparable fibrous structure) [60].

Clearly the fabrication of CNT membranes is a demanding task which requires

many complex processes, e.g. filling interstitial sites, which makes the overall production rather expensive. Small CNT diameters (less than 1 nm) required for effective desalination, and used in simulations, are not currently able to be manufactured as part of a membrane [15], which has created a void between simulation and experiment. This is discussed further in Chapter 6.

2.3 Experiments on water flows through carbon nanostructures

Experimental flow rate measurement of water transport through CNTs, CNPs and CNT membranes is currently the subject of intense research. Due to the difficulties in performing experiments at these extreme scales, there is a lack of experimental results for water flow through these nanostructures, especially towards the smallest diameters penetrable by water, where efficient filtration would occur, as discussed previously. CNTs and graphene are hydrophobic in nature [53] and have potential external flow applications such as low-drag surface coatings [12], however only internal flows and their application are considered here.

Techniques such as microscopy (optical or electron) can investigate water in MWNTs and larger diameter SWNTs, as shown in Fig. 2.5; and spectroscopy can be used to study water in SWNTs with smaller diameters. Spectroscopy techniques include: neutron scattering, nuclear magnetic resonance, x-ray scattering, and Raman scattering. The radial breathing mode frequency of SWNTs changes when filled with water [61]. Using resonant Raman scattering, experiments can be performed to study water-filling for each specific SWNT structure separately. This is a significant advantage compared to other experimental techniques, and allowed the discovery of the smallest diameter CNT penetrable by water: 0.548 nm [62].

Water transport rates are typically calculated by measuring the mass of water

produced at the outlet of the CNT over a given time period, however other methods do exist and are discussed shortly. The measured mass flow rate is often compared to a theoretical, hydrodynamic prediction in terms of a "flow enhancement factor", which is defined:

$$\epsilon_f = \frac{\dot{m}_e}{\dot{m}_h}, \tag{2.5}$$

where $\dot{m}_e$ is the measured flow rate (mass or volumetric) and $\dot{m}_h$ is the equivalent hydrodynamic flow rate, which may be calculated via the no-slip or slip-modified Hagen-Poiseuille relation for flow in a cylindrical pipe.

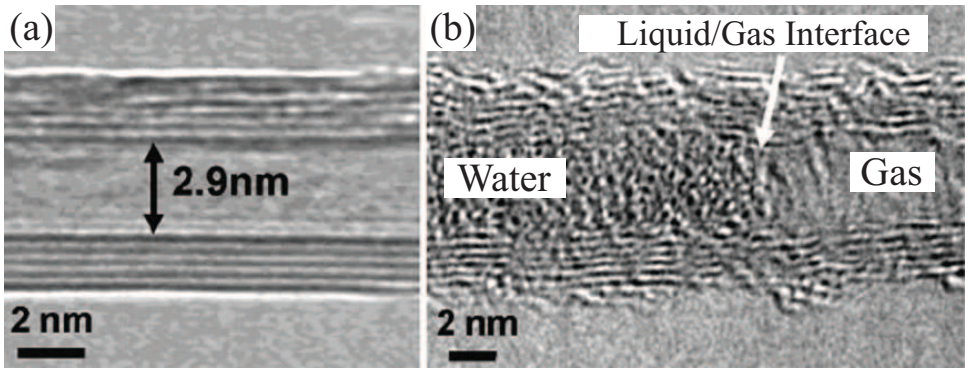

Figure 2.5: Transmission electron microscopy (TEM) images of: a) an empty 2.9 nm diameter MWNT, and b) water filling the same CNT with the liquid/gas interface highlighted. TEM passes a beam of electrons through the sample to form the above image. Taken from [3].

Sinha *et al.* [63] were the first to measure flow through single CNPs with diameters of 200-300 nm created using CVD. Sinha *et al.* modified the surface structure by graphitising it, making it more like a carbon nanotube. Using an environmental scanning electron microscope they found that the diameter of the nanopipes varied by 10 to 20 percent along their axes. The experimental set up involves placing two water droplets of different sizes at either end of the nanopipe. With the droplets being different sizes, a pressure difference across the pipe is generated, the magnitude of which can be calculated from the drops radii of curvature. The flow rate was measured by monitoring the change in size of the droplets. Sinha *et al.* found that the flow rate of water through carbon nanopipes

with a diameter >200 nm is the same as that predicted by the hydrodynamic relation (i.e. the no-slip Hagen-Poiseuille equation) giving an enhancement factor of 1.

More recently, Ray *et al.* [64] measured water flow rates through carbon nanopipe bundles with diameters ranging from 200-500 nm, with a syringe pump driving the water through the nanopipes. They also found that the fluid flow rate matched the no-slip Hagen-Poiseuille prediction (i.e. $\epsilon_f = 1$).

The flow rate of water through an array of aligned carbon nanopipes with an average diameter of 46 nm was measured by Whitby *et al.* [65]. The nanopipe array was created by the build up of carbon on an aluminium oxide template using non-catalytic CVD. Unlike previous studies, the nanopipes were not annealed, therefore the carbon surface remained fully amorphous. A syringe pump was used to drive water through the nanopipes and the flow rate was measured by collecting the emerging water and weighing it periodically. Flow enhancements were found to be 22-34 times greater than hydrodynamic predictions.

Majumder *et al.* [56] was the first to report water flow rates through CNTs. Multi-wall CNTs with inner diameters of 7 nm were aligned in a polymer film forming a membrane with a packing density of 5×10^{10} per cm^2. The pore density of the membranes was estimated using KCl diffusion through the membrane and TEM images [55, 56, 66]. Flow was generated by using a piston pump, and a pan balance was used to determine the flow rate. Majumder *et al.* reported flow enhancement factors of order 10^4 to 10^5 times greater than hydrodynamic predictions. These researchers confirmed their original findings very recently, using the same techniques, and again reported very high enhancement factors of $\epsilon_f = 10^4 - 10^5$ [57]. They also manufactured CNT membranes (7 nm diameter as before) that are tip-functionalized and core-functionalized. These showed a reduced enhancement factor of 5, for the same pore size.

Holt *et al.* successfully aligned double-walled CNTs in a silicon nitride matrix with an average nanotube diameter of 1.6 nm [2, 59]. The CNT diameter

was determined by performing size exclusion experiments and using electron microscopy. The pore density was found to be $\sim 2.5 \times 10^{11}$ per cm^2 using TEM images. A pressure difference across the membrane was created by pressurising the upstream reservoir using a controlled nitrogen gas line. Atmospheric conditions were imposed downstream of the membrane. The water flow rate was measured by observing the change in fluid volume in the upstream reservoir with respect to time. Holt *et al.* recorded flow rates that exceeded hydrodynamic predictions by over three orders of magnitude, ranging from $\epsilon_f = 560$ to 8400. A summary of these recent experimental results is shown in Table 2.2.

Author	Average Diameter (nm)	Flow Enhancement Factor, ϵ_f
Sinha *et al.* [63]	200 - 300 (CNP)	1
Ray *et al.* [64]	200 - 500 (CNP)	1
Whitby *et al.* [65]	46 (CNP)	22 - 34
Du *et al.* [67]	10 (CNT)	10^5
Majumder *et al.* [56]	7 (CNT)	10^4 - 10^5
Holt *et al.* [2]	1.6 (CNT)	560 - 8400
Qin *et al.* [68]	0.8 (CNT)	900

Table 2.2: Flow enhancement factors from experiments on pressure-driven water flow through CNPs and CNTs.

Experiments have shown that the flow of water through CNPs with diameters >100 nm has no enhancement over hydrodynamic expectations [63, 64] and that this description of a liquid is still valid at these length scales. However, experiments have also shown significant flow enhancements for CNPs and CNTs with diameters <100nm, and this enhancement becomes greater in smaller diameter nanotubes before dropping in the smallest diameter CNT membranes currently being manufactured. A rise in flow enhancement may be expected when the CNT diameters are less than 100 nm, since the effect of fluid slip becomes more significant. However at the smallest diameters penetrable by water, where only a single strand/chain of water molecules is being transported through the CNT, it is fair to ask whether the applicability of slip flow theory is still valid since

there is only one fluid layer? In this instance the entire fluid may be regarded as "slipping" along the nanotube inner surface and the use of slip-enhanced hydrodynamic equations may be invalid. The slip flow relations are based upon a fluid velocity gradient adjacent to the nanotube surface, but the determination of this velocity gradient when only one fluid layer is present is non-trivial.

Flow enhancement factors are generally calculated using predicted mass flow rates based on the no-slip flow relations. While this equation is not strictly valid in this flow problem it can be used as a comparison across all CNT diameters to provide generalised flow enhancement factors. The no-slip Hagen-Poiseuille mass flow rate is dependent upon density and viscosity terms that are typically taken as the bulk values – which may not be appropriate. However, if the use of bulk values is consistent this may be acceptable as the hydrodynamic relation is only used as a comparison; it is important that researchers compare to the same benchmark.

Small changes in diameter have been reported by experimentalists that can lead to significant deviations in flow rate, although perhaps not as much as the orders of magnitude that exist between reported values. Given that Holt's technique produces tip functionalised DWNTs in membranes, could the presence of functional groups in this work be causing a reduction in the reported flow enhancement factors? This has certainly been shown to play an important role in mass flow rate by, e.g. Majumder, and also MD simulation [57, 69, 70].

With this field being so new, it makes determining accurate trends problematic, and the relationship between CNT diameter and water flow rate is still not clarified. More experiments at smaller CNT diameters (<2 nm) are required to reveal the current counterintuitive flow behaviour and whether errors are present in some of the reported flow rates.

2.4 CNT defects

Carbon nanotube defects are very common as it is extremely difficult to synthesise ideal, pristine surface structures. The properties of CNTs, including fluid transport, will be affected by the presence of defects on their inner-walls and tips. There are many different defect types that can occur during the manufacturing process:

- functionalisation defects: carbonyl (C=O) groups [71], carboxyl (COOH) groups [72], or hydroxyl (OH) groups[73] become attached to carbon atoms on the CNT inner-wall and/or tips during synthesis;
- Stone-Wales topological defects: random carbon to carbon bonds rotate by 90° to change the hexagonal arrangement of carbon atoms into pentagons and heptagons [74–76];
- vacancy sites: these structural defects can be mono-vacancies or multi-vacancies in the walls of CNTs [77, 78];
- adatoms (doping): carbon atoms are substituted by other elements, e.g. boron or nitrogen [79], or additional chemisorbed surface impurities are located on the inner-walls [80, 81];

Functionalisation defects are mainly created during the uncapping process by ion etching [58] or plasma-oxidation [66]. The type of functionalisation can be controlled by varying the phase of the plasma treatment, e.g. water vapour plasma treatment is most likely to introduce carboxyl groups on the tips of the CNTs [66]. The tip functionalisation of CNTs in a membrane could have an effect on the ion transport through the membrane, that is if they are able to pass into the membrane at all. This electrostatic effect will have a significant role to play in the future applicability of CNT membranes to desalination.

2.5 Generating CNTs in OpenFOAM

A common method for generating CNTs in MD simulations begins by creating a unit cell of graphene, the width of which corresponds to the circumference of the CNT, which is then "rolled" into a nanotube. Unit cells have a fixed length equal to the magnitude of a translational vector, **T**. The user can only create lengths of nanotubes that are multiples of the unit cell [82]. A drawback of this method is that unit cells of nanotubes of larger diameters will consist of tens of thousands of atoms, ideally the user should have greater control over the dimensions of the nanotube.

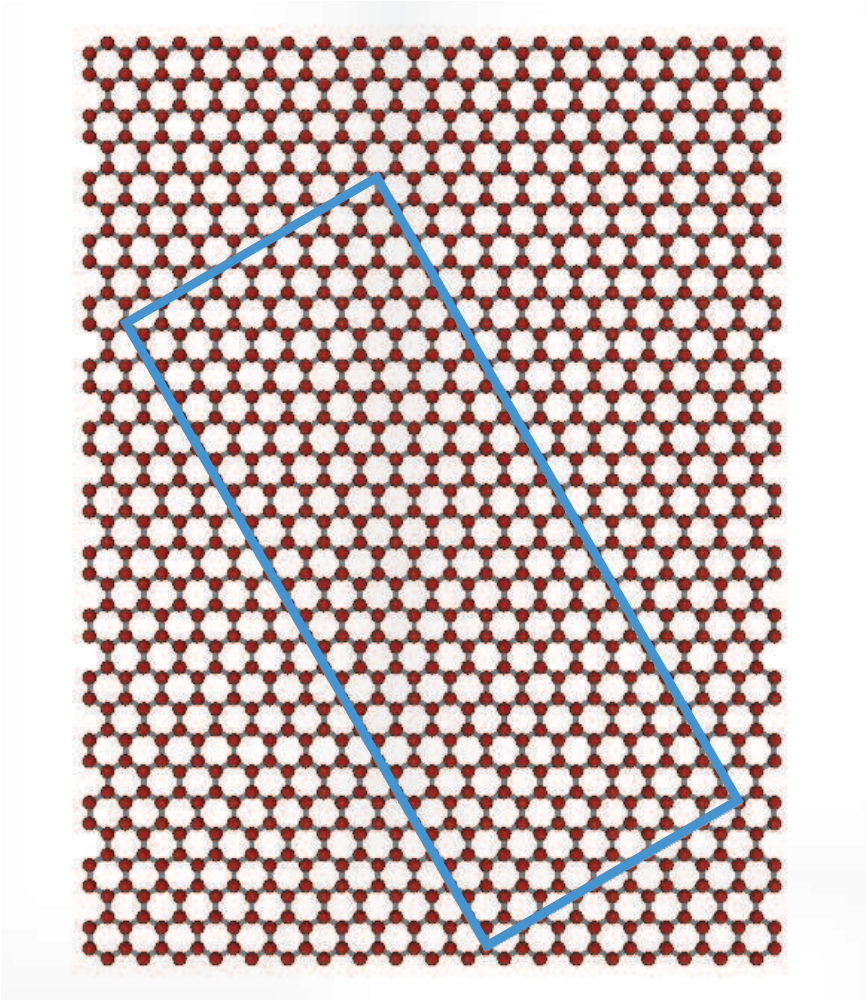

Figure 2.6: Full graphene sheet (red circles) and the required nanotube sheet (blue rectangle) generated in OpenFOAM.

A new method that gives the user complete control over the length and structure of the nanotube has been created in OpenFOAM by extending to the molecule configuration technique which already exists [83]. The input parameters for the CNT modelling technique in OpenFOAM are given in Table 2.3. This method first creates a regular graphene sheet that is large enough to contain a smaller sheet, as shown in Fig. 2.6, whose alignment is determined by the chiral vector $\mathbf{C_h}$, and is then "cut-out" and "rolled" into a nanotube.

Input	Description
n	First part of chiral vector, must be an integer
m	Second part of chiral vector, must be an integer
cntStartPoint	Position vector defining the starting point of the CNT
cntEndPoint	Position vector defining the end point of the CNT
fullyFrozenIds	This field is used when the full CNT is to be frozen to its original position
id	Molecule id e.g. C for carbon
bondLength	Carbon to carbon bond length, a_{CC}

Table 2.3: Required input data for creating CNTs in OpenFOAM.

This method can create any number of nanotubes with different lengths and chiral vectors in a single simulation, e.g. see Fig. 2.7 a). To create multiple CNTs the user must use individual entries for each CNT. Another feature of this method is that it is fully parallelised, meaning that the carbon atoms comprising the nanotube can reside on any number of different computer processors, as shown in Fig. 2.7 b). However, CNTs can currently only be modelled as rigid structures in OpenFOAM.

2.6 Summary

In this chapter we have discussed the fluid transport properties of CNTs. A review of physical experiments involving water flows through carbon nanostructures, including CNT membranes, has shown that fluid flow rates through CNTs

with diameters less than 100 nm are significantly higher than hydrodynamic expectations. CNT and CNT membrane synthesis is faced with many challenges, one of which is the control of surface defects. CNT defects manifest themselves in a variety of ways, e.g. vacancy sites (missing carbon atoms), and these defects can have a significant effect on the fluid transport properties of CNTs. We have also presented a novel technique for producing CNT atom positions for an MD simulation on any number of computer processors. Using OpenFOAM, we can generate CNTs of any chirality and, more importantly, any length from a few user inputs.

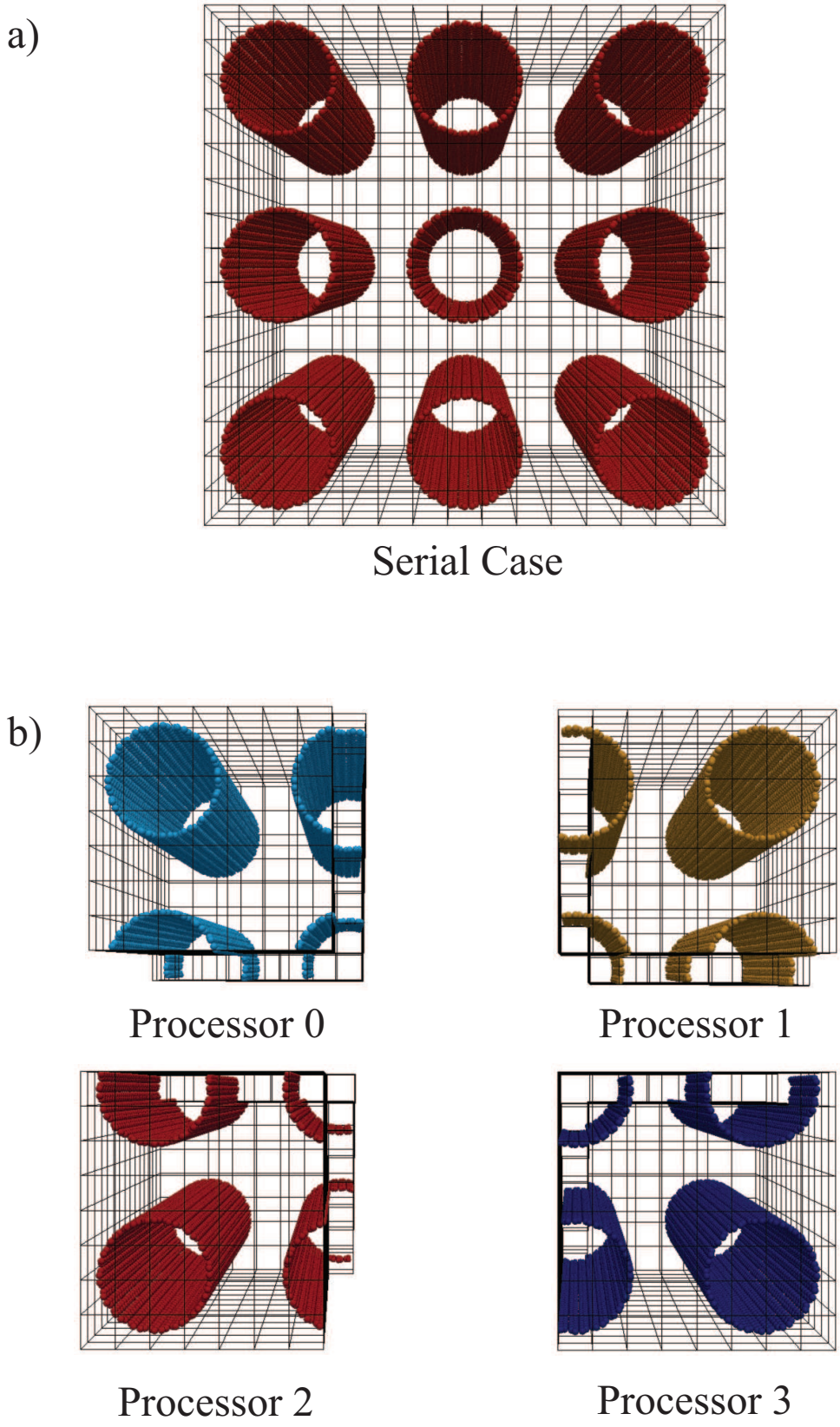

Figure 2.7: Multiple carbon nanotubes (end-on) in a) a serial simulation and b) a four processor simulation.

Chapter 3

MD Simulation of Water in CNTs: A Review

Molecular dynamics provides an accurate way of studying fluid flow at the nanoscale which is much easier than performing experiments. MD has established itself as an integral part of present and future nanofluidic research, including water transport through CNTs. MD is constantly evolving and becoming more flexible, allowing users to tackle difficult flow problems such as establishing the fundamental mechanism responsible for water flow rate enhancements through CNTs (originally observed from experiment). Even with huge advances in experimental observation techniques in recent years, insights provided by MD are proving to be invaluable e.g. internal velocity and density profiles at scales where experimental measurements are not possible. In spite of the hundreds of papers published in this area, it still remains unclear why the flow rate of water through CNTs is so high: slip flow at the liquid-solid interface, frictionless fluid transport, reduction of fluid viscosity, and alterations to the atomistic fluid structure due to geometrical confinement are some of the possible explanations which have been suggested by MD simulations.

3.1 Water models

Computer simulations of water, the most ubiquitous fluid in nature, have been the focus of over 30 years of MD research [84]. Despite the large amount of time devoted to this task, there is no model in the literature which can accurately reproduce all of the properties of water from atomistic simulations. There are over 40 water models reported in the literature, which highlights the fact that no single model is fully representative of real water. The essential characteristics of any water model are that it must be capable of reproducing the basic properties of water, such as the self diffusion coefficient, viscosity, radial distribution function, heat capacity, and hydrogen bond structure [85].

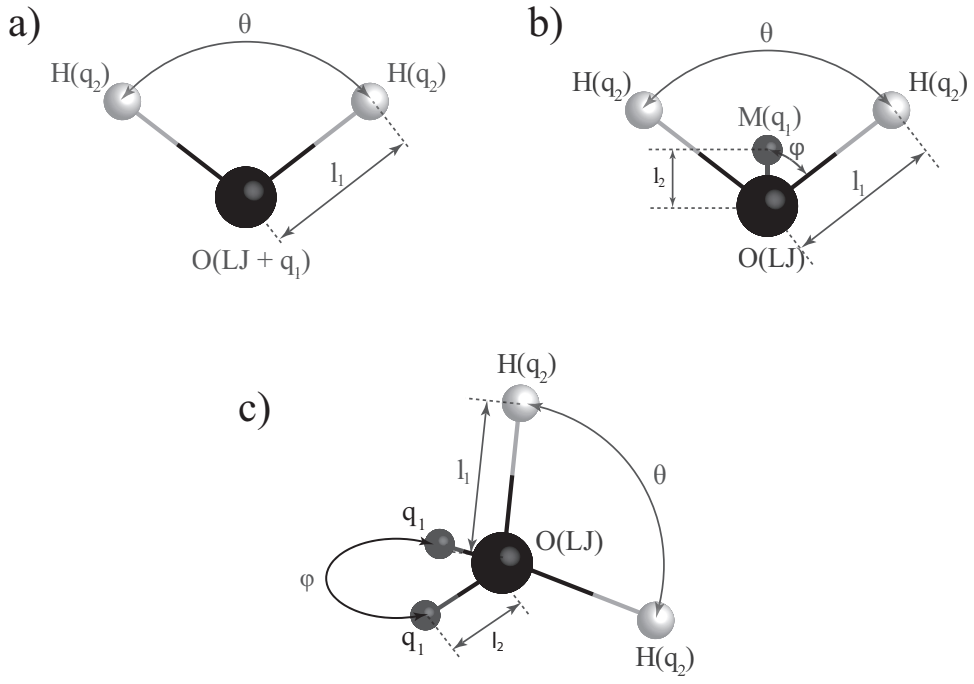

Figure 3.1: Different water models can contain different numbers of interaction sites: a) three-site model b) four-site model and c) five-site model. Interaction parameters, bond lengths and bond angles for different models are presented in Table 3.1.

Of the vast number of water models produced over the years, the most commonly used are: SPC [86], SPC/E [87], TIP3P [88], TIP4P [89] and TIP5P [90]. The parameters for these water models are shown in Table 3.1. The SPC, SPC/E and TIP3P are three-site models of the form shown in Fig. 3.1a). The TIP4P is

a four-site model, and the TIP5P is a five-site model, shown in Figs. 3.1b) and c) respectively. The main difference between these water models is the representation of the dipole moment i.e. the locations of the shared electrons of the covalent bonds between oxygen and hydrogen, shown as q_1 in Fig. 3.1. The location of these sites are used as fitting parameters for specific thermodynamic properties, meaning that each model is only accurate for specific properties. Therefore the choice of water model is dependent upon what property the user needs to represent accurately. For example, the TIP4P water model is best suited to model the phase change of liquid water to ice [91].

Model	No. of Sites	θ°	ϕ°	$q_1(e)$	$q_2(e)$	$l_1(\AA)$	$l_2(\AA)$	$\sigma(\AA)$	ϵ(kJ mol^{-1})
SPC	3	109.47	-	0.41	-0.82	1	-	3.166	0.65
SPC/E	3	109.47	-	0.4238	-0.8476	1	-	3.166	0.65
TIP3P	3	104.52	-	0.417	-0.8340	0.9572	-	3.15061	0.6364
TIP4P	4	104.52	52.26	0.52	-1.04	0.9572	0.15	3.15365	0.648
TIP5P	5	104.52	52.26	0.241	-0.241	0.9572	0.7	3.12	0.669

Table 3.1: Parameters for popular water models.

The performance of each of these models varies depending on the phase of the water under investigation, e.g. liquid-solid, and the physical property being measured, e.g. self-diffusion coefficient. Some models are more accurate than others under certain circumstances but no single model is accurate for all conditions, which makes the selection of a model more difficult.

The use of rigid water models is commonplace in modern MD simulations. This configuration means that the atoms or sites of the water molecule do not move relative to each other, meaning the bond lengths and bond angles are fixed. This enables larger simulation time steps to be used (no bond vibration frequencies to consider), allowing longer simulation times to be accessed.

While the values of charges remain fixed in the models described previously, there exist polarisable models which include charge fluctuations. The inclusion of such fluctuations (e.g. Charge-On-Spring models) is complicated but has been shown to be more accurate [92], however polarisable models are computationally more demanding than non-polarisable models.

Reference	Water model	Year
Thomas and McGaughey [5, 11, 93, 94]	TIP5P	2008 – 2010
Corry[69, 95]	TIP3P	2008 – 2010
Zambrano *et al.* [96]	SPC/E	2009
Shiomi and Maruyama [97]	SPC/E	2009
Zuo *et al.* [98]	TIP3P	2010
Suk and Aluru [99]	SPC/E	2010
Rivera and Starr [100]	TIP5P	2010
Mukherjee *et al.* [101]	TIP3P	2010
Beu *et al.* [102]	TIP4P & COS/G2†	2010
Su *et al.* [103]	TIP3P	2011
Ma *et al.* [104]	TIP3P	2011
Majumder and Corry[70]	TIP3P	2011
Nicholls *et al.* [105]	TIP4P	2011

† polarisable model.

Table 3.2: Water models used in water-CNT MD simulations. All models are rigid.

Many different water models are used in CNT water simulations, see reference [44] for a summary up to year 2008. Since this review paper was written there have been many more simulations which have also used five-site water models. Simulations of water flow through CNTs and the water models used in more recent studies are listed in Table 3.2. No study has been performed to identify which model is best suited for water contained within CNTs due to the lack of experimental data required for comparison [44]. The choice of water model in CNT simulations remains fairly arbitrary.

Van der Spoel and van Maaren [36] investigated the effect of truncating the electrostatic interaction of water in MD simulations. They found that TIP3P water formed strange layer formations due to electrostatic truncation but discovered that TIP4P is much less affected by this problem because the dipole-dipole interaction is quenched at long distances. Since truncated electrostatic interactions will only be considered in all of the MD simulations in this thesis, TIP4P is chosen as the water model best suited for this flow problem.

MD simulations are performed to ensure that the TIP4P model is performing

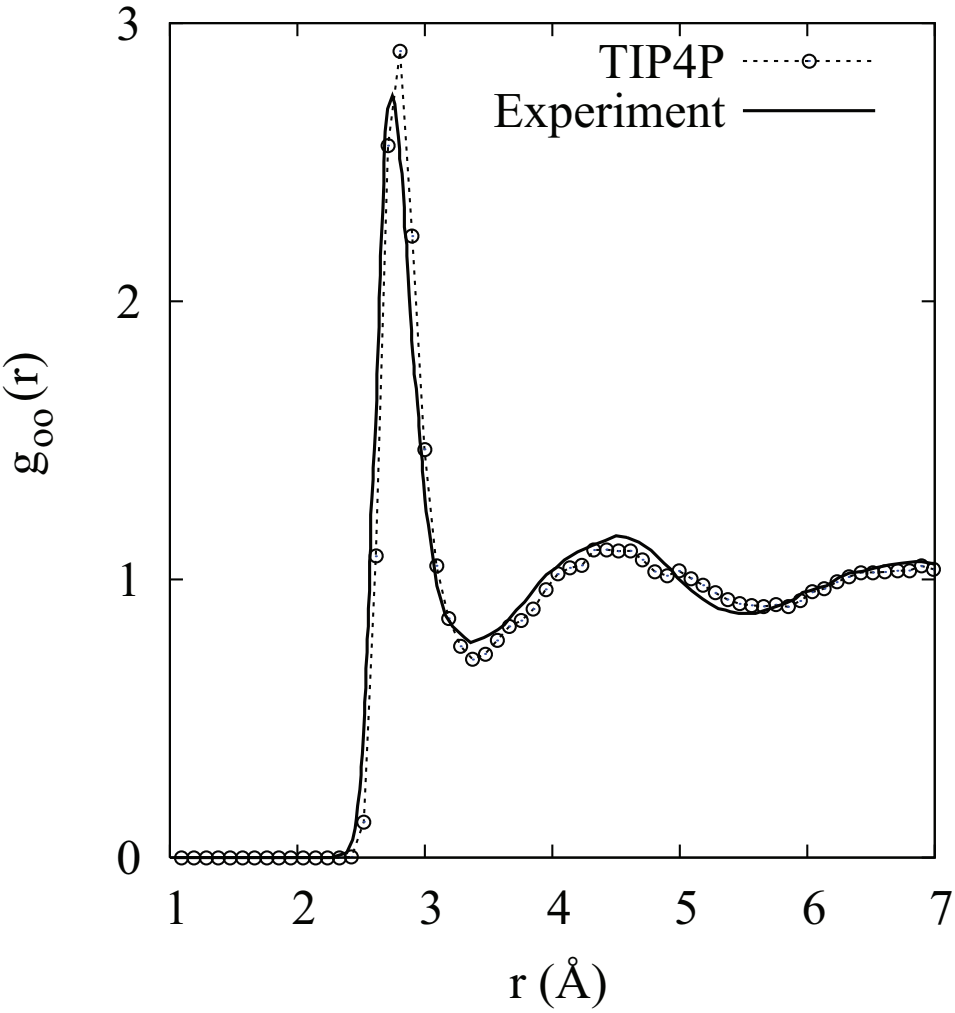

Figure 3.2: The radial distribution function of the TIP4P water model measured using *mdFoam* compared with experimental data [4]. g_{OO} refers to the RDF between oxygen atoms of different water molecules.

correctly in OpenFOAM. The radial distribution function (RDF) of oxygen sites is measured using 1000 TIP4P water molecules in a periodic cube using *mdFoam*. The RDF provides a measure of the local fluid structure: peaks at short atom separations indicate a higher likelihood of atoms being present at these distances. The RDF acts like a fingerprint for a fluid at a given density and temperature. The water density and temperature in this simulation are 997 kg/m^3 and 298 K, respectively. These properties are controlled using a Berendsen thermostat and a density controller, described in detail in Chapter 4, for an initial time period of 0.5 ns after which the controllers are turned off and the RDF is measured over a

1 ns time period (1×10^6 time-steps). The result is compared with experimental data [4] and is shown in Fig. 3.2. Excellent agreement is present with only a slight discrepancy at the first peak which is common in MD simulations [91]. This result indicates that the implementation of the TIP4P water model, and its associated interaction parameters, has been successful and is performing correctly. The truncation of the electrostatic potential has not resulted in layering at long distances.

3.2 Carbon-water interactions

The representation of the interaction between water molecules and carbon atoms will have a major effect on the behaviour of water in CNT simulations. Similar to the choice of water model, there exists a difficult decision in choosing the correct carbon-water interactions. This interaction is generally represented by a carbon-oxygen LJ potential, however the choice of σ_{CO} and ϵ_{CO} remain open to debate. Werder *et al.* [106] used MD to simulate a water droplet on a graphene sheet and "tuned" the LJ parameters to match the corresponding macroscopic wetting contact angle (WCA). Their findings suggest the use of the following: $\sigma_{CO} = 3.19\mathring{A}$ and $\epsilon_{CO} = 0.392$ kJ mol^{-1}. These LJ parameters are specifically for the water model used in those experiments, the SPC/E model. It may be the case that each water model should require a separate "tuning" procedure to match the resultant WCA, so producing specific LJ interaction parameters for each type of water model. Wang *et al.* [107] suggest that these values found by Werder *et al.* may only be used in large diameter CNTs, however many authors have continued to use these parameter values in small diameter CNTs. Longhurst and Quirke [108] suggest that the radial breathing mode of a CNT submerged in water could provide a way of determining the interaction parameters between CNTs and fluids. The debate over the correct way to model the interaction between water and carbon will remain open until more experimental data is

available, or perhaps until more quantum chemistry studies are performed.

CNTs are commonly modelled as rigid structures to speed up the MD runs: this has been reported to be a fair approximation in a previous study [109]. Alexiadis and Kassinos [110] also found that water transport was unaffected by the use of a flexible CNT model over a rigid one.

3.3 Water structure in CNTs

While experiments have successfully determined that water becomes ordered in smaller diameter CNTs, they have not yet provided information on water structure under such confinement. Raman spectroscopy experiments [62] have shown that water can penetrate into CNTs with diameters as small as 0.548 nm (corresponding to a chirality of (5,3)) and it was deduced that water must form a single-file chain of molecules at this diameter, as it is only possible for one chain of water molecules to fit inside the CNT. The actual structure of water inside CNTs can currently only be investigated using MD.

Many papers have reported that single-file water chains exist in CNTs with diameters less than 0.9 nm [5, 11, 95, 98, 101, 111–114]. Hummer *et al.* [115] found that in these extremely confined conditions, water molecules form only two hydrogen bonds, as opposed to four in bulk conditions, and this is believed to be related to the unusual water properties under these conditions, e.g. fast proton transport [113].

Above this range of diameters, the reported radial and axial structure of water varies significantly: between 0.86 and 1.39 nm, different ordered structures are present and above 1.39 nm bulk-like water structures are present. In the 0.86 to 1.39 nm diameter range there exists a debate about the actual structure of water, with some reports from MD simulations contradicting others. Previous studies have shown that there is no correlation between the CNT chirality and the internal fluid structure at diameters below 1.39 nm [5, 94]. So CNTs with different

chiralities but the same diameter should produce similar results. Therefore the structure of water is presented in relation to CNT diameter from here onwards in this thesis.

Noon *et al.* [116] studied TIP3P water inside CNTs with diameters ranging from 0.96-1.25 nm and found that water formed "ice sheets" under ambient conditions (300 K and 1 atm). They also stated that water did not enter a (5,5) CNT, with a diameter of 0.66 nm, which does not agree with experimental findings [62]. Mashl *et al.* [117] presented MD results which showed that SPC/E water under ambient conditions forms a stacked column of cyclic hexamers in (9,9) CNTs, with a diameter of 1.25 nm, but not in (7,7), (8,8) or (10,10) CNTs.

Liu *et al.* [118] found that SPC water in a 1.39 nm diameter CNT formed helical chains and suggest that in general the structure of water in CNTs is solidlike. However, Wang *et al.* [107] found that TIP3P water in CNTs with diameters ranging from 0.96-1.39 nm displayed no obvious structuring, yet it did not resemble bulk-like structures either, and they suggested that the ordering of water may be sensitive to the choice of interaction potential parameters.

Thomas and McGaughey [11] reported numerous polygonal TIP5P water structures in CNT diameters of up to 1.25 nm, above which bulk-like structures were present. Corry [95] observed double and quadruple water chains in 0.96 and 1.10 nm diameter CNTs, respectively, using TIP3P water.

Wang *et al.* [107] also suggested that LJ interaction parameters between water and carbon may affect water structuring. There are no "correct" parameters which must be used in water-carbon simulations as discussed in the previous section. This may explain why, for the same water model under the same conditions, Wang *et al.* obtained different results from Corry [95]. Alexiadis and Kassinos [119] note that low values for the interaction parameters result in polygonal structures while higher values lead to disordered structures. Gay *et al.* [120] suggest that the treatment of long range forces could also affect water structuring.

Alexiadis and Kassinos [110] demonstrated that the TIP3P water model pro-

duced a polygonal water structure in a 1.26 nm diameter CNT whereas another three-site water model, namely the SPC/E model, used under the same conditions did not demonstrate this molecular arrangement. Thomas and McGaughey [11] found that for a similar diameter (1.25 nm), TIP5P water formed a hexagonal layered structure, further emphasising the effect of water model choice on the resultant fluid structure. It has also been suggested that using thermostats can affect water structuring [121].

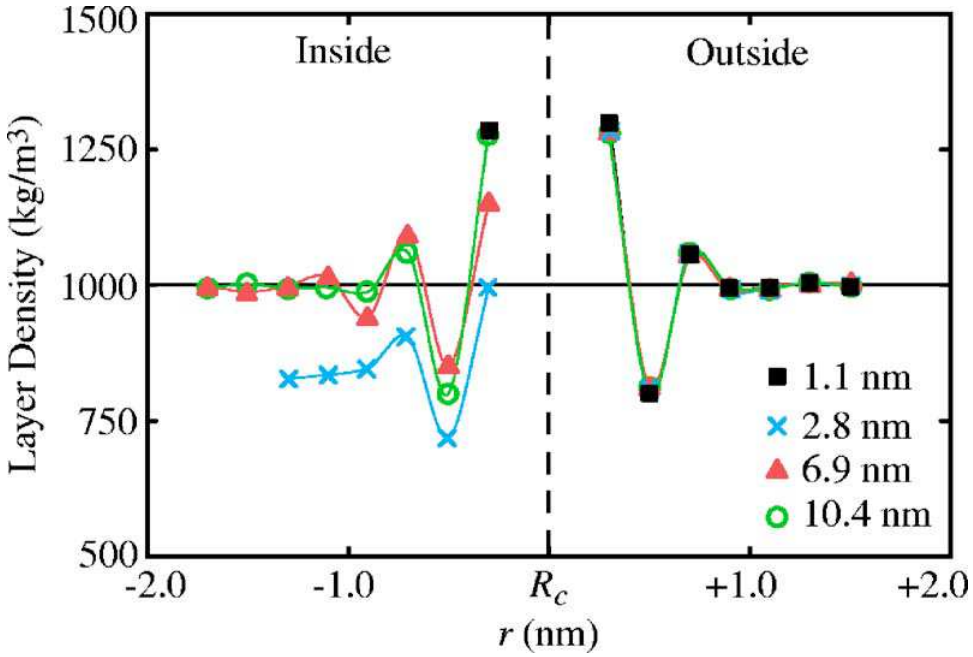

Figure 3.3: Water layering on the inside and outside of CNTs with diameters ranging from 1.1 to 10.4 nm, taken from [5].

The transition from ordered to disordered water structuring has been reported to occur at diameters greater than 1.39 nm. Even with bulk-like water structures inside (and even outside) CNTs, there always exists the presence of fluid layering adjacent to the CNT surface [5, 122]. This effect causes peaks and troughs in fluid density close to the surface before returning to bulk conditions beyond a certain distance from the solid surface. Figure 3.3 demonstrates that, regardless of a CNT's diameter, the external density distribution will remain the same. However, inside smaller diameter CNTs bulk water conditions will not be recovered. The phenomenon of fluid layering adjacent to a surface is commonplace in nanofluidics

and is caused by the interaction of the fluid with the surface, making the choice of MD interaction parameters pivotal in the resulting fluid behaviour.

3.4 Fluid flow rate

Molecular dynamics simulations have shown that water is transported through carbon nanotubes at unexpectedly high flow rates. Measured flow rates are often compared with the no-slip Hagen-Pousielle relation, as discussed in Chapter 2, to obtain a measure of the flow enhancement over hydrodynamic predictions. While MD simulations are in agreement that flow enhancement does exist, there exists a wide spread in the reported levels of enhancement.

Direct comparisons of mass flow rates from MD simulations and experiments are not possible due to computational restrictions associated with MD. Large pressure differences, typically $\mathcal{O}(100)$ MPa, and short CNT lengths are generally used in MD simulations of this type of flow problem. These magnitudes of pressure differences lead to higher fluid flow rates which can be extracted more readily from simulation above the thermal fluctuations of the molecules and the statistical noise this generates. The fluid flow rates recorded in experiments cannot currently be reproduced using MD simulations for these reasons. CNT membranes as thin as $2 - 5$ μm can be manufactured [55, 58] but MD simulations are typically performed using CNTs which are only a few nanometers in length. CNT length and its effect on fluid flow rate is discussed in Section 6.1. One possible way of making comparisons between MD and experiments is by using the flow enhancement factor, ϵ. However, there exist many MD studies in this field that do not explicitly state the pressure difference across the CNT, meaning that the flow enhancement factor cannot be calculated [94].

Joseph and Aluru [109] modelled water transport in a periodic, 2.2 nm diameter CNT and generated an equivalent pressure difference by applying an external body force to all water molecules inside the CNT. They found that the mass flow

rate exceeded hydrodynamic predictions by a factor of 2052 and suggested that water orientation and hydrogen bonding are significant in the transport mechanism of water through CNTs.

Thomas and McGaughey performed two MD studies of pressure driven water flow through CNTs, looking at different ranges of CNT diameters: 1.66 – 6.93 nm [94] and 0.83 – 1.66 nm [11]. They model the flow problem by using two water reservoirs located at either end of the CNT and apply a pressure difference through the use of a reflective particle membrane. In the first range of CNT diameters (1.66 – 6.93 nm), flow enhancement factors decrease monotonically with increasing CNT diameter from 500 (1.66 nm) to 20 (6.93 nm). They compare their results with those of Joseph and Aluru [109] (rescaled to the same diameter, 2.2 nm) and found that their flow enhancement was almost 3 times less than that reported by Joseph and Aluru. Thomas and McGaughey suggest that differences in carbon-water interaction parameters and the water model may account for this, but do not suggest that differences in modelling techniques may be significant. However, the application of an external body force to generate a pressure gradient may introduce artefacts into the MD simulation since the applied force is based upon the assumption of a bulk density inside the CNT, which may not be the case. External body forces, which are typically very high compared to the intermolecular forces, may also affect the dynamics of the water molecules and hence overall water transport through a CNT. Boundary conditions in MD simulations are discussed in detail in Chapter 4.

The second study by Thomas and McGaughey [11] (0.83 – 1.66 nm diameters), demonstrated that the mass flow rate of water through a CNT is dependent upon the CNT diameter, but not as one may expect: mass flow rate increases with decreasing CNT diameter. Thomas and McGaughey found that the flow enhancement factor increased for decreasing CNT diameters until 1.25 nm, where a sharp drop in enhancement was reported. At this diameter, water contained within the CNT no longer exhibits a bulk-like structure and Thomas and Mc-

Gaughey consider this as a transition to sub-continuum transport [11]. The flow enhancement factors then increase dramatically with decreasing CNT diameter down to 0.83 nm with a peak enhancement factor of ∼6000.

This was a significant finding by Thomas and McGaughey: the flow of water inside CNTs of diameters below 1.39 nm can be regarded as non-continuum. This means the problem cannot be accurately described using conventional continuum fluid mechanics with its associated linear constitutive relations and no-slip boundary conditions. This truly atomistic problem therefore requires a molecular dynamics simulation method.

Corry [95] was the first to utilise MD to investigate the potential of CNT membranes for seawater desalination. He modelled 12 CNTs closely packed together to form a membrane. A pressure difference was created across the membrane by applying an external force only to water molecules in a region of the upstream reservoir, this technique exploits the periodic nature of MD simulations and was first introduced by Zhu *et al.* [123]. CNT diameters ranging from 0.66 nm to 1.1 nm were investigated. The flow enhancement factors were calculated to be 2.6 for the largest diameter and 105 for the smallest diameter. The magnitude of enhancement reported by Corry is much lower than that reported by Joseph and Aluru, and Thomas and McGaughey. One of the main reasons for this reduction in enhancement is due to the transport of ions in addition to water. The competitive entry of ions and water into the CNT may have reduced the overall flow rate. Collective effects may be significant in the flow rates reported by Corry due to the representation of a CNT membrane as closely packed nanotubes, whereas other authors only model a single CNT. It has been shown that interaction of water molecules in adjacent nanotubes of the same membrane can be significant [124, 125].

Flow enhancement factors calculated from MD simulations are subject to an assumption of the effective CNT diameter needed in the no-slip Hagen-Poiseuille equation, i.e. the diameter that water can physically pass through, for which there

is no consistency in the literature. Many authors use the cross-CNT carbon to carbon diameter which results in lower flow enhancement factors since the hydrodynamic prediction will be greater. Others use the carbon to carbon diameter minus twice σ_{CO}, as this takes into account the physical size of the interacting molecules which causes a reduction in the effective diameter and an increase in the flow enhancement factor. Although these differences in diameter are small, the predicted mass flow rate is dependent upon the fourth power of the diameter, meaning that small differences can lead to significant alterations in the reported enhancement factors.

Water transport rates will also be affected by fluid structuring, i.e. how many water molecules physically fit into the CNT and whether molecular ordering is present. The CNT seems to optimise the water structure to maximise fluid transport at smaller CNT diameters: when single-file water transport is present, correlated molecular motion has been shown to occur [114], i.e. the motion of a water molecule in single-file chain is directly linked to the movement of water molecules upstream and downstream of itself. The development of this correlated motion may account for this increase in flow rates and enhancements reported at these CNT diameters.

3.5 Hydrogen bonding and orientation

Defining when a hydrogen bond is present is based upon oxygen atom separation, distance between hydrogen and oxygen atoms of water molecules that are hydrogen bond candidates, and the angle θ between the potential hydrogen bond and the oxygen-oxygen interaction vector of the two water molecules [126–128], see Fig. 3.4 and Section 4.1.7. Each water molecule can form hydrogen bonds with up to four other water molecules. The number of hydrogen bonds each water molecule forms is dependent upon the fluid temperature and choice of water model [44, 129]. Simple rigid, point-charge water models do not include many-

body effects or polarisation which can cause significant variations in the hydrogen bond strength but still provide good approximations [130, 131].

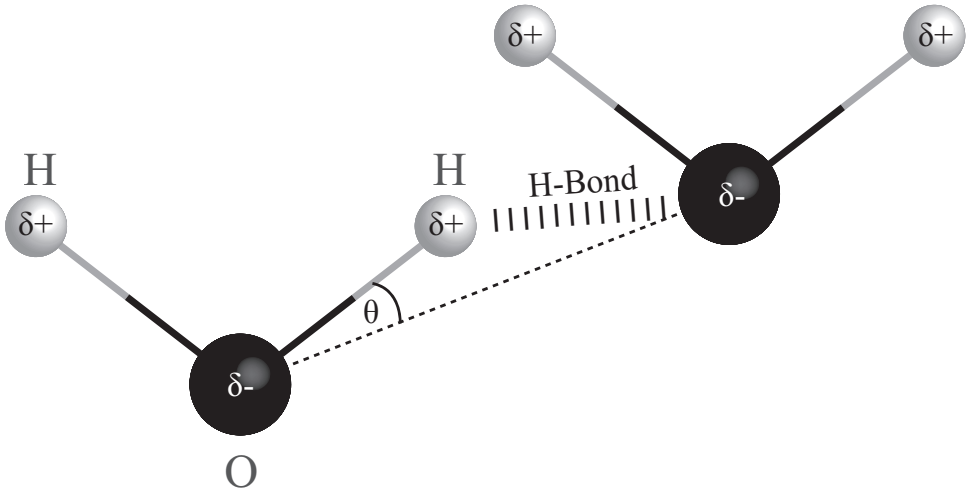

Figure 3.4: Schematic of a hydrogen bond in MD.

Similarly to water structuring, hydrogen bonding is affected by confinement, in this case the CNT diameter. The average number of hydrogen bonds per water molecule decreases from ∼4 in large diameter CNTs, where bulk-like structures are present, to less than two for the smallest diameters penetrable by water [129]. This reduction is caused by the formation of fluid layers and ordered water structures, as previously discussed. Single file water structures are commonly referred to as a "hydrogen-bonded chain" [114, 118, 132], in which water molecules form hydrogen bonds with neighbouring molecules only. Hanasaki and Nakatani [133] report hydrogen bonding profiles inside CNTs and show that if the CNT diameter is large enough hydrogen bonding similar to bulk conditions will occur on the CNT axis, but in CNTs with diameters less than 1 nm the average number of hydrogen bonds per water molecule remains below the bulk value.

Joseph and Aluru [109] demonstrated that disrupting the smooth, hydrophobic surface of a 2.2 nm diameter CNT causes a reduction in measured flow enhancements. They attribute this to a change in the hydrogen bond network: the average number of hydrogen bonds per water molecule increases, generating a stronger bond network than before. This meant that there were fewer "free" OH

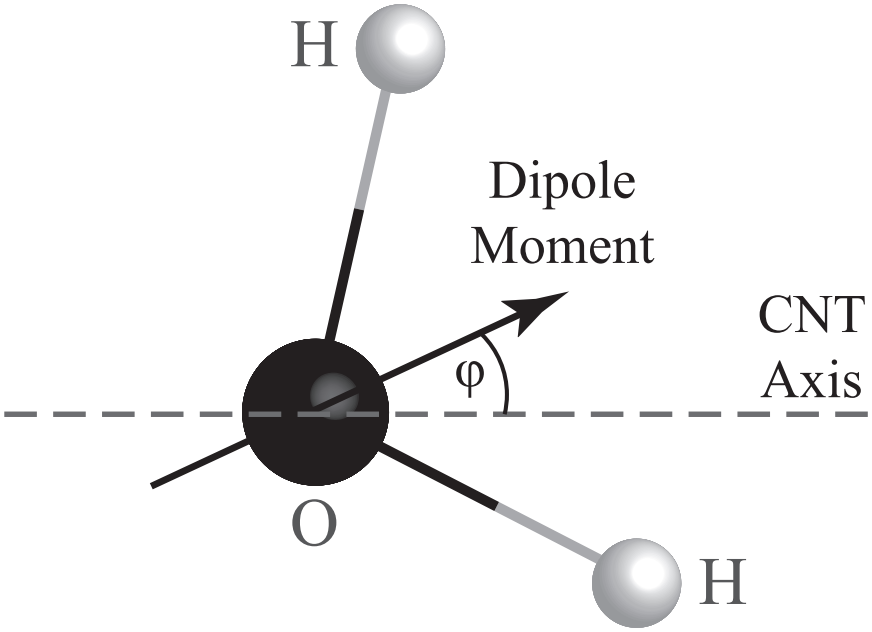

Figure 3.5: Definition of orientation of the water dipole moment.

bonds directed towards the CNT surface the authors believe that this may be related to the rapid transport of water through CNTs.

Water molecule orientation is often described through the angle between the water dipole moment and the CNT axis as shown in Fig. 3.5. The topic of dipole "flipping", where the water dipole moment changes direction while travelling along the CNT, is controversial. There are mixed reports on whether this flipping occurs and the frequency at which it happens, if at all. Some authors have shown water dipole flipping to occur very frequently [134], whereas others did not find any suggestion of its existence [107]. It could be that in the latter case the water flipping frequency was greater than the simulation time, and therefore this phenomenon was not captured. It is unclear whether water dipole flipping plays any role in water flow rate enhancements through CNTs. The measurement of hydrogen bonding and dipole moment orientation using OpenFOAM is discussed in detail in Chapter 4.

3.6 Ion rejection capabilities

The ion rejection capabilities of CNTs are important in future nanoscale technological applications, including seawater desalination. For seawater to be potable, at least 95% of the salt ions must be removed. Corry [95, 135] has shown in recent MD simulations that CNT with diameters less than 1 nm are capable of achieving this rejection rate. His work suggests that the (7,7) CNT, which has a diameter of 0.96 nm, may possess the optimum attributes for desalination, removing 95% of salt while transporting water at a suitably high flow rate. CNTs with smaller diameters than this have a lower flow rate, while larger diameter CNTs do not remove enough salt from the water for human consumption. Suk *et al.* [136] attribute the ion rejection capabilities of CNTs to a combination of steric hinderance and large energy barriers which completely prevent ions from entering the smallest diameter CNTs. Beu [102] investigated water/ion transport through CNTs with diameters ranging from 1.1-1.66 nm, using a homogeneous electric field to drive the flow. Beu confirmed that CNTs with diameters less than 1 nm do not accommodate ion transport due to significant energy barriers facing the ions.

CNT membrane ion rejection performance may be enhanced by functionalisation of the CNT tip and inner core. Corry [69] demonstrated, using MD, that by adding a variety of charged and polar groups to the tip of a 1.1 nm CNT that the nanotube became more effective at rejecting ions. However, he also found that functionalisation of the CNT reduced the mass flow rate of water and attributed this to an enhanced electrostatic interaction between the water and the functionalised CNT. Functionalisation of a CNT is likely to occur during the manufacturing process but the level of control over which functional groups are attached, as chosen by Corry, may be difficult. MD simulations of ion solutions must incorporate a comprehensive treatment of electrostatic interactions; simple truncation techniques are not adequate due to inhomogeneous charge distributions.

3.7 Summary

In this chapter we have provided a review of MD simulations of water transport through CNTs. There are a large number of different water models used throughout the literature for this flow problem and the ultimate choice remains arbitrary. The choice of water-carbon LJ parameters determines whether the interaction is hydrophobic or hydrophillic and MD studies have provided guidance when choosing these values. Water structure inside CNTs varies with diameter, with more ordered structures forming in the smallest diameter nanotubes and bulk-like structures in CNT with diameters greater than 1.39 nm. Different water models have been shown to produce different fluid structures in CNTs with the same diameter.

A number of MD simulations have demonstrated that the transport of water through CNTs is much higher than hydrodynamic predictions. However, there exists an extensive range of reported flow enhancements for similar diameter CNTs. Differences in interactions parameters, water models and boundary conditions may account for these variations.

The structure of the hydrogen bond network inside CNTs is believed to be related to the high flow rate of water through the nanotubes. There exists a debate about whether the water molecules flip orientation as they travel along a nanotube. MD simulations have shown that CNTs with a diameter less than 1 nm are able to reject 95% of ions but the salt rejection capabilities of larger diameter CNTs can be enhanced by functionalising their tips.

Chapter 4

Measurements and Boundary Conditions in MD

In this chapter, the techniques used throughout this thesis for measuring fluid properties and applying boundary conditions in MD simulations are presented. In Section 4.1 we begin by outlining methods for measuring hydrodynamic properties of polyatomic fluids. The implementation of such models within the existing measurement framework of OpenFOAM was an important outcome of this research. Section 4.2 discusses the role of boundary conditions in MD simulations with a focus on modelling pressure driven flow through nanotubes. Novel pressure boundary conditions are presented in Section 4.2.3 which allow the upstream and downstream pressures to be set explicitly by the user.

4.1 Measurements

The role of measurement techniques in MD simulations is to transform molecular data (e.g. positions and velocities) into more apprehensible macroscopic properties. While measurements can be taken at instantaneous time steps, they will be subject to substantial fluctuations which makes deriving accurate, reliable measurements difficult. Statistical fluctuations associated with measurements are

discussed shortly.

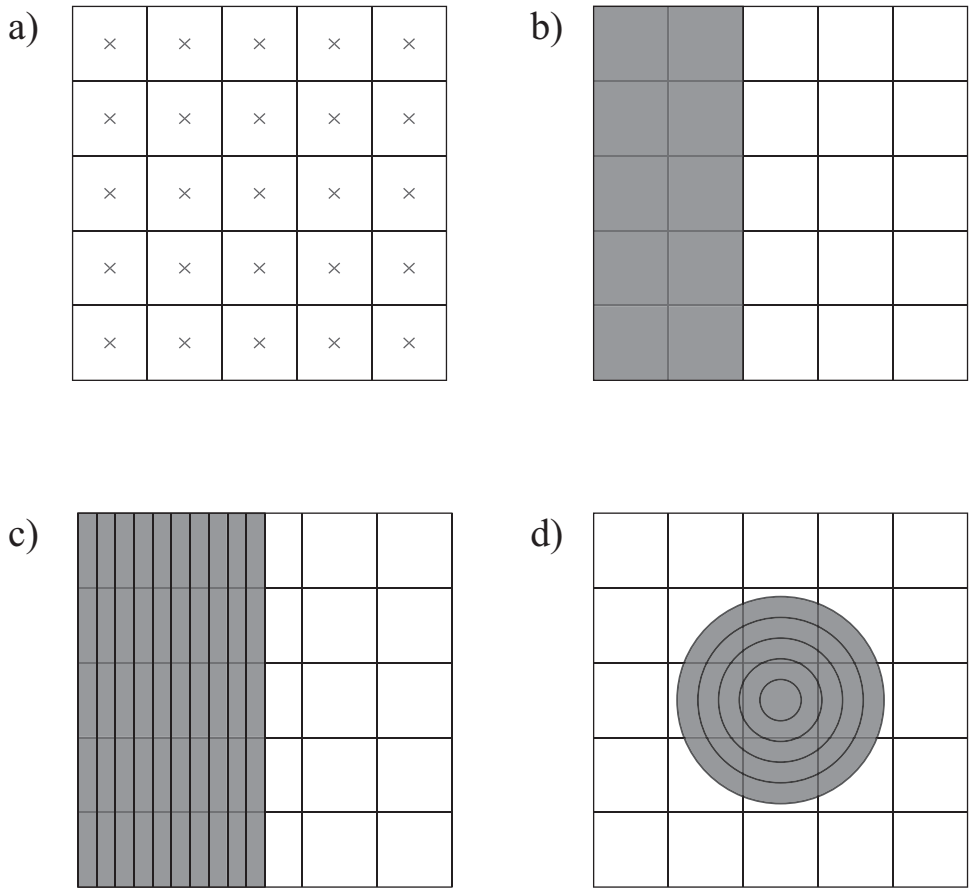

Figure 4.1: A variety of measurement techniques can be utilised in OpenFOAM, using different sampling volumes which may be dependent upon the computational mesh: a) mesh-cells and b) zone of cells or independent of the mesh: c) longitudinal bins and d) radial bins. Dark shaded areas indicate local measurement regions within the domain.

Measurements in MD simulations are commonly performed using volumes which are a subset of the simulation domain: molecules which reside within these volumes are included in the measurement procedure. For a computational domain discretised by a mesh, measurement volumes can be the individual mesh-cells (e.g. for measuring property fields, similar to finite volume techniques) or, by selecting a number of cells, zones (e.g. to measure properties within a large region of the domain, or the entire domain itself). Additional measurement volumes called bins can be used, which are independent of the mesh (e.g. to measure the spatial variation of properties in one dimension). All of these techniques are illustrated

in Fig. 4.1. By using more bins in a simulation, i.e. smaller volumes, greater spatial resolution of a measured property can be obtained. However, smaller measurement volumes lead to greater statistical fluctuations as they will contain fewer molecules on average than larger sampling regions. The number of bins to use can be estimated by using equations derived by Hadjiconstantinou *et al.* [137], and are discussed shortly.

Measurements are taken over a sampling period Δt_{av}, which spans a number of instantaneous samples, S, such that $\Delta t_{av} = \Delta t_{MD} S$, where Δt_{MD} is the MD time step. Samples can be taken every time step making them time correlated, or taken at times separated by a number of time-steps making the samples statistically independent. If time correlated measurements are used then a greater number of samples are required to reduce the associated statistical error [38].

Depending on the property being measured, the sampling time required to obtain meaningful averages can vary significantly. Hadjiconstantinou *et al.* [137] provide estimates for the number of samples required to obtain measurements with a particular statistical error E for density, velocity and pressure, presented in the following format by Werder *et al.* [38]:

$$M_\rho = \frac{\kappa_{\mathrm{T}} k_{\mathrm{B}} T_0}{V E_\rho^2}, \tag{4.1}$$

$$M_u = \frac{k_{\mathrm{B}} T_0}{u_0^2} \frac{1}{\rho_0 V E_{\mathrm{u}}^2}, \tag{4.2}$$

$$M_{\mathrm{P}} = \frac{\gamma k_{\mathrm{B}} T_0}{P_0^2 \kappa_{\mathrm{T}}} \frac{1}{V E_{\mathrm{P}}^2}, \tag{4.3}$$

where V is sampling region volume, T_0, u_0, ρ_0, and P_0 are the average temperature, velocity, density, and pressure, respectively, k_B is the Boltzmann constant, γ is the ratio of specific heats, and κ_T is the fluid isothermal compressibility. If time correlated samples are used then the required number of samples for property q

becomes:

$$M_q^c = 2\tau_q M_q, \tag{4.4}$$

where τ_q is the autocorrelation time, which is the length of time required before a property becomes uncorrelated.

Fluid density is least affected by statistical fluctuations since it is only influenced by changes in the occupancy of molecules in the measurement region, which will not be highly time-variant due to the small time step size used in MD. For example, using Eq. 4.1, to be within 5% error of density measurement of water at atmospheric conditions, in a 1 nm^3 sampling volume, will require 10^2 uncorrelated samples. Pressure measurements are subject to large fluctuations, so longer sampling periods are required to produce accurate measurements. Pressure measurement is dependent upon time-variant properties, including the intermolecular force, which can vary considerably from one time step to another in dense liquids. Using Eq. 4.3, to be within 5% error for water under the same conditions requires 10^8 uncorrelated samples.

The property measurement time-scheme in OpenFOAM, created by Borg [19], provides the user with the flexibility to sample different fluid properties over independent sampling periods within the same simulation run.

The choice of measurement technique is dependent upon the problem under investigation. More information regarding these techniques is available in [19]. One of the outcomes of this present research was the inclusion of property measurements for polyatomic fluids. In the following sections we describe how hydrodynamic properties relevant to this research are measured. The hydrodynamic properties described in the following sections are averaged using the same equations, regardless of whether they are performed in zones or bins as these are both local volumes of the simulation domain and are for one species of fluid.

4.1.1 Density

The time-averaged number density in a sampling region R, of volume V_{R}, is given by:

$$\langle \rho_{\mathrm{R}} \rangle = \frac{1}{SV_{\mathrm{R}}} \sum_{k=1}^{S} N_{\mathrm{R}}(t_k), \tag{4.5}$$

where N_{R} is the number of molecules in sampling region, S is the number of sampling steps, and t_k is an instantaneous time step.

4.1.2 Translational and Angular Velocity

The translational velocity is computed using the cumulative average measurement technique described by Garcia *et al.* [138]:

$$\langle \mathbf{u}_{\mathrm{R}} \rangle = \frac{\sum_{k=1}^{S} \sum_{i=1}^{N_{\mathrm{R}}(t_k)} m_i \mathbf{v}_i(t_k)}{\sum_{k=1}^{S} \sum_{i=1}^{N_{\mathrm{R}}(t_k)} m_i}, \tag{4.6}$$

where $\mathbf{v}_i(t_k)$ and m_i are the instantaneous translation velocity and the mass of molecule i, respectively. The angular velocity is:

$$\langle \boldsymbol{\omega}_{\mathrm{R}} \rangle = \frac{\sum_{k=1}^{S} \sum_{i=1}^{N_{\mathrm{R}}(t_k)} \mathbf{I}_i \boldsymbol{\omega}_i(t_k)}{\sum_{k=1}^{S} \sum_{i=1}^{N_{\mathrm{R}}(t_k)} \mathbf{I}_i}, \tag{4.7}$$

where $\mathbf{I}_i$ is the moment of inertia and $\boldsymbol{\omega}_i(t_k)$ is the instantaneous angular velocity.

4.1.3 Temperature

The total temperature of a rigid, polyatomic fluid is calculated using a combination of its translational and rotational temperatures [139]. There is no contribution from molecular vibration since the intramolecular bonds are fixed in our

simulations. The translational temperature is:

$$\left\langle T_{\mathrm{R}}^{trans} \right\rangle = \frac{2}{d_t k_b} \frac{\sum_{k=1}^{S} \sum_{i=1}^{N_{\mathrm{R}}(t_k)} \frac{1}{2} \mathbf{m}_i (\mathbf{v}_i(t_k) - \mathbf{u}_{\mathrm{R}})^2}{\sum_{k=1}^{S} N_{\mathrm{R}}(t_k)}, \tag{4.8}$$

where d_t is the number of translational degrees of freedom, k_b is the Boltzmann constant, $\mathbf{u}_{\mathrm{R}}$ is the average velocity of the fluid in the sampling region, and $\mathbf{v}_i(t_k) - \mathbf{u}_{\mathrm{R}}$ is the peculiar velocity of molecule i. The velocity $\mathbf{u}_{\mathrm{R}}$ is measured over a number of time steps, specified by the user, prior to the temperature measurement procedure, meaning that a slight time lag will be present. The rotational temperature is:

$$\left\langle T_{\mathrm{R}}^{rot} \right\rangle = \frac{2}{d_r k_b} \frac{\sum_{k=1}^{S} \sum_{i=1}^{N_{\mathrm{R}}(t_k)} \frac{1}{2} \mathbf{I}_i (\boldsymbol{\omega}_i(t_k) - \boldsymbol{\omega}_{\mathrm{R}})^2}{\sum_{k=1}^{S} N_{\mathrm{R}}(t_k)}, \tag{4.9}$$

where d_r is the number of rotational degrees of freedom, which is 0 for monatomic molecules (e.g. argon), 2 for linear polyatomic molecules (e.g. oxygen) and 3 for non-linear polyatomic molecules (e.g. water). The number of translational degrees of freedom is always 3, regardless of the type of molecule.

Finally, the average temperature of the fluid is:

$$\left\langle T_{\mathrm{R}}^{ave} \right\rangle = \frac{2}{(d_t + d_r) k_b} \left(\frac{\sum_{k=1}^{S} \sum_{i=1}^{N_{\mathrm{R}}(t_k)} \frac{1}{2} \mathbf{m}_i (\mathbf{v}_i(t_k) - \mathbf{u}_{\mathrm{R}})^2}{\sum_{k=1}^{S} N_{\mathrm{R}}(t_k)} + \frac{\sum_{k=1}^{S} \sum_{i=1}^{N_{\mathrm{R}}(t_k)} \frac{1}{2} \mathbf{I}_i (\boldsymbol{\omega}_i(t_k) - \boldsymbol{\omega}_{\mathrm{R}})^2}{\sum_{k=1}^{S} N_{\mathrm{R}}(t_k)} \right). \tag{4.10}$$

4.1.4 Pressure

The local pressure of the fluid is based on the fluid stress tensor, which is calculated using the Irving-Kirkwood relation [140]:

$$\langle \boldsymbol{\sigma}_{\mathrm{R}} \rangle = \frac{1}{V_{\mathrm{R}} S} \sum_{k=1}^{S} \sum_{i=1}^{N_{\mathrm{R}}(t_k)} \quad (m_i \left(\mathbf{v}_i(t_k) - \mathbf{u}_{\mathrm{R}}\right) \otimes \left(\mathbf{v}_i(t_k) - \mathbf{u}_{\mathrm{R}}\right) + \frac{1}{2} \sum_{j \neq i}^{Nsys(t_k)} \sum_{a} \sum_{b} \frac{\mathbf{r}_{ab} \cdot \mathbf{f}_{ab}}{r_{ab}^2} (\mathbf{r}_{ab} \cdot \mathbf{r}_{ij})), \tag{4.11}$$

where N_{sys} is the number of molecules in the system, $\mathbf{r}_{ab}$ is the separation vector of sites a and b, and $\mathbf{r}_{ij}$ is the separation vector between the centre of mass of molecules i and j. It should be noted that sites a and b belong to different molecules as only intermolecular forces are required [22]. The normal pressure of the fluid is:

$$\langle P_{\mathrm{R}} \rangle = \frac{1}{3} \mathrm{Tr}(\langle \boldsymbol{\sigma}_{\mathrm{R}} \rangle), \tag{4.12}$$

where Tr is the trace operator of a tensor. This definition of pressure is based upon the virial expression (right-hand term in Eq. 4.11) which assumes that the fluid is contained within hard walls, however this assumption remains valid in periodic systems [20].

The definition of pressure given by Eqs. 4.11 and 4.12, requires an additional correction term to account for the missing force contribution that stems from the truncation of the Lennard-Jones pair potential, discussed in Section 1.3. The pressure is modified to $\langle P_{\mathrm{R}} \rangle + P_{\mathrm{R}}^{cor}$, where the pressure correction is defined as:

$$P_{\mathrm{R}}^{cor} = \left(\frac{32}{9}\right) \pi \rho_{\mathrm{R}}^2 r_c^{-9} - \left(\frac{16}{3}\right) \pi \rho_{\mathrm{R}}^2 r_c^{-3}. \tag{4.13}$$

The pressure correction is always negative and the magnitude can be in the region of 20 MPa for water at atmospheric conditions.

4.1.5 Axial Distribution Function

The axial distribution function (ADF) provides a measure of fluid structuring in one dimension, which is of particular importance for fluids highly confined within nanotubes. ADF measurement uses a combination of zonal and bin measurement techniques and is defined as [118]:

$$g(x) = \frac{\dfrac{1}{SV_b}\displaystyle\sum_{k=1}^{S} N_b(t_k)}{\dfrac{1}{SV_{\mathrm{R}}}\displaystyle\sum_{k=1}^{S} N_{\mathrm{R}}(t_k)}, \tag{4.14}$$

where N_b is the number of molecules in bin b and V_b is the volume. The numerator is the local density in bin b and the denominator is the total density within the sampling region R. Bulk fluids with homogeneous density distributions will have a constant ADF of 1 in all directions, since local fluid structuring will not be present.

4.1.6 Drag force

The average drag force on a surface can be evaluated by using the average force per surface molecule, given by:

$$\langle \mathbf{f}_{\mathrm{R}} \rangle = \frac{\displaystyle\sum_{k=1}^{S} \sum_{i=1}^{N_{\mathrm{R}}(t_k)} \mathbf{f}_i(t_k)}{\displaystyle\sum_{k=1}^{S} N_{\mathrm{R}}(t_k)}, \tag{4.15}$$

where $\mathbf{f}_i(t_k)$ is the instantaneous force vector on surface molecule i. The total average drag force is then calculated by multiplying the result of Eq. 4.15 by the number of surface molecules.

4.1.7 Hydrogen bonding in water

A hydrogen bond is the intermolecular interaction between a positively charged hydrogen of one water molecule and the negatively charged oxygen of another. Hydrogen bonds are stronger than van der Waals interactions but weaker than the covalent bonds between the hydrogen and oxygen of the same water molecule. The average number of hydrogen bonds per water molecule is calculated as:

$$\langle H_{\mathrm{R}} \rangle = \frac{\sum_{k=1}^{S} \sum_{i=1}^{N_{\mathrm{R}}(t_k)} H_i(t_k)}{\sum_{k=1}^{S} N_{\mathrm{R}}(t_k)} \tag{4.16}$$

where $H_i(t_k)$ is the instantaneous number of hydrogen bonds molecule i is part

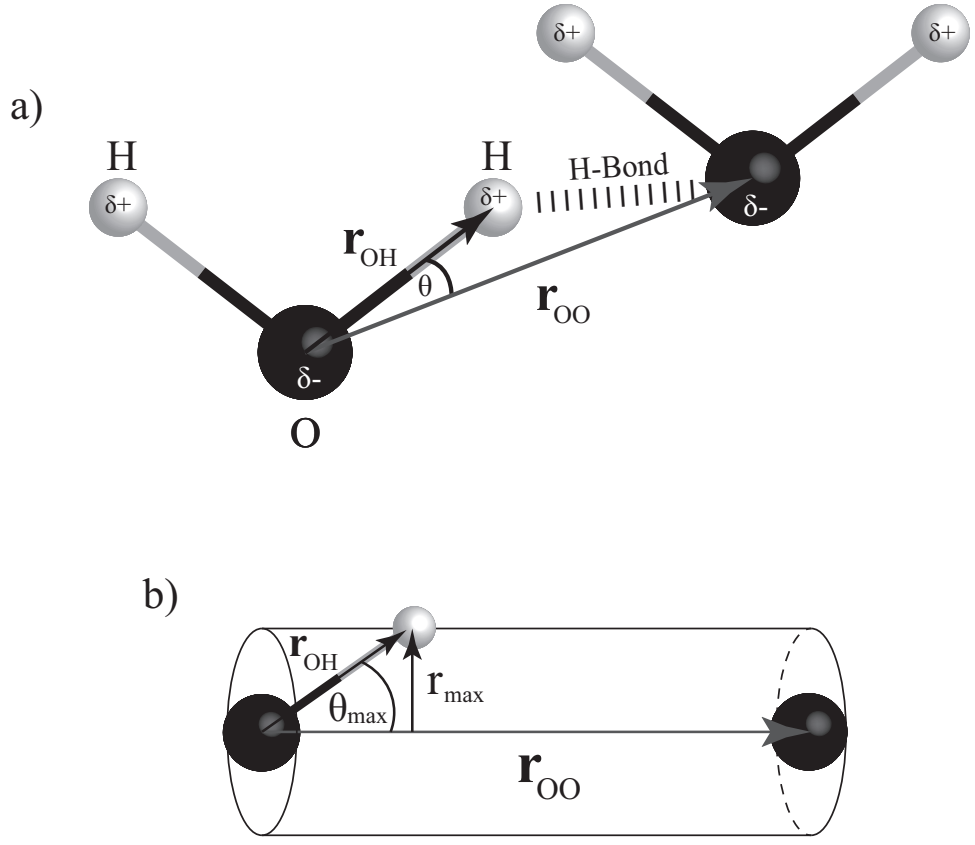

Figure 4.2: a) Illustration of a hydrogen bond in MD, and b) cylindrical region used to determine if a hydrogen bond is present.

of. For one water molecule to be hydrogen bonded to another it must fulfill the following criteria, according to [127]:

1. the magnitude of the vector between the oxygen atoms of the candidate water molecules $\mathbf{r}_{\mathrm{OO}}$, shown in Fig. 4.2a), must be less than 0.35 nm;

2. the angle made between $\mathbf{r}_{\mathrm{OO}}$ and the OH bond vector of the donor molecule $\mathbf{r}_{\mathrm{OH}}$ must be less than or equal to 30°.

These conditions can be realised as a cylindrical region between the candidate water molecules, the radius of which is related to the maximum allowable angle between $\mathbf{r}_{\mathrm{OO}}$ and $\mathbf{r}_{\mathrm{OH}}$, shown in Fig. 4.2b). The axis of the cylinder lies on $\mathbf{r}_{\mathrm{OO}}$ and its length is equal to the magnitude of $\mathbf{r}_{\mathrm{OO}}$. If a hydrogen atom lies within this cylindrical volume then a hydrogen bond is present and both water molecules are updated in the code to include this.

4.1.8 Normalised histogram of water dipole orientation

The positive hydrogen and negative oxygen atoms of a water molecule set up a dipole vector which lies along the bisector of the angle made by the two hydrogens. The orientation of this dipole and its dynamic behaviour in confined spaces has become a topic of interest as it is believed to be related to the unexpected behaviour of water inside CNTs. Water molecule orientation is measured by using the angle between the water dipole moment and a specified vector (typically the CNT axis), shown in Fig. 4.3.

The normalised histogram is constructed as follows:

1. set the range of angles over which the measurement is being made, e.g. 0 to 180 degrees;

2. specify the angle interval (e.g. 3 degrees) which is used to discretise the entire range of angles into bins;

3. measure the angle between the dipole moment and the reference vector ϕ;

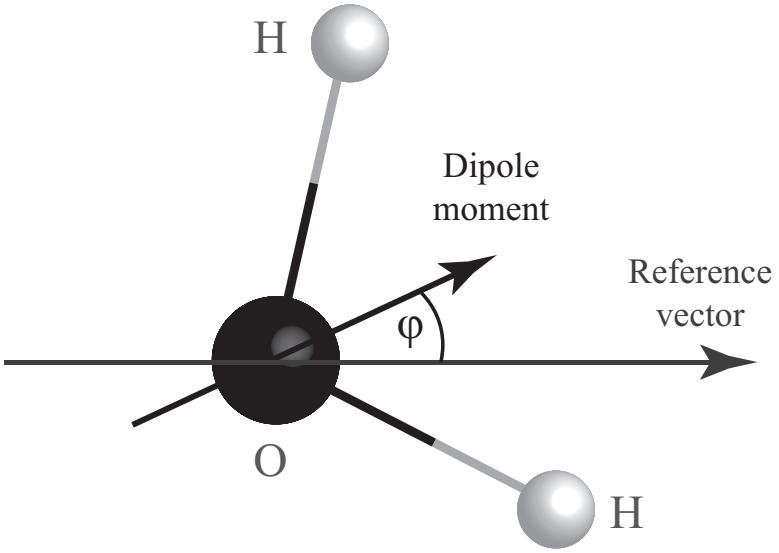

Figure 4.3: The orientation of the water dipole moment.

4. identify which bin the measured angle belongs to and add a count of 1 to that bin;

5. establish which angle interval is most common (i.e. the bin with the maximum number of counts) and divide all bin values by this maximum.

4.2 Boundary Conditions

One of the least explored areas in MD research is the application of physically realistic boundary conditions to generate fluid transport. Engineering applications at the nanoscale often require a pressure driven flow in MD simulations, e.g. water transport in a nanotube (or nanochannel), for which various techniques exist that are discussed shortly.

MD simulations are typically modelled as fully periodic systems, with periodic boundary conditions (PBCs) employed at all boundaries of the domain. PBCs provide us with a way of modelling a very small volume of fluid which is representative of a much larger volume – greatly reducing the computational demands of MD, enabling larger time scales to be accessed with the same computational resources. For this reason alone, PBCs have proven to be the most popular BC

in MD.

Despite their popularity, PBCs are limited in their application. For example, PBCs cannot be applied to an inlet of a domain that has a different geometry from the outlet. Such a scenario requires the implementation of non-periodic boundary conditions (NPBCs) in one dimension. NPBCs differ from PBCs in that they are independent and not associated with any other boundary in the domain. There are many other scenarios where the application of NPBCs is necessary at individual and independent boundaries of an MD domain. For example, open-systems and hybrid MD-continuum coupled simulations [38, 141–143].

Unlike conventional CFD, boundary conditions in MD can be applied globally or locally in the simulation domain. For example, traditional barostats (which control pressure and density) apply boundary conditions globally as they rescale the dimensions of the entire simulation domain, and the positions of molecules therein, although the total number of molecules remains fixed [22]. Simple thermostats, such as the Berendsen thermostat [144], can control fluid temperature globally or locally within the domain by rescaling all molecular velocities or only for those molecules in a local region.

The majority of the work in this thesis involves fluid transport through CNTs, therefore the focus of this chapter is on how to model boundary conditions for this flow problem. However, most of the boundary conditions described here could be adapted for a variety of flow scenarios. We begin by summarising existing techniques for simulating fluid transport in a nanotube, followed by an explanation of the approaches which have been adopted in our work.

There are two common approaches to investigate pressure driven flows in nanotube systems using MD, shown in Fig. 4.4. The first technique involves modelling a section of the nanotube, and applying periodicity in the streamwise direction, thereby ignoring inlet and outlet effects [93, 104, 109, 145].

A technique for generating fluid flow in this type of configuration is the gravitational field method [146], which applies a gravity force to all molecules in the

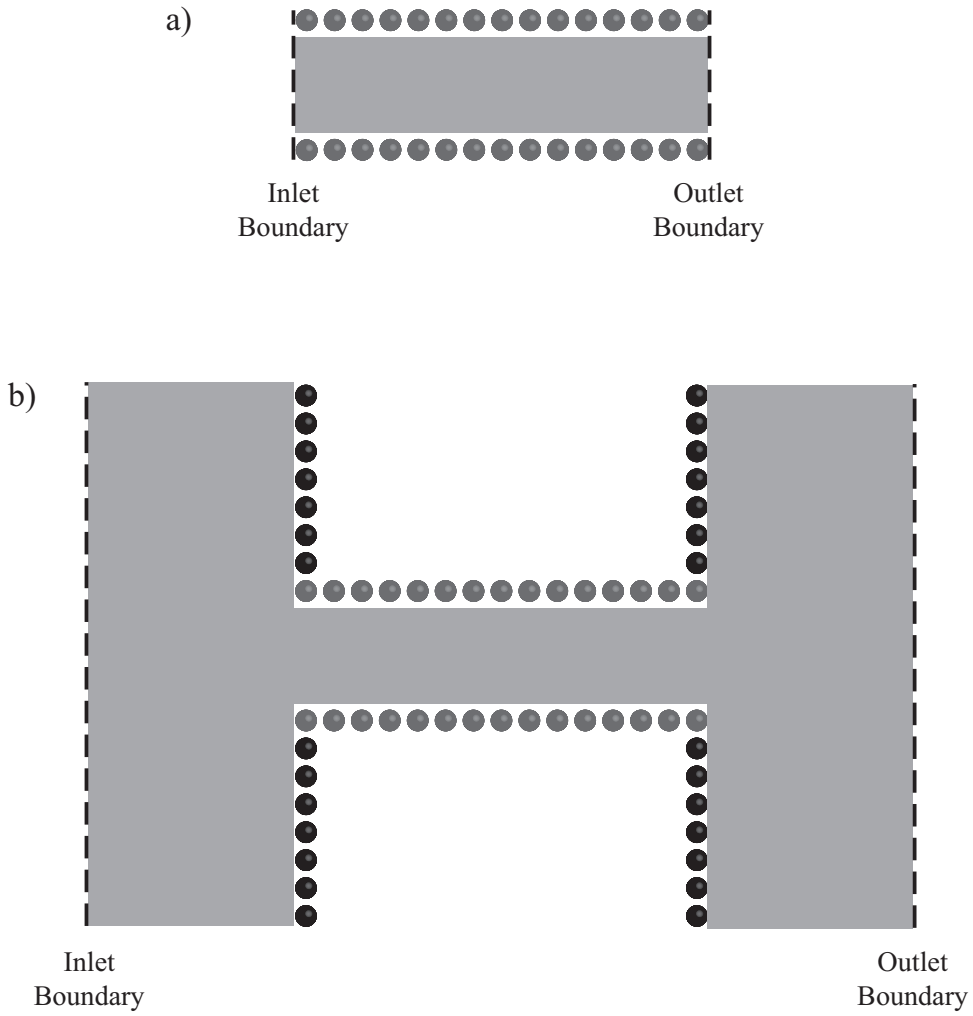

Figure 4.4: Two different approaches for modelling pressure driven flow through a nanotube: a) only the nanotube has periodic boundary conditions at the inlet and outlet of the nanotube, and b) including two fluid reservoirs at either end of the nanotube.

tube. The applied force can be a magnitude greater than the earth's gravitational pull in order to overcome the intermolecular forces. The external gravity force mimics a pressure gradient along the nanotube when used in conjunction with periodicity in the streamwise direction [109]. For smaller nanotube diameters, the fluid density is not easily defined, and so there exists an uncertainty about the actual applied pressure gradient.

Another technique to establish a pressure gradient within a nanotube with streamwise periodicity is the reflective particle membrane (RPM) method [147]. A semi-permeable membrane is superimposed on the periodic boundary in the

axial direction. Molecules are allowed to pass freely across the boundary in the flow direction, but have a probability of 1-p for passing in the other direction and probability p of being specularly reflected back into the domain. The RPM sets up a density gradient across the nanotube, and as a result, a pressure gradient. The probability p is used to control the magnitude of the pressure gradient: larger values for p create greater pressure gradients. The main drawbacks of this method are that it is difficult to control the actual inlet/outlet pressures and an extensive trial and error procedure is required to set up the desired pressure gradient.

The second type of pressure-driven simulations examine fluid flow through nanotubes that are part of a membrane, and therefore requires fluid reservoirs at the inlet and outlet of the nanotube. The most popular method for generating a pressure difference across a nanotube membrane in fully periodic systems is the technique of Zhu *et al.* [123], where an external force is applied only to molecules located in a specific region in the upstream reservoir. While this technique creates a hydrostatic pressure difference across the membrane, the downstream reservoir density decreases and negative pressures have been recorded [99]. This does not realistically represent physical experiments, in which the downstream pressure is close to atmospheric conditions.

The RPM technique can also be used in simulations with two fluid reservoirs. In this arrangement, the RPM is located at the inlet of the upstream reservoir, which leads to it having a higher density than its downstream counterpart, generating a pressure difference across the membrane. Both the RPM technique and the method of Zhu *et al.* (external forcing) cannot be used to model the build-up of ions in a desalination MD simulation, as demonstrated by Corry [69].

There are also MD simulations that implement two fluid reservoirs with NPBCs in the streamwise direction. Huang *et al.* [148] proposed a method using two rigid self-adjusting plates located at the extremities of reservoirs either side of a nanoscale membrane. External forces are applied to the plates corresponding to the required constant pressures in each reservoir. This technique involves using

NPBCs in the flow direction but PBCs in the other two dimensions. This method has recently been developed [149] to include flexible self adjusting plates to reduce the effect the rigid plates have on the molecular distributions near them. The main disadvantage of this technique is that the number of molecules in the simulation is fixed, meaning that eventually the upstream reservoir will contain no fluid molecules and the simulation will end. To simulate longer time periods, large upstream reservoirs would be required which would come with a significant computational burden.

Firouzi *et al.* [150] performed dual control-volume non-equilibrium MD simulations of molecular separation by a nanoporous membrane. This technique generates pressure driven flow via a difference in chemical potential (fluid density) in each control volume. Particle insertions are performed randomly which may disturb the dynamics of the simulation. Any molecules which cross the extremities of the control volumes are deleted, making the simulations non-periodic in one direction. This type of simulation is an example of a grand canonical ensemble where chemical potential, domain volume and fluid temperature are constant but the total number of particles in the domain is allowed to fluctuate.

In this present work we use the new continuum boundary conditions of Borg *et al.* [1] to generate fluid transport using the fluid reservoir approach. Although this approach is more computationally demanding, it is more representative of a realistic experimental setup, and incorporates inlet and outlet effects which may be significant.

By introducing NPBCs and controlling state quantities in user-defined regions, we can impose continuum-like boundary conditions in the MD domain. An additional motive in developing these methods is to enable MD simulations to be included as part of hybrid continuum-molecular techniques; boundary conditions from the continuum solver are applied on the MD domain using these "controllers". The feedback algorithm used in OpenFOAM for converging a fluid property to a required value was originally developed by Borg *et al.* [1].

4.2.1 Temperature

Temperature control is exclusively performed throughout this work using the Berendsen thermostat [144]. This feedback technique involves re-scaling molecule translation velocities and angular velocities to converge the fluid to the correct temperature. This method does not conserve linear or angular momentum but comes with the advantage that it can be applied locally in MD domains. Fluid temperature is only controlled in the reservoirs and not inside the nanotube, as recommended by [121]. Both translational velocity and angular velocity are re-scaled using a scaling factor:

$$\chi = \left[1 + \frac{\Delta t_{\mathrm{MD}}}{\tau_t}\left(\frac{T_{\mathrm{R}}^{req}}{\langle T_{\mathrm{R}}\rangle} - 1\right)\right]^{(1/2)}, \tag{4.17}$$

where Δt_{MD} is the MD time step size, τ_t is a time constant which determines the rate of convergence, and T_{R}^{req} and $\langle T_{\mathrm{R}}\rangle$ are the required and measured temperatures in control region R. This thermostat acts to control fluid temperature through molecular kinetic energy: scaling factors less than 1 reduce the kinetic energy (and temperature) while scaling factors greater than 1 cause the energy to increase and fluid temperature follows suit.

4.2.2 Controlling fluid density to generate mass transport

Similar to the work of Firouzi *et al.* [150], we control the density of the fluid reservoirs to create a chemical potential and generate mass transport through the membrane. The density control region inside the upstream reservoir is shown in Fig. 4.5; the configuration in the downstream reservoir is identical and therefore not shown. Unlike Firouzi *et al.,* molecule insertions and deletions are not performed randomly. For insertion, the USHER algorithm [151] is used which searches for a site within the potential energy landscape via a steepest descent iteration scheme. A molecule is inserted if the potential energy of the prospective site is equal to the cell-averaged potential energy. In this way, the algorithm

ensures that the inserted molecule does not overlap with existing molecules while ensuring minimal local potential energy changes. Similarly for deletion, the candidate molecule is chosen with its potential energy closest to the cell-averaged potential energy. Momentum and energy conservation steps are also performed after a molecule is inserted/deleted by distributing the added/removed momentum to neighbouring molecules, and updating the pair-forces.

As the density of the fluid increases, the number of insertion sites which correspond to the average potential energy of the cell becomes less until no more molecules can be inserted into the control region. Tolerances can be set by the user to insert molecules within a specific range of potential energy values relative to the cell average value, e.g. 10% of cell average potential energy. The greater the tolerance value, the easier it is to insert molecules, but this can lead to significant disturbances in the fluid properties and is not recommended. We found that inserting within 20% of the cell average potential energy did not lead to significant variations in fluid temperature or pressure and facilitated fast molecule insertion.

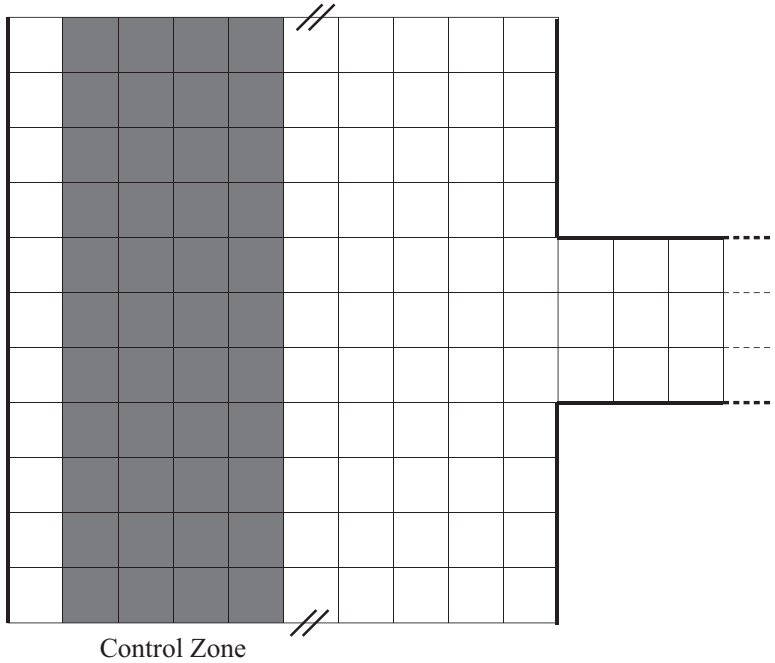

Figure 4.5: Schematic of upstream reservoir control zone to maintain the fluid at the density specified by the user. PBCs are indicated by the short double black lines.

Density control is performed away from the membrane so as not to disturb the regions of the fluid which are of interest to us, as illustrated in Fig. 4.5. PBCs are employed perpendicular to the flow, while NPBCs are applied in the flow direction: both the inlet and outlet domain boundaries are specular-reflective walls which help to control fluid density in the reservoirs. Berendsen thermostats are applied to each reservoir to maintain a constant system temperature and eliminate the contribution of any temperature gradients to the fluid transport.

The number of molecules which are required to be inserted or deleted over a specified time interval, $t \rightarrow t_n$, is calculated as follows for each cell, P, in the control zone:

$$\Delta N_{\mathrm{P}}(t \rightarrow t_n) = \mathrm{NINT}\left(\left[\rho_{\mathrm{P}}^{req}(t_n) - \langle \rho_{\mathrm{P}} \rangle (t)\right] V_{\mathrm{P}}\right), \tag{4.18}$$

where NINT is the nearest integer function, as only whole molecules can either be inserted or deleted, $\rho_P^{req}(t_n)$ is the required number density at the new time t_n, $\langle \rho_{\mathrm{P}} \rangle (t)$ is the measured density at the old time t, and V_{P} is the cell volume. Full details of the USHER algorithm used in OpenFOAM can be found in [19].

As part of this work, the USHER algorithm was updated to include the insertion/deletion of polar, polyatomic molecules according to [152]. This involved updating the potential energy calculation to include electrostatic contributions, and incorporating molecule rotations during the site searching algorithm, in addition to the original translational displacement. Results using this simulation approach are presented in Chapter 6.

4.2.3 Controlling pressure to generate mass transport

We find that it is more effective to explicitly control the pressures in the upstream and downstream reservoirs, and therefore the resulting pressure difference across the membrane. Upstream, the fluid pressure is controlled through state constraints of pressure and temperature, while density is adaptively controlled.

Downstream of the membrane, an open-system [143] is adopted that enables pressure to be controlled whilst allowing flow through the system to develop without being over-constrained.

Periodic boundary conditions are employed in the transverse directions, while non-periodic boundary conditions are applied in the streamwise direction: the left-hand boundary is a specular-reflective wall, while the right-hand boundary deletes molecules upon collision. The wall helps control the fluid pressure and density upstream while the deletion patch creates an open system [143].

The upstream pressure is controlled using a proportional-integral-derivative (PID) control feedback loop algorithm in addition to adaptive control of density at the inlet. Downstream of the membrane, pressure is controlled using a pressure-flux technique which was originally used in hybrid MD-CFD simulations [153].

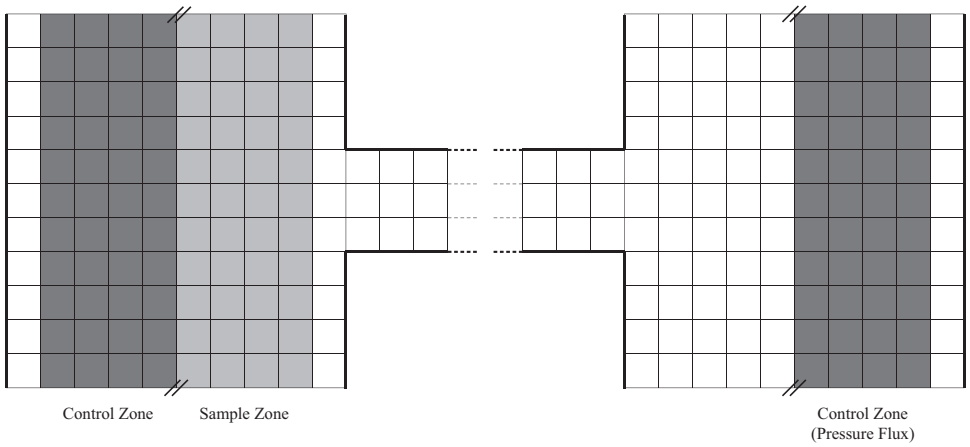

Figure 4.6: Schematic of control and sampling regions in the upstream and downstream reservoirs. PBCs are indicated by the short angled black lines.

Upstream reservoir

An external force is distributed over all molecules that reside in the upstream control zone, to create the required pressure in the neighbouring sampling region, shown in Fig. 4.6. The required external force is calculated using three separate components: a proportional term, an integral term, and a derivative term. The proportional force term is calculated from the pressure error $e_p = P_{\mathrm{R}}^{\mathrm{req}} - \langle P_{\mathrm{R}} \rangle$ be-

tween the measured pressure in the sampling region $\langle P_{\mathrm{R}} \rangle$ and the target pressure $P_{\mathrm{R}}^{\mathrm{req}}$:

$$\mathbf{f}_p = K_p \frac{e_p A \hat{\mathbf{n}}}{N}, \tag{4.19}$$

where A is the cross-sectional area of the control zone, $\hat{\mathbf{n}}$ is a normal vector indicating the direction of the applied force, K_p is the proportional gain (dimensionless), and N is the number of molecules in the control region. The integral force term is calculated using the accumulation of past pressure errors:

$$\mathbf{f}_i = K_i \frac{\left(e_p^n + e_p^o\right) \Delta t_{\mathrm{MD}} A \hat{\mathbf{n}}}{2N}, \tag{4.20}$$

where e_p^n is the pressure error at the new time step n, e_p^o is the accumulated pressure error at the old time step o, and K_i is the integral gain (units are s^{-1}). The derivative force term is calculated using the rate of change of the pressure error:

$$\mathbf{f}_d = K_d \frac{\left(e_p^n - e_p^o\right) A \hat{\mathbf{n}}}{\Delta t_{\mathrm{MD}} N}, \tag{4.21}$$

where K_d is the derivative gain (units are s). The equation of motion for a molecule, j located in the control zone is then:

$$\mathbf{a}_j = \mathbf{f}_j / m_j + \mathbf{f}_t^{\mathrm{ext}} / m_j, \tag{4.22}$$

where $\mathbf{a}_j$ is the acceleration of molecule j, m_j is the molecule mass, $\mathbf{f}_j$ is the total intermolecular force, and $\mathbf{f}_t^{\mathrm{ext}}$ is the total external force given by the sum of all three PID components:

$$\mathbf{f}_t^{\mathrm{ext}} = \mathbf{f}_p + \mathbf{f}_i + \mathbf{f}_d. \tag{4.23}$$

Molecules that move from the upstream reservoir into the nanotube must be accounted for so as to maintain the reservoir in a steady thermodynamic state. A general adaptive method for control of density is used since both pressure and temperature in this region are already constrained at the desired values. We implement a new mass flux method by controlling density in the control zone at

the boundary to be equal to the measured fluid density in the sampling region. A steady homogeneous density distribution is always achieved because the pressure controller forces molecules in or out of the control zone. We use relaxation to improve the stability of our algorithm, so the target density within the control zone is given by:

$$\rho^{req} = \beta\langle\rho_{sz}\rangle + (1-\beta)\langle\rho_{cz}\rangle, \tag{4.24}$$

where $\langle\rho_{sz}\rangle$ is the measured density in the sampling zone, $\langle\rho_{cz}\rangle$ is the measured density in the control zone, and β is a relaxation parameter (e.g. $\sim$0.5). The number of molecules to insert/delete in control zone 1 is then:

$$\Delta N = \frac{(\rho^{req} - \langle\rho_c\rangle)V_{cz}}{m_i}, \tag{4.25}$$

where V_{cz} is the volume of the control zone. Molecule insertions/deletions are performed as described previously. This pressure control technique is best applied in the following way to converge the upstream reservoir to the correct state point:

1. equilibrate the fluid to the correct temperature;

2. turn on the proportional and integral terms of the PID controller ($K_p = 1$, $K_i = 100$ and $K_d = 0$) and adaptive density control;

3. once the fluid pressure begins to fluctuate about the required value, turn on the derivative term ($K_d = 20$).

We found that including the derivative term during the initial stages of pressure control leads to extremely large external forces, due to the highly fluctuating nature of pressure during this period, causing the simulation to crash. This problem was remedied by performing an equilibration stage using only the proportional and integral terms of the PID controller. This pressure control technique proved to be applicable at high pressures, but at low pressures the magnitude of pressure fluctuations are much greater than the required value meaning that the derivative

term constantly introduced instabilities. Therefore it is not recommended to use the PID control technique to converge a fluid to near-atmospheric conditions.

Downstream reservoir

The pressure in the downstream reservoir is set by applying an external force to all molecules in the control zone [153], shown in Fig. 4.6:

$$\mathbf{f}^{\text{ext}} = \frac{\alpha P^{\text{req}} A \hat{\mathbf{n}}}{N}, \tag{4.26}$$

where P^{req} is the target pressure and α is a tuning parameter. We found that this particular pressure control technique was more effective at low fluid pressures as it is not based on a feedback loop algorithm. However, a trial and error procedure to tune α is required to set the fluid at the correct pressure, which is why it is not used upstream.

4.3 Summary

In this chapter we outlined MD measurement techniques and boundary conditions used throughout this work. Building on the original measurement framework created by Borg [19] we have extended the models to measure hydrodynamic properties of polyatomic fluids. We also included a description for measurement of the axial distribution function and the average total drag force acting on a molecular surface. The procedure for measuring hydrogen bonding and dipole orientation of water molecules was also described.

Two novel approaches to generate fluid transport through a nanotube membrane between two fluid reservoirs were described in Sections 4.2.2 and 4.2.3. The first involved controlling fluid density in the reservoirs to create a chemical potential across the membrane, implicitly controlling pressure. While this technique is effective, it is more advantageous to be able to control fluid pressure in the reservoirs explicitly.

Fluid pressure in each reservoir can be applied explicitly by using two different techniques: a proportional-integral-derivative (PID) feedback algorithm upstream and a pressure flux method downstream. We found that the PID method is more effective at higher pressures while the pressure flux technique is applicable at low pressures. Advice about using this pressure control technique was outlined in Section 4.2.3.

Chapter 5

Liquid Argon Flow In and Around CNTs

5.1 Introduction

Modelling fluid interactions with CNTs is vital for many nanoscale applications, as discussed in Chapter 1. The design and performance of such systems is dependent upon our understanding of flow phenomena at this scale. Liquids under extreme confinement behave very differently to those at a macroscopic level, with the presence of fluid layering, molecular ordering and unexpectedly high molecular mass transport.

Ordered fluid structures adjacent to solid surfaces occur due to the interaction of the solid and fluid molecules. This is commonly referred to as the "interface region", where the local fluid density deviates from the bulk value [154]. These ordered structures generally dissipate at distances of several molecular diameters from a solid surface. However, if the fluid is confined in a channel which is not wide enough, these ordered structures will persist across the channel width.

Travis *et al.* [10] and later Travis and Gubbins [155] demonstrated using MD that, in a channel of five molecular diameters width, flow behaviour could not be accurately described by the Navier-Stokes (NS) equations. Velocity profiles

deviated significantly from hydrodynamic predictions. However, they also found that in a channel which was 10 molecular diameters wide the NS equations were valid. The breakdown in the accuracy of hydrodynamic predictions was attributed to the application of a local version of Newton's law of viscosity, which is invalid if the fluid is highly inhomogeneous – common under extreme confinement. Xu and Zhou [156] studied pressure-driven liquid argon flow between parallel platinum plates 4 nm apart using MD, and found that increasing the shear-rate (driving force) led to an increase in fluid viscosity and the development of non-Newtonian fluid behaviour. Ziarani and Mohamad [157] found good qualitative agreement between an analytical solution of the NS equations and results from MD of liquid flow in a 7 nm wide channel.

From these findings, it is clear that a criterion exists where the scale of a flow problem becomes too small to be modelled using a continuum technique and a molecular approach must be adopted. Establishing at what length scale this "continuum breakdown" occurs in a liquid is difficult, and no single parameter can be used. The findings of Travis *et al.* [10], and Travis and Gubbins [155], do however provide some insight into the transition to non-continuum fluid behaviour.

It is not only confinement that can produce unexpected fluid behaviour but also the material through which the fluid is being transported. Supple and Quirke [158] showed through MD simulations that oil was rapidly imbibed into a 1.8 nm diameter CNT at ∼445 m/s and the filling did not obey the macroscopic Washburn equation. Skoulidas *et al.* [159], and later Ackermans *et al.* [160], demonstrated using MD that argon gas was transported through CNTs almost three orders of magnitude faster than through zeolites and silicalite, respectively. Cannon and Hess [161] demonstrated, using non-equilibrium MD simulations, that liquid argon inside small diameter CNTs forms well-ordered fluid structures. They also found that flow rates increased towards the smallest diameter CNTs, and attributed this enhancement to the well-defined flow structure present in this range of CNT diameters.

It is also important to consider the effect that the set-up of the flow problem can have on results from an MD simulation. Huang *et al.* [149] investigated the influence of entrance and exit effects on fluid flow rate by simulating liquid argon flow through one nanopore of finite length and one which was infinitely long. Both nanopores had a diameter of 2.2 nm (and in the finite case the nanopore was 6 nm in length and separated two fluid reservoirs at different densities). The infinitely long nanopore was modelled using periodic boundary conditions and the fluid was driven by applying an external body force to all of the argon atoms in the system. Huang *et al.* found that the flow rate through the finite pore was ∼40% less than the infinitely long case and attributed this decrease to entrance and exit effects. A comparison of these simulation approaches is discussed in Section 4.2.

The development of a molecular dynamics simulation is dictated by the choice of interaction parameters. Ideally these values should be derived from experimental or quantum chemistry methods, however this is not always possible. The interaction of different species in a MD simulation is often obtained by "mixing" rules that use the parameters for similar species interactions (e.g. argon-argon and carbon-carbon) to derive a set of values for inter-species interaction (e.g. argon-carbon). This mixing of parameters has led to a broad range of values characterising the interaction between argon and carbon in the literature, ranging from hydrophilic to hydrophobic representations, which may introduce inaccuracies in an MD simulation [162].

Nagayama and Cheng [154] used MD to investigate the effect of surface wettability on liquid argon flow in a nanochannel. They found that a hydrophobic surface has less interfacial resistance than a hydrophilic one, and that this led to a plug flow velocity profile as opposed to a parabolic one. They claim that the reduction in interfacial resistance stems from a gap that exists between the liquid and the hydrophobic surface which leads to frictionless flow. Mao and Sinnott [163] also found that molecular diffusion through CNTs was strongly af-

fected by the molecule-nanotube interactions. The hydrophobic nature of CNTs is believed to be one of the most influential features in their ability to rapidly transport fluids.

In this work we use the new continuum boundary conditions of Borg *et al.* [1] to generate fluid transport. By introducing non-periodic boundary conditions (NPBCs), and controlling state quantities in user-defined regions, we can impose continuum-like boundary conditions in the MD domain. An additional motive in the development of this method is that it enables MD simulations to be included as part of a hybrid continuum-molecular technique [38, 141–143]: boundary conditions from the continuum solver are applied on the MD domain using these "controllers".

Interacting Pair (i,j)	ϵ_{ij} (J)	σ_{ij} (m)
Ar-Ar	1.6567×10^{-21}	3.4×10^{-10}
Ar-C	1.9646×10^{-21}	3.573×10^{-10}

Table 5.1: Lennard-Jones parameters for initial cases, taken from [6].

Two different problems are addressed in this chapter: liquid argon in cross-flow around a CNT, and a CNT linking two reservoirs of liquid argon at different densities. The parameters we used for the Lennard-Jones interactions for both cases are listed in Table 5.1. A cut-off radius of 0.8 nm was used for both argon-argon and carbon-argon pairs. In all simulations the carbon atoms of the nanotubes were "frozen" to their original positions, making the nanotubes rigid, in order to reduce the computational time required for the simulations [6, 38].

5.2 Liquid argon flow past a CNT

In this section, we perform MD simulations to investigate one of the classic problems in fluid mechanics: a cylinder in uniform fluid cross-flow. In this scenario, the cylinder is a (12,12) CNT with a diameter of 0.9422 nm and the fluid is liquid

argon at 95 K and 1342 kg/m^3. The aim of this work is to demonstrate that by introducing novel NPBCs we can reproduce results from a larger periodic system whilst reducing the computational cost of the MD simulation significantly.

5.2.1 Fully periodic system

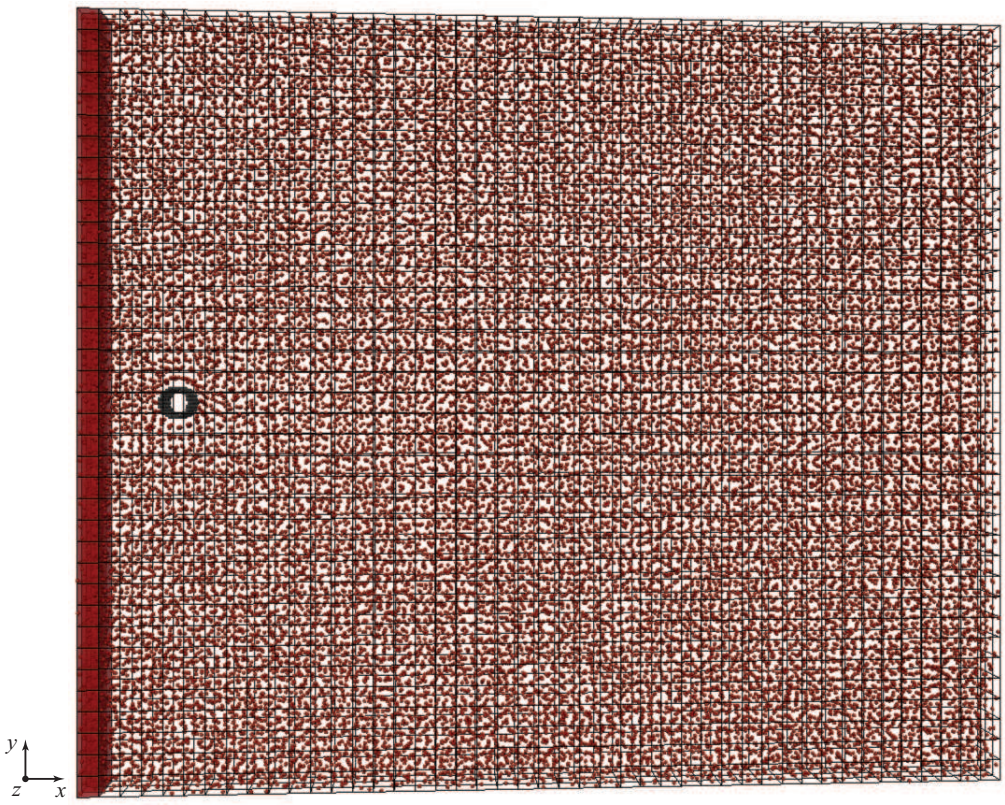

Figure 5.1: Fully periodic simulation domain for cross-flow of liquid argon over a CNT, with the control zone highlighted.

We begin by replicating an MD simulation performed by Tang and Advani [6], who demonstrated that classical continuum mechanics cannot be used to calculate drag on a CNT. They compared their MD results, of a fully periodic system, with a finite element analysis using the same flow conditions, and found that drag forces in the MD simulation were considerably larger.

The domain size is 30.56 $\times$ 25.47 $\times$ 2.23 nm in the x, y and z directions, respectively, and periodic boundary conditions are applied in every direction.

The simulation domain is shown in Fig. 5.1. Tang and Advani performed domain size tests in their work and found that the drag force on the CNT converged using these dimensions. The total simulation time is 2.15 ns using a time step of 2.15 fs. The interaction between all molecules in the system is represented using the Lennard-Jones potential and the parameters for this potential are listed in Table 5.1. The total number of argon atoms in the domain is 36 400, which is in agreement with [6].

A uniform flow of argon is created by controlling the velocity of molecules upstream of the CNT in a user defined zone, shown in Fig. 5.1. The control zone is located 0.9 nm from the CNT, in accordance with [6]. When molecules are controlled, their velocities are replaced by random velocities from a Maxwellian distrubtion at the required temperature. The required bulk streaming velocity is then also superimposed onto the molecule. This technique creates uniform flow and removes any excess heat in the system. The freestream velocity is controlled to 80 m/s every 50 time steps throughout the duration of the simulation, which is the same method used by Tang and Advani to generate uniform flow and was first reported by Rapaport [20]. After filling the simulation domain with molecules, the system is converged to the correct conditions over 300 000 time steps before measurements are taken.

5.2.2 Partially periodic system

The main properties from this simulation in which we are interested are the velocity profiles around the CNT and the drag forces acting upon it. Therefore the domain size need only be large enough to apply the correct boundary conditions and include a sufficient amount of fluid surrounding the CNT, at the required state point, for accurate drag measurement. By reducing the size of the domain we can decrease the associated computational cost of the simulation.

However, continuing to use a fully periodic system in this situation is not possible. In the flow direction, a reduced density region is created immediately

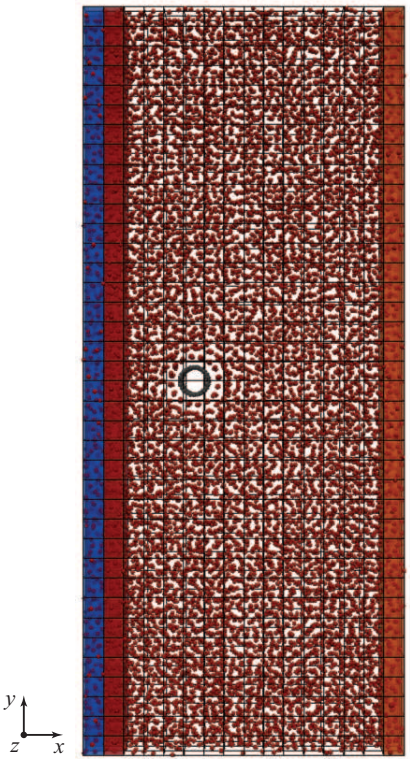

Figure 5.2: Partially periodic simulation domain for cross-flow of liquid argon over a CNT, with the control zone highlighted.

downstream of the CNT which would then be reintroduced at the inlet of the domain if periodic boundary conditions were used, significantly affecting the results. In order to reduce the size of the domain, we must therefore use NPBCs in the flow direction. Here, the domain size was reduced in the x direction, but not in the y and z directions in order to make results comparable.

The size of the domain was therefore reduced to 10.88 nm in the x direction, which matches a similar partially-periodic simulation by Werder *et al.* [38]. In their work, Werder *et al.* combine an MD simulation with a CFD solver to model liquid argon flow past a CNT, although the fluid properties are different to the current study and the MD system was periodic in two directions and non-periodic in the flow direction. Werder *et al.* control their fluid velocity by applying an external force to the molecules upstream of the CNT and by using moving specular walls at the domain boundaries in the flow direction; these techniques are explained in detail in [38].

In this present work, the periodic boundaries in the x direction are replaced by non-periodic boundaries with two boundary zones at the inlet and outlet of the domain, as shown in Fig. 5.2. Velocity control remains unchanged from the fully periodic case (controlling velocity at 80 m/s and temperature at 95 K). In additional to velocity control, molecules are inserted and deleted using the USHER algorithm in the control zone to ensure that the fluid density upstream remains at the correct conditions. Inserted molecules are assigned the required free stream velocity. A mass flow rate of molecules is imposed at the inlet of the domain to simulate inflow and reduce the burden on the density controller. This model inserts molecules in the upstream boundary zone based on a prescribed value, 5.7×10^{-12} kg/s in this case. Full details of this model can be found in [1]. The upstream boundary is modelled as a specular wall to help control density upstream of the CNT.

A deletion patch is specified at the outlet, which creates an open system. The downstream boundary zone is used to apply an external force on all molecules in this region to set the fluid at the required pressure. See Section 4.2.3 for more details about this model. The adjustable parameter α in Eq. 4.26 allows the external force to be scaled, e.g. if $\alpha = 1$ then the full external force is applied and if $\alpha = 0$ then the external force is zero. Four different α values are used in this study: 1, 0.67, 0.56 and 0. These values come from the normalisation of the external forces by the force required at bulk density and pressure. The pressure of argon at the given state point is $\sim$0.2 MPa, obtained from [164], and this value is used in Eq. 4.26 to calculate the value of the external force at each time step.

There are many models which exist to control fluid pressure at a non-periodic boundary, all of which rely upon *a priori* data and estimates, and this present method is no different. The required state point of the fluid at the outlet boundary is not known beforehand and may differ from bulk conditions. As such, choosing the correct value for α is difficult and is a common problem when using any boundary model. Werder *et al.* [38] apply an effective force on molecules in

the boundary region that is dependent upon the state point of the fluid in this region. This effective force is measured from previous MD simulations at the predicted state point. If the fluid properties differ from the predicted values then the effective force will be incorrect. Other boundary models are also dependent upon adjustable parameters such as the one used in this study. The dependence of results on α is discussed in the following section.

These non-periodic simulations require an initial equilibration time period, typically less than 0.5 ns, until the drag on the CNT has converged and the number of molecules in the system fluctuates about a constant value. The time averaging of properties commences after these conditions have been met. The time characteristics, e.g. total simulation time, of these simulations remain unchanged from the fully periodic case in Section 5.2.1 above.

5.2.3 Results

The streaming velocity profile obtained for the flow of liquid argon past a CNT in a fully periodic domain is presented in Fig. 5.3, and compared to the published data by Tang and Advani [6]. This velocity is measured across the centre of the nanotube in the y direction using a binning method to provide a spatial average. The sampling region is 0.48 nm wide and spans the entire height and depth of the domain. The profile is sampled every time step and averaged over $1{\times}10^6$ samples.

Case	α	Drag Force (N/m)	% Error
Fully periodic	–	0.00696	0
External force 1	1	0.00735	5.6
External force 2	0.67	0.00700	0.58
External force 3	0.56	0.00690	0.86
No external force	0	0.00618	11.2

Table 5.2: Measured drag forces on the CNT for different boundary conditions.

It is clear from Fig. 5.3 that Tang and Advani have not created the correct free

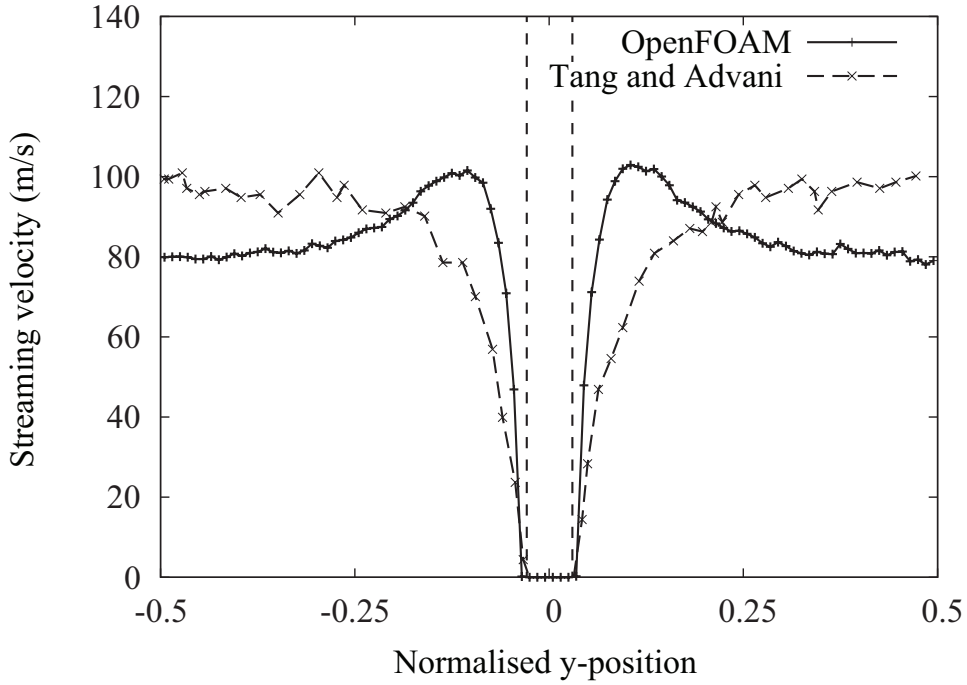

Figure 5.3: Streaming velocity profiles for flow past a CNT in a fully periodic system; the vertical dashed lines indicate the position of the CNT around $y = 0$.

stream velocity; the required value was 80 m/s, but their measured value is closer to 100 m/s. The free stream velocity measured in this present work matches the required 80 m/s very well. The liquid argon can be seen accelerating around the nanotube reaching a maximum velocity of $\sim$ 100 m/s; no such behaviour is present in the profile produced by Tang and Advani, although it has previously been shown by Werder *et al.* [38].

The average drag on the nanotube is measured using Eq. 4.15 to provide the average force per carbon atom. This value is then multiplied by the number of atoms in the CNT and divided by its length to obtain the average force per unit length of the nanotube. The drag forces (per unit length) for each simulation are listed in Table 5.2.

The boundary conditions used in both simulations are identical and yet the results are significantly different. All flow velocities reported by Tang and Advani are above the required values and with a lack of information regarding mass flow rate measurement, we suggest that an error is present in their work. We measure

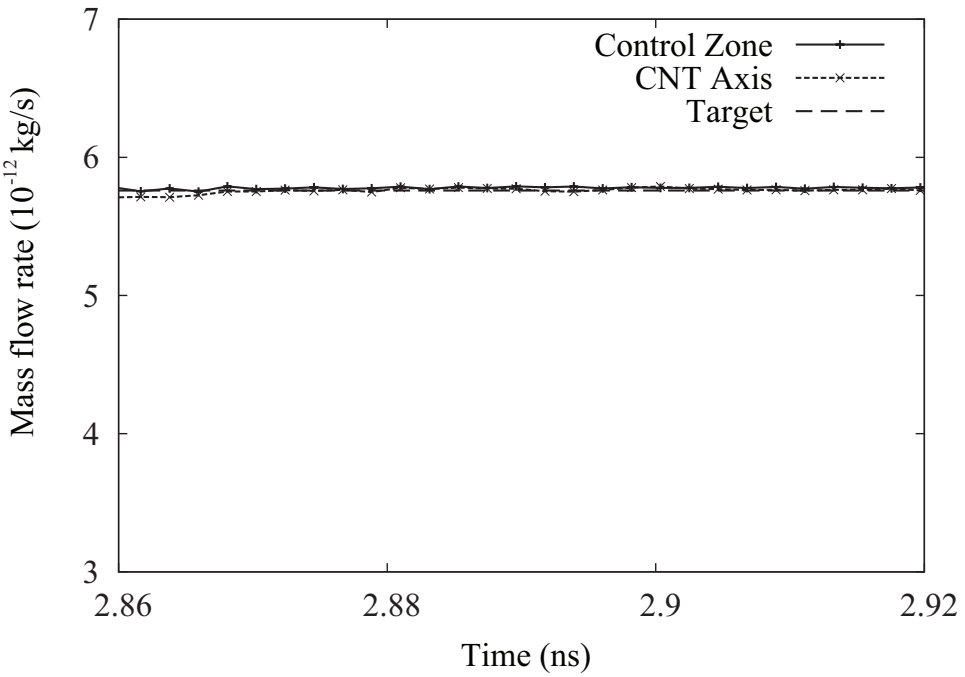

Figure 5.4: Measured mass flow rate at the inlet of the domain and across the CNT compared with the target value.

the mass flow rate in our simulation at the end of the control zone and along the centre axis of the CNT and these are compared in Fig. 5.4. These results show that mass flow is conserved throughout the domain and that the flow rate matches the required value. Tang and Advani provide no information about the fluid flow rate or fluid density surrounding the CNT. We would expect the fluid density to be at bulk conditions away from the CNT in the y direction, which would mean that the mass flow rate of Tang and Advani must be higher than required since the free stream velocity is well above the desired value.

The acceleration of flow close to the CNT, which is not reported in macroscopic solutions of this flow problem, is primarily due to the reduction in the cross sectional area through which the fluid can pass. Periodic boundary conditions are applied in the y direction so the problem is effectively being modelled as flow past an array of CNTs, meaning that the flow must accelerate as it passes around the CNT in order to conserve the mass flow rate. Another reason why the fluid accelerates close to the CNT surface is because of the local fluid structure in that

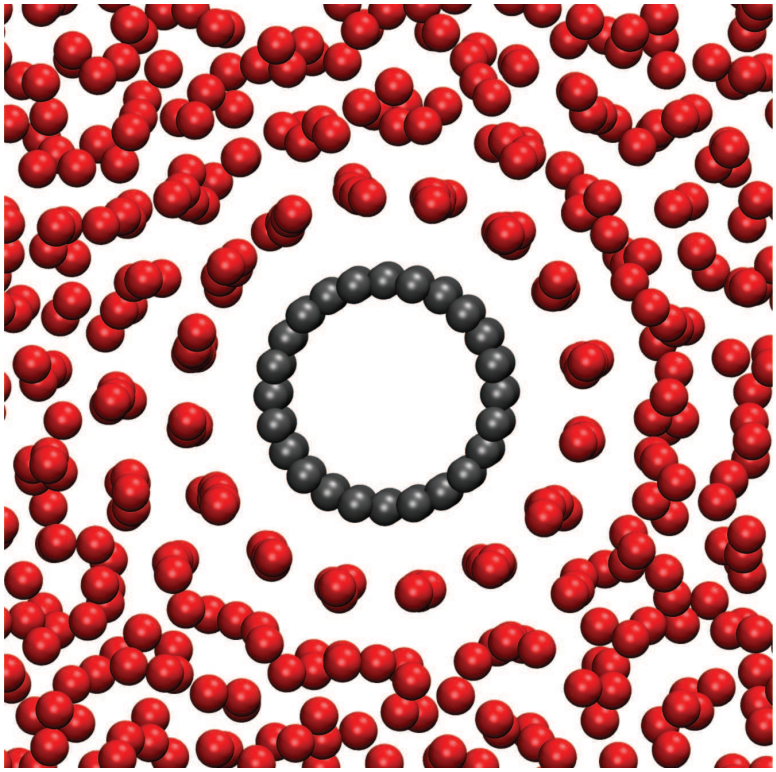

Figure 5.5: Snapshot of argon atoms forming a layered surface close to the CNT surface. The carbon atoms have been reduced in size for visual clarity.

region, which is now described.

A snapshot of the fluid structure around the CNT and the corresponding average radial density distribution are shown in Figs. 5.5 and 5.6, respectively. Liquid argon located adjacent to the CNT surface forms high density layers which dissipate beyond ∼2 nm from the CNT centre to bulk conditions. The phenomenon of liquid layering adjacent to a surface is well reported in the literature, as discussed previously. The layering structure of the fluid results in the density in the layer itself being higher, while the total density in the region close to the CNT surface is lower and hence the flow must accelerate. Since this layering effect occurs over a few nanometers, classical macroscopic solutions are not valid for a cylinder which is less than 1 nm in diameter.

The primary purpose of this study is not to assess the drag characteristics of a CNT but to investigate the effectiveness of using NPBCs in MD simulations. By introducing NPBCs we are able to reduce the size of the simulation domain

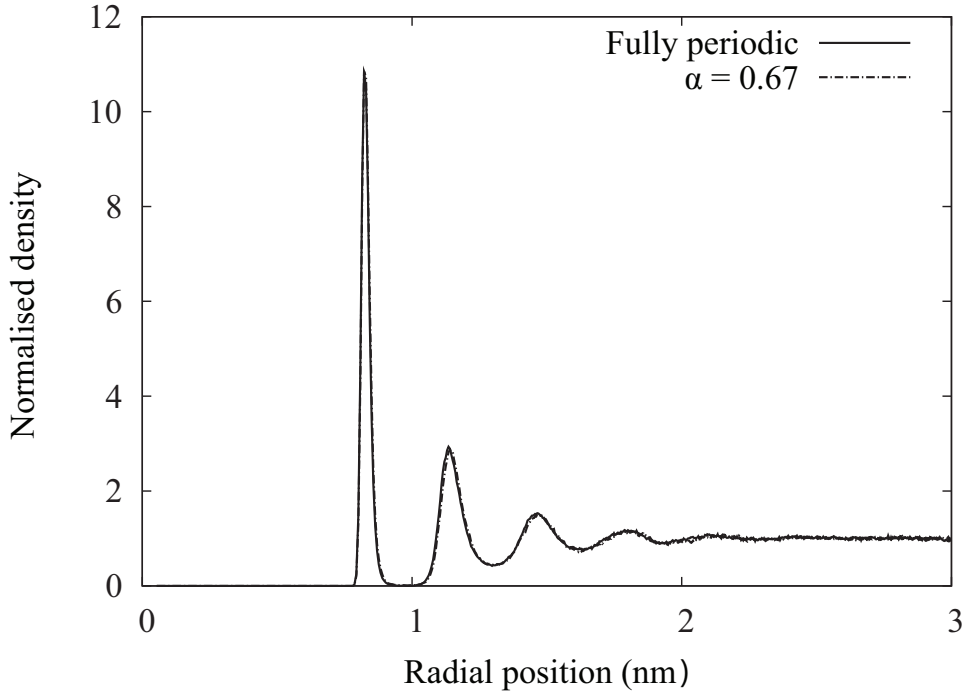

Figure 5.6: Radial density profile around the CNT for both the fully periodic case and the non-periodic case with an applied boundary force.

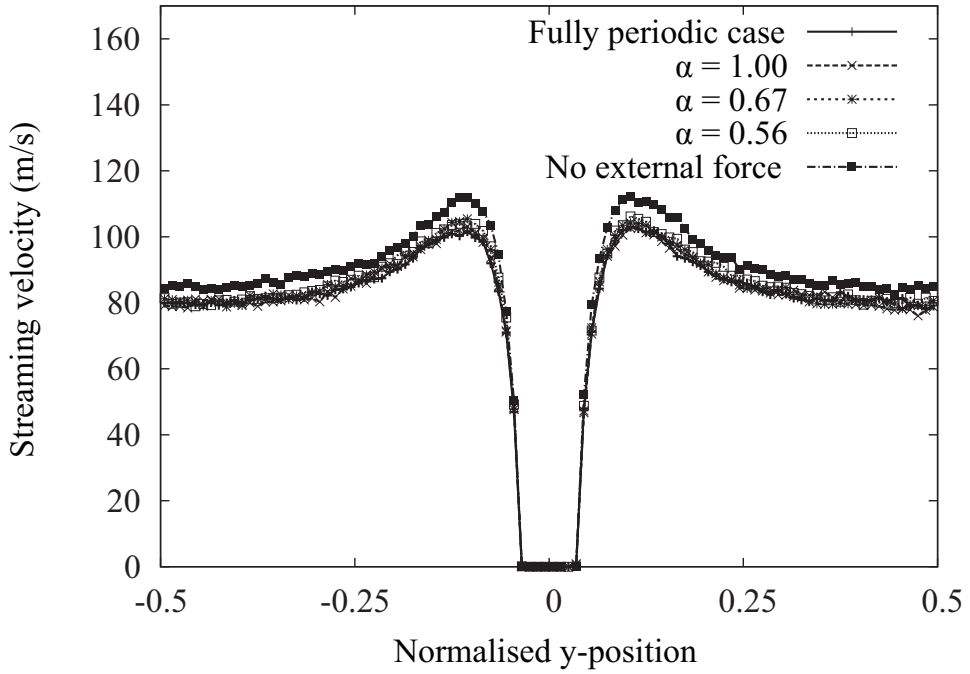

Figure 5.7: Streaming velocity profiles for flow past a CNT in a fully periodic system (PBC), and a system with non-periodic boundary conditions (NPBC) in one direction with different outlet boundary conditions.

and decrease the computation time of the problem significantly. Using the same velocity measurement techniques as the fully periodic case, we obtain the velocity profile across the CNT for different outlet conditions and compare these to results from the fully periodic case in Fig. 5.7. Drag measurements are also compiled and presented in Table 5.2.

The velocity profiles in the PBC and NPBC cases with an external force ($\alpha > 0$) are in very good agreement, in particular when $\alpha = 0.67$. However, when no external force is applied the velocity profile deviates from the fully periodic case. To understand why this is happening we must consider the density profiles across the domain. Figures 5.8a) and b) show the average density profiles upstream and downstream of the CNT, respectively.

When no external force is applied, molecules are constantly being deleted at the outlet boundary. The upstream boundary conditions cannot accommodate this rate of loss, which causes the fluid density throughout the simulation to decrease. With this decrease comes a higher fluid velocity, as shown in Fig. 5.7. Including an external force at the boundary stems the flow of molecules out of the domain and produces more promising results.

The effect of including external forces on the drag experienced by the CNT is shown in Table 5.2. When $\alpha = 1$, the drag force is within 6% of the value measured in the fully periodic case. By adjusting α we can reduce this error to less than 1%. Drag measurement without an external force is inaccurate and not recommended. Adjusting α to the correct value is straightforward when the fully periodic MD simulation results are available, but choosing appropriate values when they are not is difficult and more research into making this choice is required. The inclusion of adjustable parameters in boundary models is a common problem, as previously discussed. Regardless of this, choosing a default value of $\alpha = 1$ reproduces the correct velocity profile across the CNT and an average CNT drag force with reasonable error values.

The total simulation time for the fully periodic case was 6 days, and 2 days

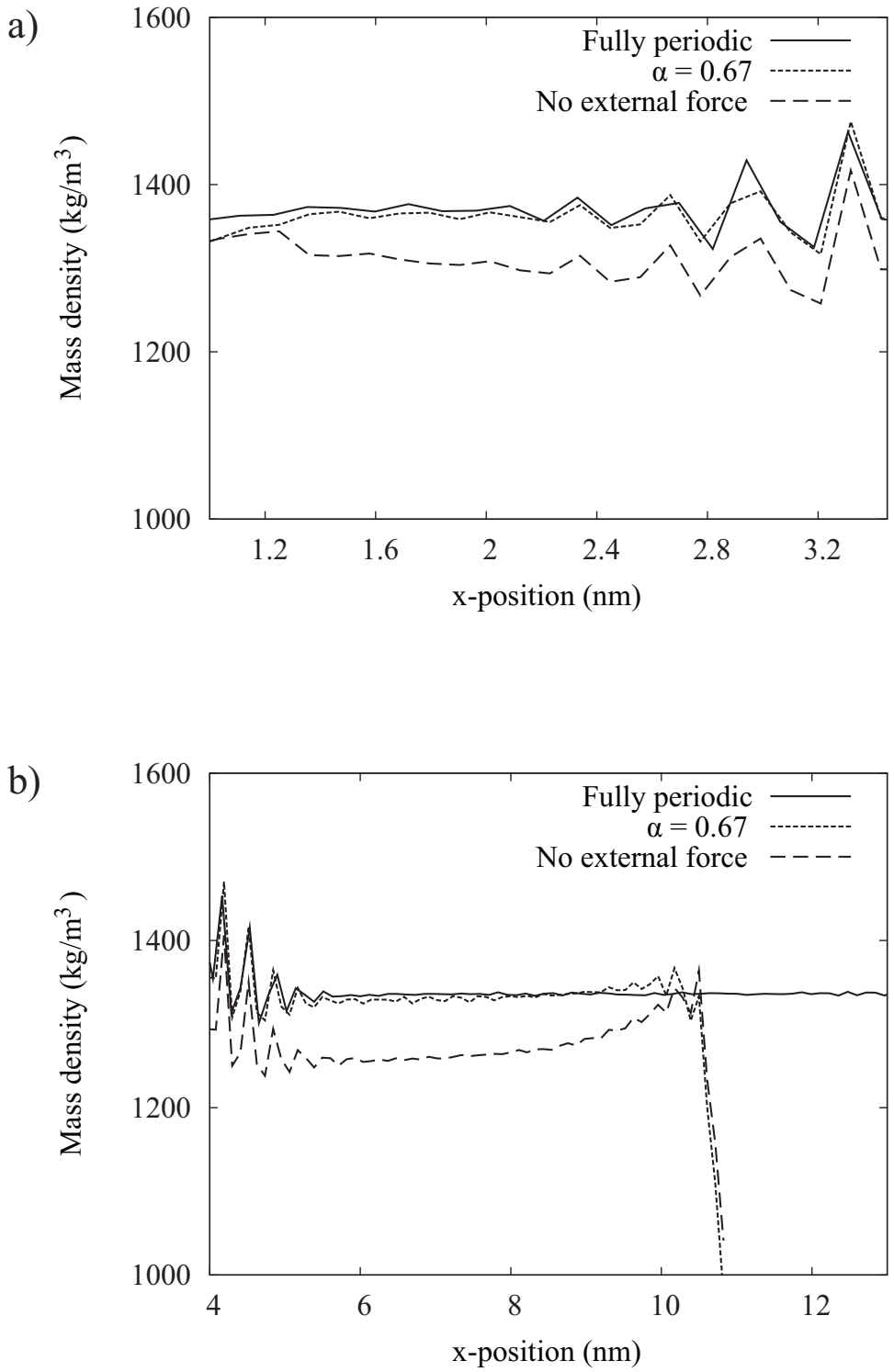

Figure 5.8: a) Upstream mass density profile b) downstream mass density profile.

for the partially periodic cases, both using 8 processors. This corresponds to a simulation speed up of approximately 3 times.

5.3 Liquid argon flow through a CNT membrane

We now consider pressure-driven flow of liquid argon through a CNT that is embedded in a solid substrate. The main purposes of this work is: to test novel boundary conditions introduced in Chapter 4; to investigate the behaviour of a simple fluid under extreme confinement; and to provide further insight into the fluid transport properties of CNTs.

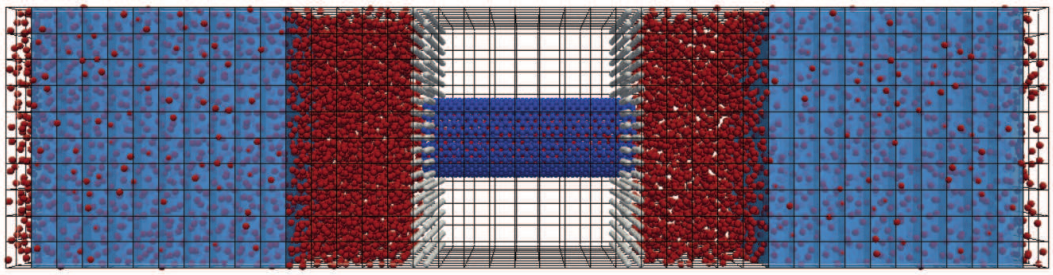

Figure 5.9: CNT membrane simulation domain.

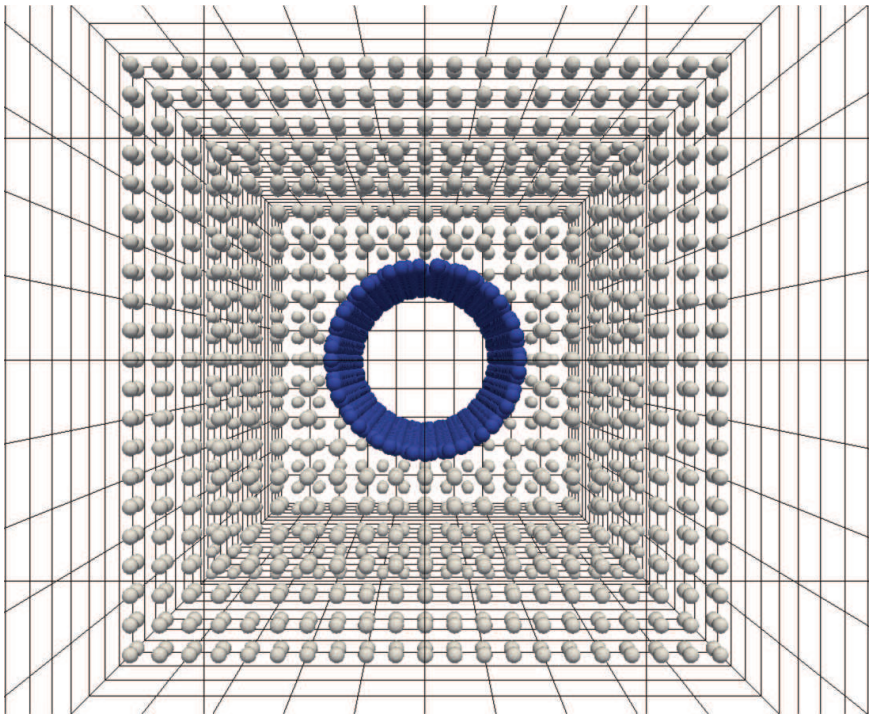

Figure 5.10: End-on view of a CNT embedded within a membrane made up of argon atoms.

To do this, we place two fluid reservoirs either side of a CNT membrane. A pressure difference is created by controlling the density of the fluid in each reservoir. This generates a concentration gradient, as previously described in Section 4.2.2. The simulation domain is shown in Fig. 5.9.

	ρ_1 kg/m^3	ρ_2 kg/m^3	ΔP (MPa)
Case 1	1300	965	49.3
Case 2	1300	1063	44.3
Case 3	1300	1189	28.2

Table 5.3: Simulation details for each case.

A $(16, 16)$ CNT with a diameter of 2.2 nm and length of 6 nm is used. The two membrane surfaces that surround the inlet and outlet of the CNT are constructed of fluid molecules frozen to their original positions, see Fig. 5.10. The density of this solid substrate is 1500 kg/m^3. The type and length of CNT are chosen to match a previous simulation performed by Huang *et al.* [165], who compared an MD simulation of pressure-driven flow through a nanopore with a full NS solution. Berendsen thermostats are applied to each reservoir to maintain a constant temperature of 133 K. The insertion and deletion of molecules was performed far away from the CNT membrane so as not to disturb important entrance effects that play a vital role in fluid transport through nanoscale membranes [149]. A time step of 1×10^{-15} s was chosen to ensure that no molecules would overlap after any time step. The dimensions of the reservoirs are $11{\times}7{\times}7$ nm^3, chosen so that the inlet/outlet boundaries are 5 CNT diameters from the inlet/outlet of the membrane: this ratio was shown by Mansouri *et al.* [166] not to influence fluid transport in a microchannel. The interaction parameters are the same as the previous external flow study, i.e. a strong interaction between the argon and carbon atoms, shown in Table 5.1.

Three density (pressure) differences are considered in this initial study, shown in Table 5.3. In each case the upstream density is controlled to be 1300 kg/m^3

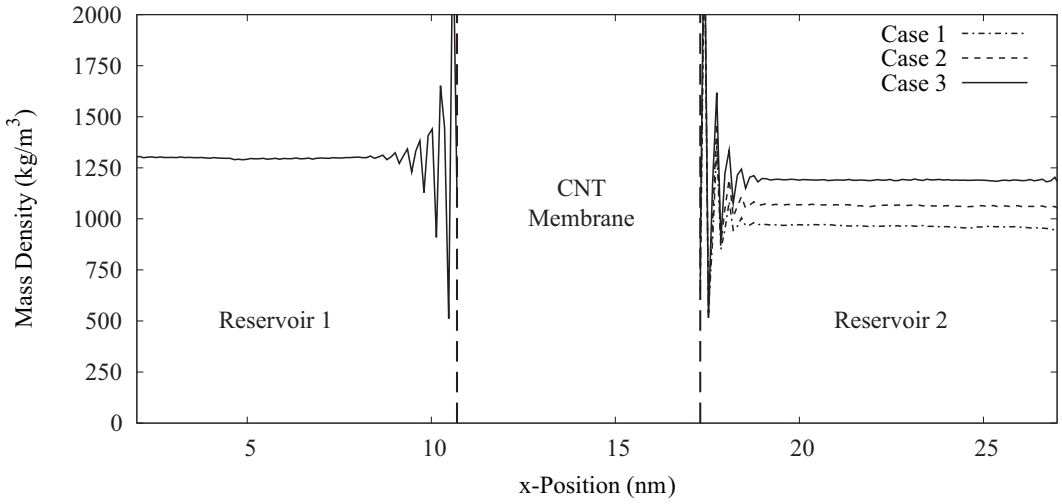

Figure 5.11: Density profile across the domain.

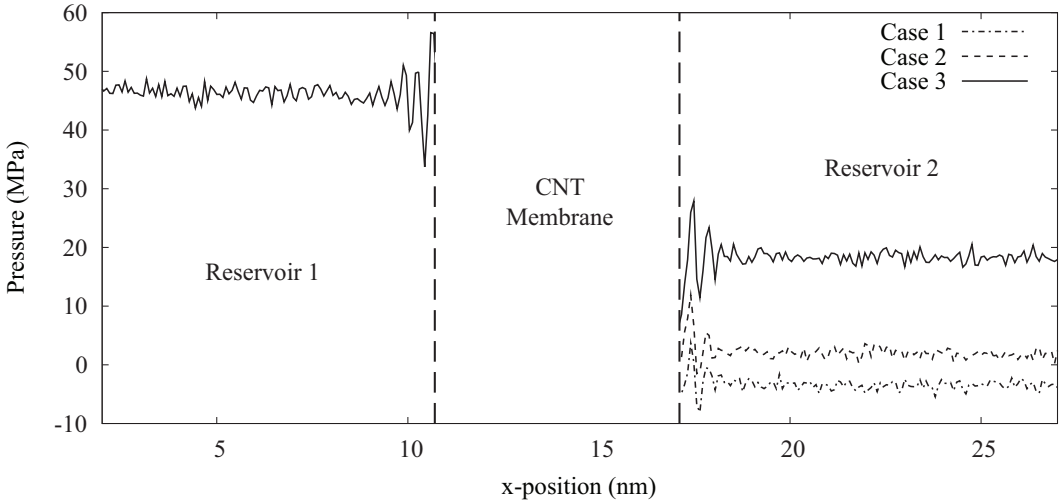

Figure 5.12: Pressure profile across the domain.

and the downstream density is controlled to – in turn: 965, 1063 and 1189 kg/m^3. These values of density are the same as those used in [165]. The density changes lead to pressure differences of 49.3, 44.3 and 28.2 MPa, respectively, which were measured during our MD simulations. However, Huang *et al.* report pressure differences (for the same density changes) of 70, 60 and 40 MPa, respectively. After referring to thermophysical properties provided by the National Institute of Standards and Technology (NIST) [164], it is clear that Huang *et al.* have not included a correction term in their pressure measurements, as discussed in

Section 4.1.4. For example, liquid argon at 1309 kg/m^3 and 133 K should have a pressure of ∼51 MPa, according to NIST [164]. Huang *et al.* [165] report a measured pressure of 80 MPa. Using Eq. 4.13, the pressure correction at this state point is -27.3 MPa which would give a corrected pressure of 52.7 MPa, which is in reasonable agreement with the experimental value. If the same procedure is applied in the downstream reservoir for each case, then the corrected pressure differences may be obtained. We chose to match fluid densities, which have no such associated errors, to allow a fair comparison of results.

The density and resulting pressure profiles across the domain are shown in Figs. 5.11 and 5.12, respectively. The target densities in the reservoirs have been reached and the controllers are operating correctly. The average number of argon molecules in the highest density case was ∼18 000.

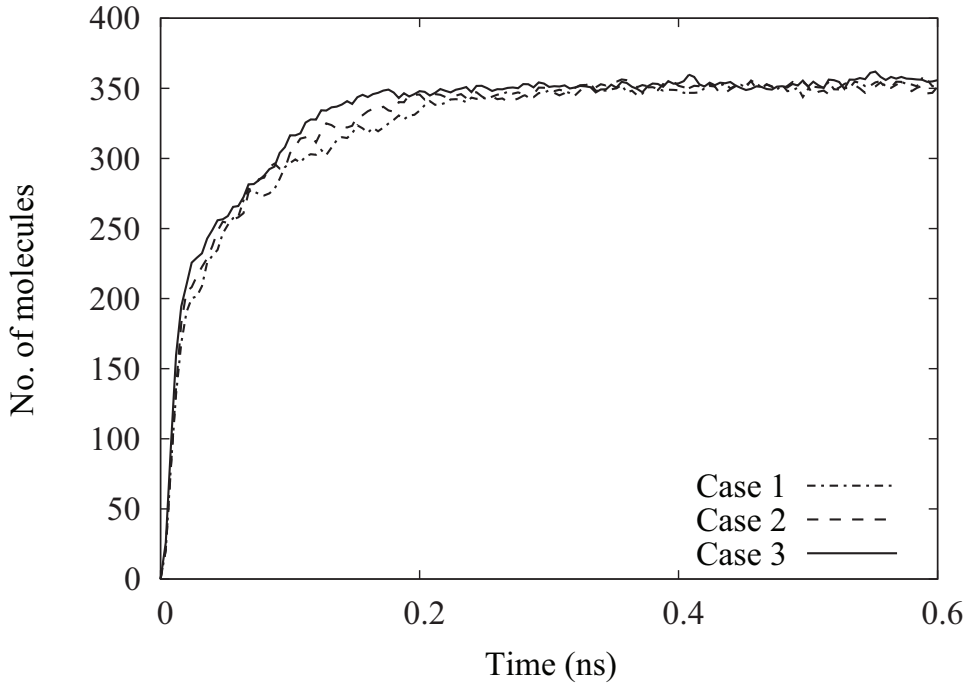

Figure 5.13: Number of fluid molecules inside the CNT during the initial filling process.

The simulation procedure for each case was as follows:

1. create the mesh and fill it with molecules;

2. equilibrate each reservoir to the correct conditions while the CNT is closed,

(Figs. 5.11 and 5.12);

3. open the CNT and allow the fluid to fill the nanotube (Fig. 5.13), and allow steady state conditions to be reached;

4. average the fluid properties over a specified time period.

Step 3 took approximately 0.5 ns to complete: steady state conditions were established when a constant average streaming velocity inside the CNT was obtained. The total number of molecules inside the CNT over the initial filling period is shown for each case in Fig. 5.13. Step 4 is performed over 2 million time steps which is equivalent to 2 ns, and took 4 days to solve on 8 processors.

5.3.1 Results

We compare velocity profiles, measured using a radial binning technique, with those of Huang *et al.* [165] for a nanotube of similar diameter and length. These authors used a neutral potential model between the liquid and the nanotube, with interaction parameters the same for liquid-solid and liquid-liquid. The velocity profiles for each case are shown in Fig. 5.14.

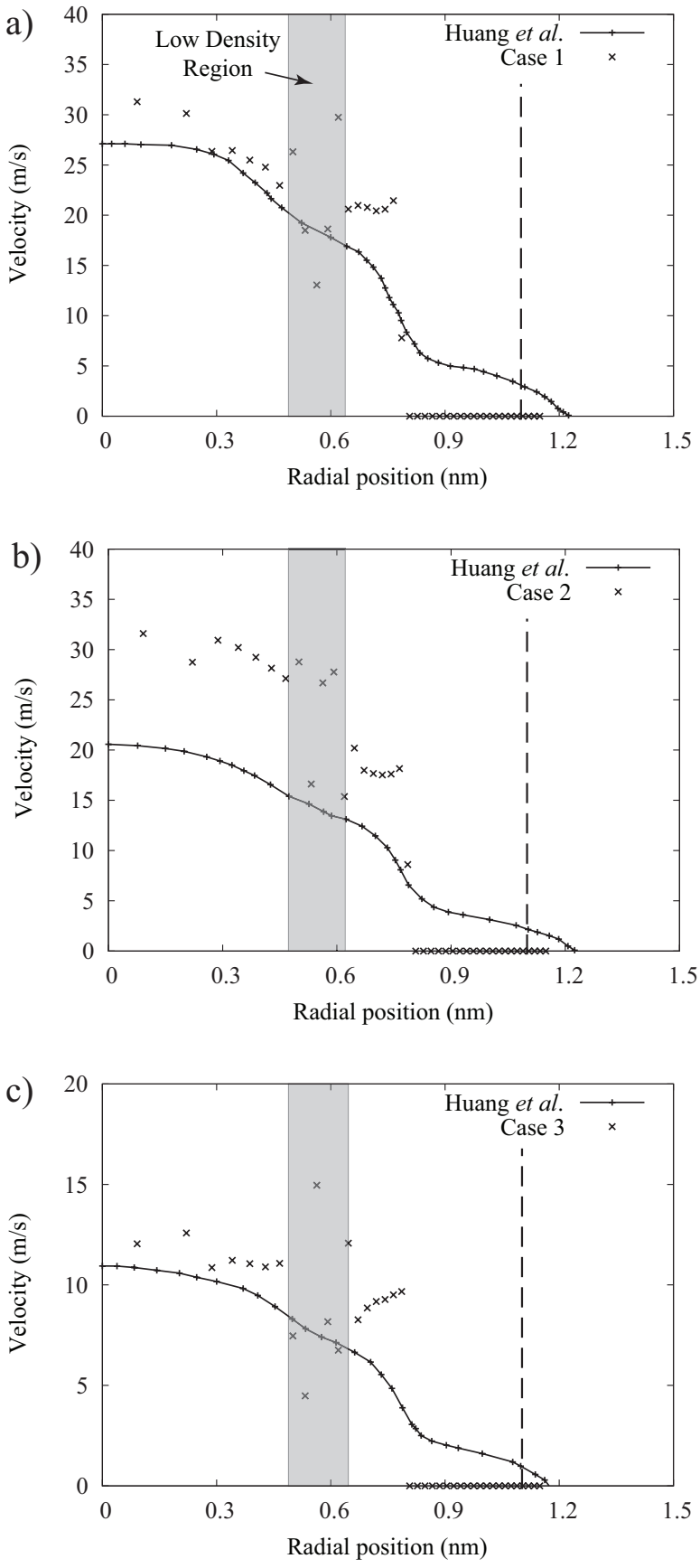

Figure 5.14: Comparison of MD results of radial velocity profile for a) case 1 b) case 2 and c) case 3. The vertical dashed line indicates the location of the CNT carbon atom centres. The gray area indicates the regions of low fluid density inside the CNTs.

The velocity profiles from our simulations lie slightly higher than those reported in [165] for all three cases. The reason for this is that while both simulations include an attractive potential between liquid and solid, the nanopore contained many more molecules in its walls than our CNT. This difference causes a reduction in the fluid velocity due to the increase in the number of attractive interactions. Huang *et al.* also report a fluid velocity beyond the nanopore wall, suggesting an error as the fluid should be unable to pass through the physical boundary. Our results show that the fluid velocity beyond a radius of ∼0.8 nm is zero, because there are no fluid molecules in this region. The physical size of the carbon atoms in the CNT prevents any argon atoms from passing beyond this radius. No such effect is shown by Huang *et al.* The statistical noise in the velocity profile at ∼0.6 nm is caused by the fluid structure within the CNT, which is described in detail shortly. The area of low fluid density inside the CNT, highlighted by the shaded area in Fig. 5.14, creates uncertainty in the velocity measurement due to the sampling technique used, discussed in Chapter 4. In reality, the velocity in that region would be zero since there are so few molecules which occupy that space inside the CNT.

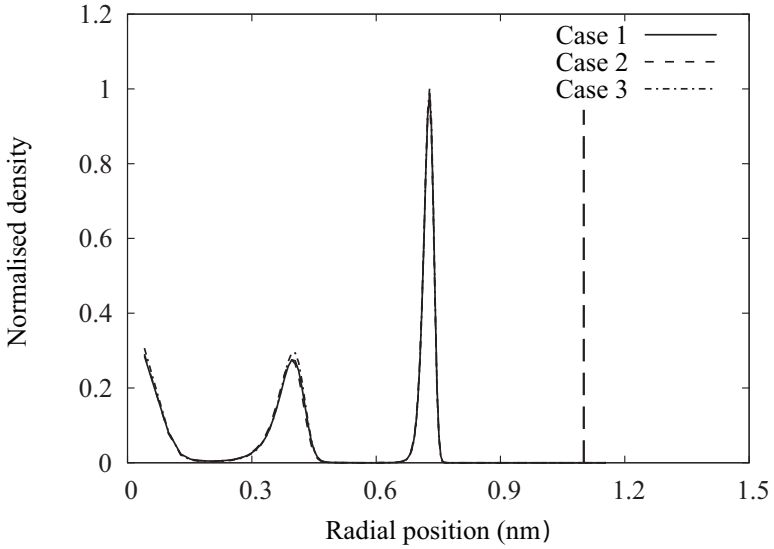

Figure 5.15: Radial argon density profile. The vertical dashed line indicates the location of the CNT carbon atom centres.

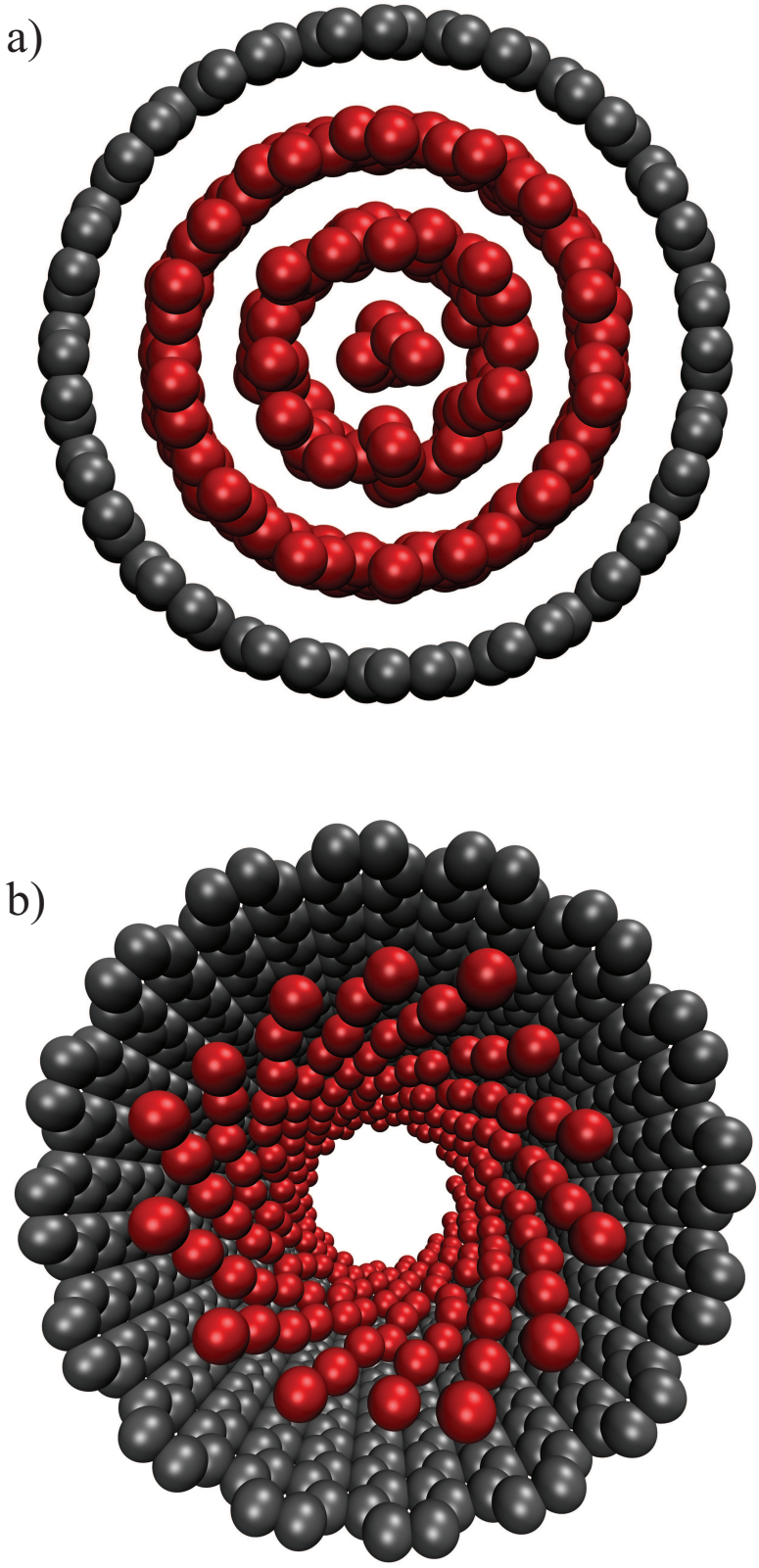

Figure 5.16: a) Fluid layering inside CNT and b) Outer layer of liquid argon demonstrating the spiral internal structure.

Figure 5.15 shows that the liquid argon forms a well-ordered structure within the CNT. Three layers are present, with the one closest to the CNT surface having the highest density; this is because of the strong interaction between the fluid and the solid. The radial density profile is the same in each case and is independent of the applied pressure difference. In Fig. 5.13 we showed that each CNT contains the same number of molecules, therefore the overall density is also constant. We can visualise the fluid structure further by taking a snapshot during the simulation, as shown in Fig. 5.16. The fluid in the outer layer (closest to the wall) demonstrates a very high level of ordering – forming a spiral structure, similar to that of a gun barrel, see Fig. 5.16 b). Huang *et al.* reported an oscillatory density profile inside their nanopore but the fluid structure was more disordered, resulting in flatter density peaks. They also reported a non-zero density beyond the solid boundary, which again suggests the presence of errors in their results.

The velocity profiles from MD are compared to a NS solution, obtained by Huang *et al.* [165], for the same flow problem and also compared with a simple analytical hydrodynamic model, all of which are shown in Fig. 5.17. Analytical radial velocity profiles are calculated using the following:

$$u(r) = \frac{R^2}{4\mu}\left[1 - \frac{r^2}{R^2} + \frac{2L_s}{R}\right]\frac{\Delta P}{L}, \tag{5.1}$$

where R is the CNT radius, μ is the liquid viscosity, L is the CNT length, ΔP is the pressure difference and L_s is the slip length. Assumptions must be made about the nanotube radius and liquid viscosity, which are both difficult to accurately define when considering fluids contained within the smallest diameter CNTs. By setting L_s to zero we have the no-slip solution. The analytical solutions are evaluated by assuming bulk viscosity values at the average pressure inside each CNT, and using as the radius the distance from the CNT axis to the carbon atom centres. The incompressible NS solution is based upon the no-slip assumption and further details can be found in [165].

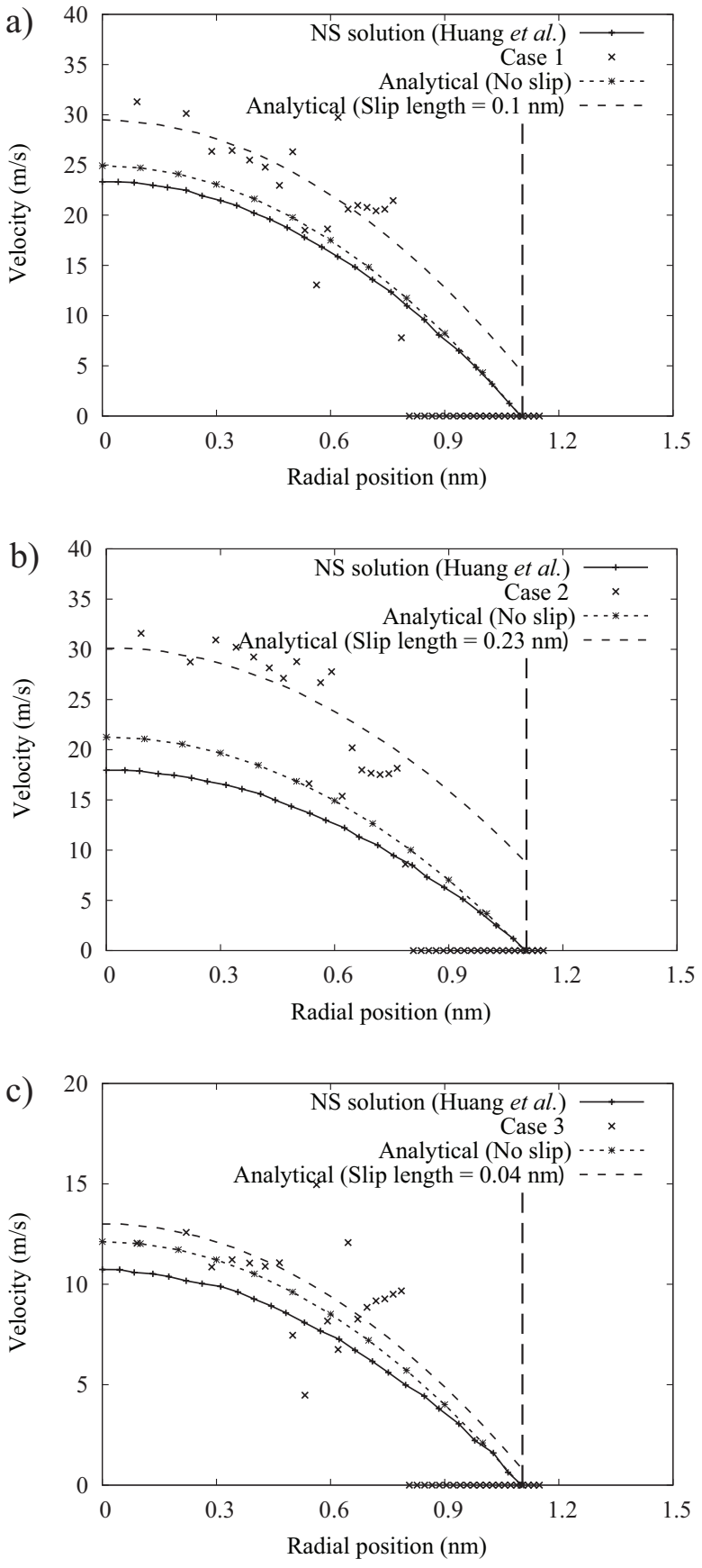

Figure 5.17: Comparison of MD results, NS solutions and analytical hydrodynamic predictions of the radial velocity profile for a) case 1, b) case 2, and c) case 3. The vertical dashed line indicates the location of the CNT carbon atom centres.

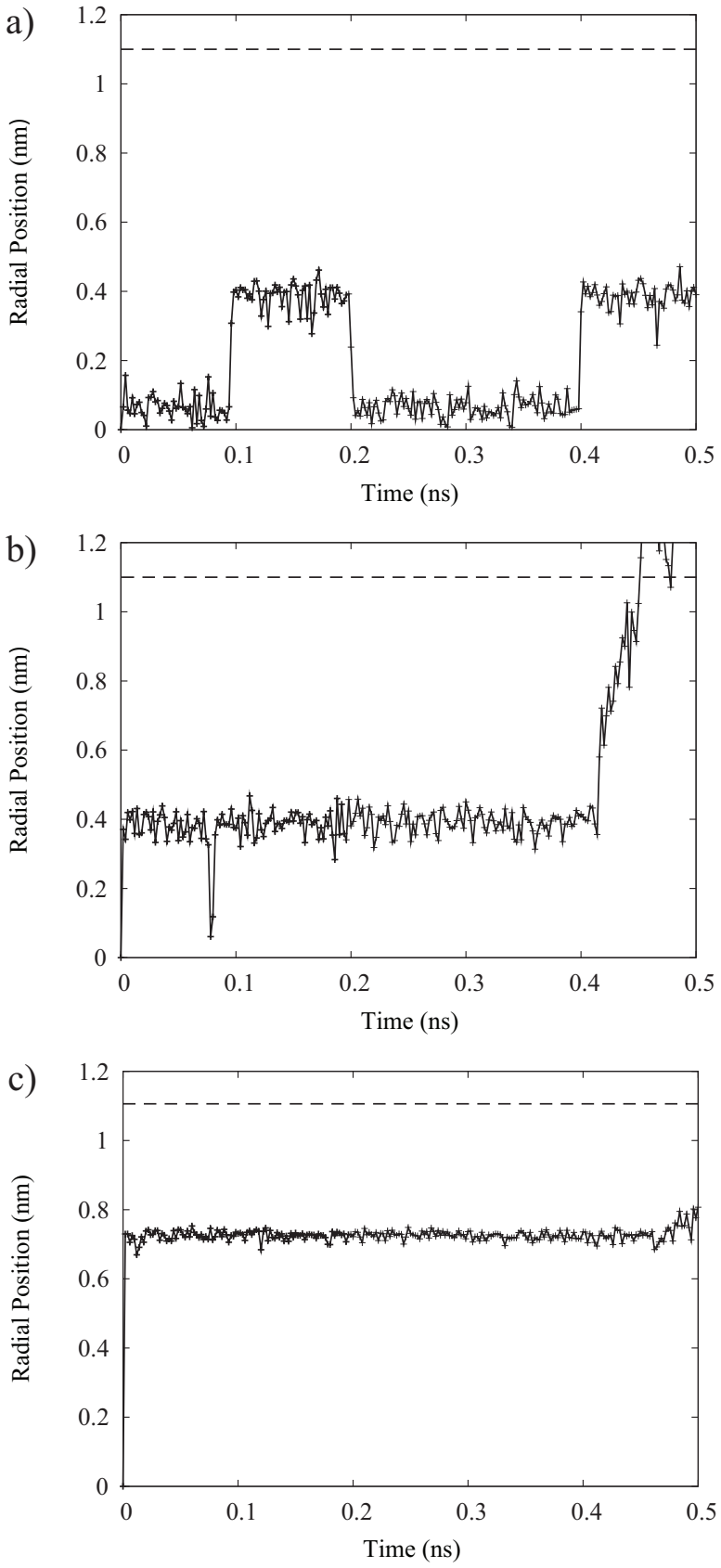

Figure 5.18: Radial tracking of argon molecules originally located in a) the innermost shell, b) the middle shell, and c) the outermost shell. The horizontal dashed line indicates the position of the CNT wall.

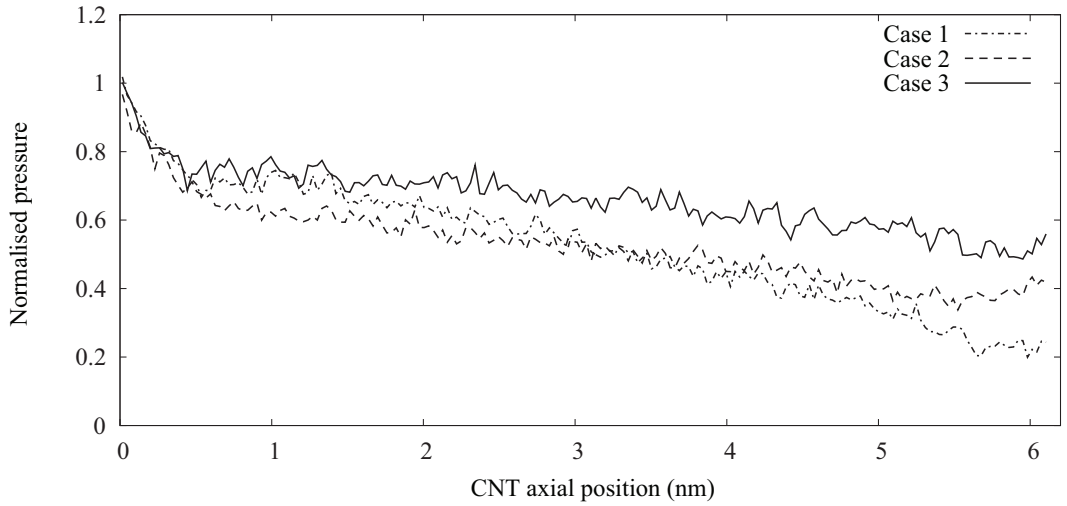

Figure 5.19: Normalised pressure profiles inside the CNT.

We can fit Eq. 5.1 to our MD results by using L_s as a fitting parameter, as shown in Fig. 5.17. The inclusion of the slip term improves the profile prediction slightly, but significant errors are still present. Based on the assumptions made, and the poor fit of data, Eq. 5.1 – with or without slip, is not a reliable analytical tool for this particular flow problem and we must turn to atomistic techniques such as MD for accurate results under such extreme conditions.

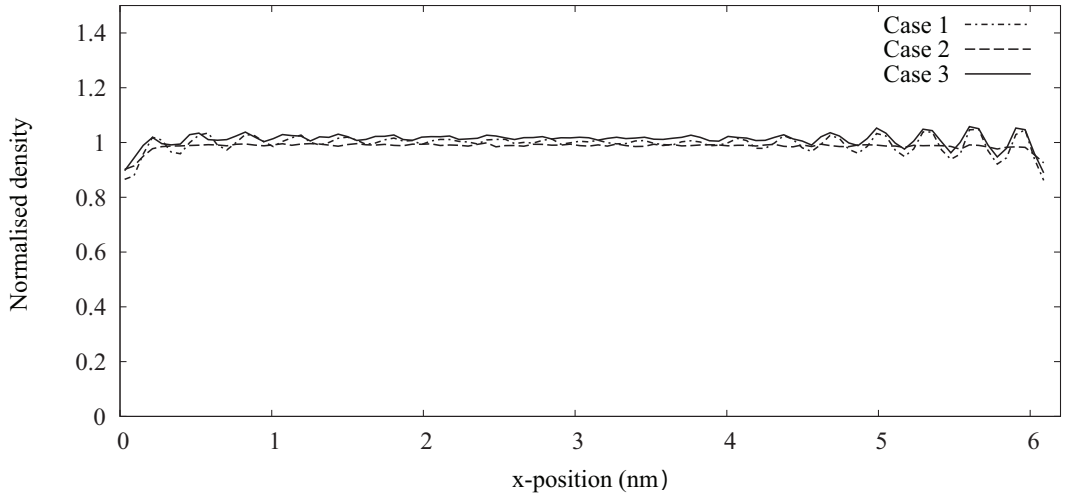

Figure 5.20: Normalised density profiles inside CNT.

By tracking the trajectory of individual molecules in each fluid layer we can gain insight into the associated molecular transport mechanisms. Figure 5.18

shows the radial positions of 3 molecules over a 0.5 ns time period as they travel along the CNT. Molecules which are originally located in the innermost and middle "shells" are free to move from one to another but molecules in the outer shell do not appear to have the freedom to leave the layer. This non-continuum behaviour is one of the main reasons why hydrodynamic relations cannot be used to predict fluid behaviour at the nanoscale; the assumption that the fluid is continuous and fills the entire space inside the nanotube is not valid. The tracking of many more molecules inside the CNT is required to confirm this theory, and will be the subject of future work.

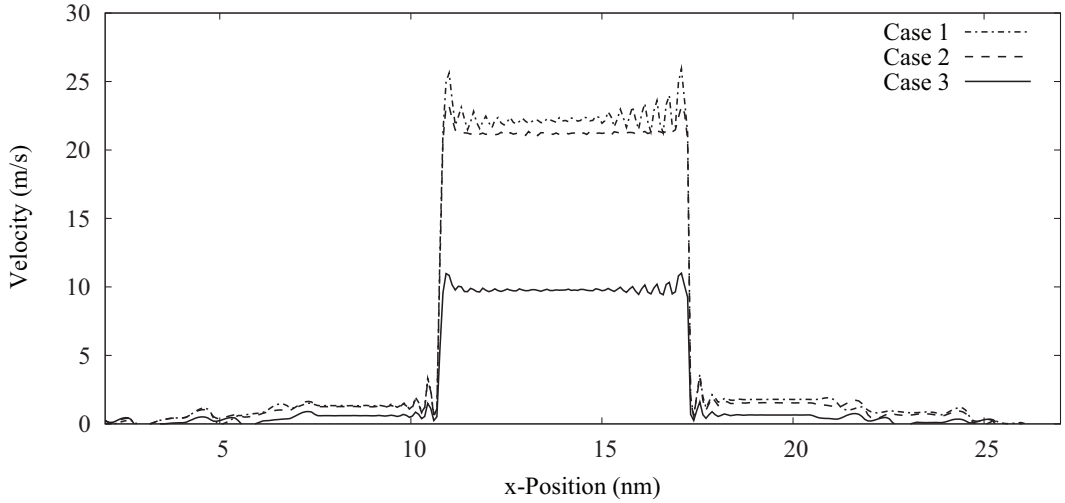

Figure 5.21: Axial velocity profiles along the domain.

Figure 5.19 shows the internal pressure profiles of liquid argon inside the CNT. The inlet pressure is the same in each case as the upstream conditions are identical. The fluid density and streaming velocity fluctuate about constant values along the CNT axis in each case, as shown in Figs. 5.20 and 6.12, respectively. Oscillations present in these profiles, located at the CNT inlet/outlet, are most likely caused by the fluid interacting with the membrane as it passes into and out of the CNT, however it is clear that they oscillate about constant values. Velocity must be constant since the density and cross sectional area remain fixed as the fluid travels down the CNT. Therefore the different pressure drops along each CNT must be associated with frictional losses, as there are greater pressure losses

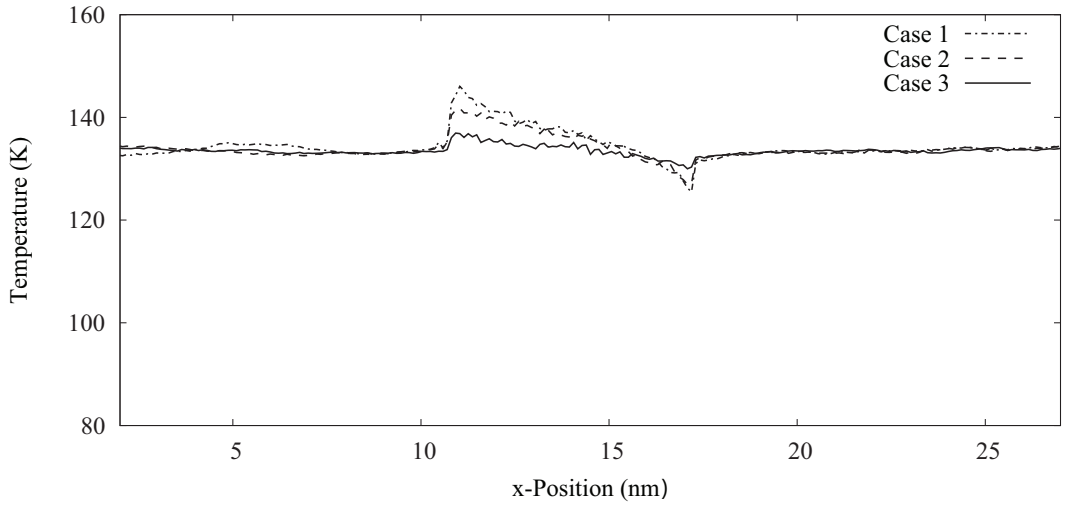

Figure 5.22: Axial temperature profiles.

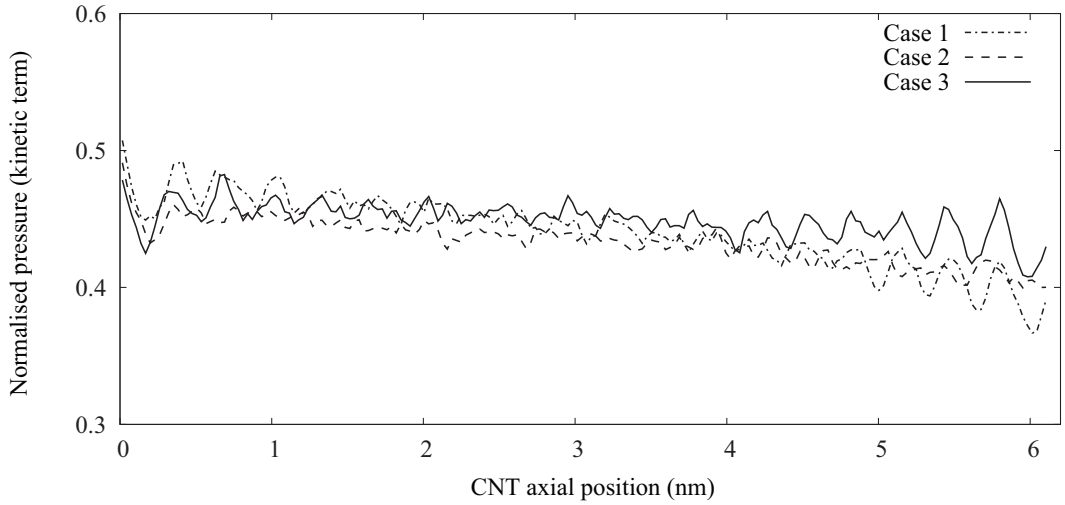

Figure 5.23: Kinetic term in the pressure measurement along the CNT axis.

when the fluid streaming velocity is higher. As with any moving fluid, friction causes energy dissipation, which in this case is associated with the intermolecular forces between the fluid and solid as the liquid argon flows through the CNT. The role that this intermolecular force plays in total frictional loss is discussed shortly.

The temperature of the argon rises as it passes into the CNT in each case, as shown in Fig. 5.22. This temperature rise is caused by the sudden acceleration of the fluid (see Fig. 6.12), which causes viscous heating (molecules having

greater kinetic energy) which dissipates along the CNT because no similar effect is present downstream. This temperature rise has been observed experimentally in microtubes and is referred to as viscous dissipation [167]. Although velocity remains constant along the CNT length, the temperature decreases; the streaming velocity is not included in temperature measurement, see Section 4.1.3. However, the fluid's kinetic energy decreases along the CNT, demonstrated by the decrease in the kinetic term of the total pressure in Fig. 5.23.

The kinetic term of the pressure is usually constant along the CNT, as the temperature is controlled using a thermostat in a typical MD simulation. However, the use of thermostats in such confined regions is not recommended [121]. In this case, a thermostat would directly affect the dynamics of the fluid inside the CNT – the pressure losses will be less, which would in turn change the fluid velocity. We tested this and found that thermostating the fluid inside the CNT causes the fluid velocity to rise by 5%, above the associated statistical error of less than 2%.

5.3.2 Effect of changing CNT-liquid interaction

To investigate the effect of choosing different interaction strengths between argon and carbon, we repeat the simulations and make the CNT more hydrophobic, i.e., decrease the interaction strength between the fluid and solid. $\epsilon_{\text{Ar-C}}$ is reduced to 0.79834×10^{-21} J [161], all other interaction parameters remain unchanged.

The radial velocity profiles for these cases are shown in Fig. 5.24. The most noticeable difference between these profiles and those of the hydrophilic case, see Fig. 5.14, is the radial velocity profile becomes more like a plug flow and less parabolic in shape. This phenomenon has been shown previously by Nagayama and Cheng [154] who used MD to simulate pressure driven argon flow through a 5.4 nm wide nanochannel. These results support the theory that hydrophobic surfaces provide less resistance to fluid flow: streaming velocities and mass flow rates are much higher than those reported for a hydrophilic CNT, as shown in

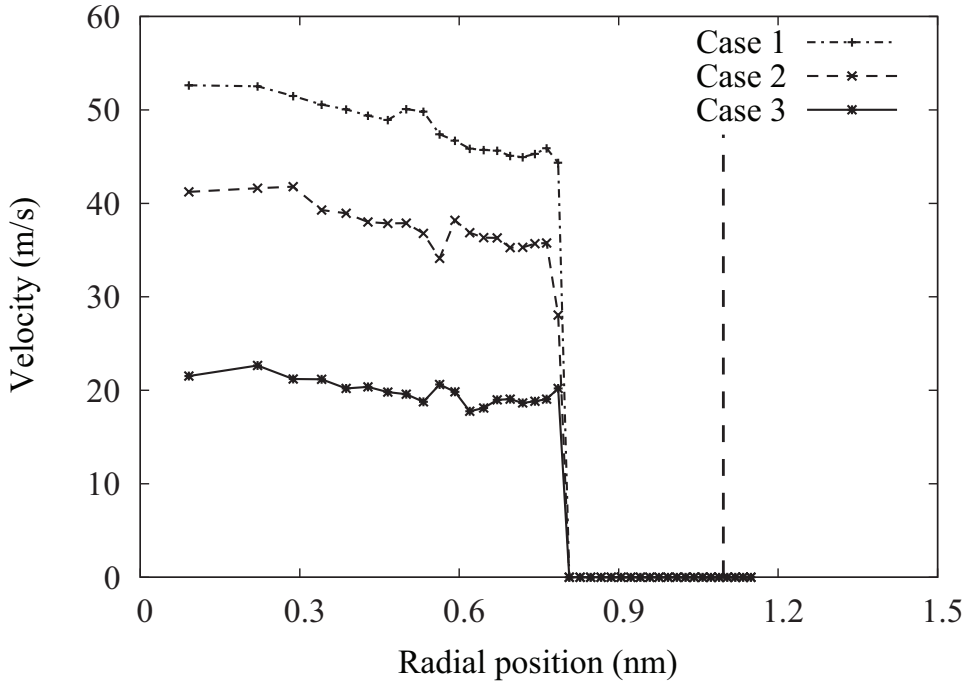

Figure 5.24: Velocity profiles for three cases where the interaction strength between the CNT and fluid has been reduced. The vertical dashed line indicates the location of the CNT carbon atom centres.

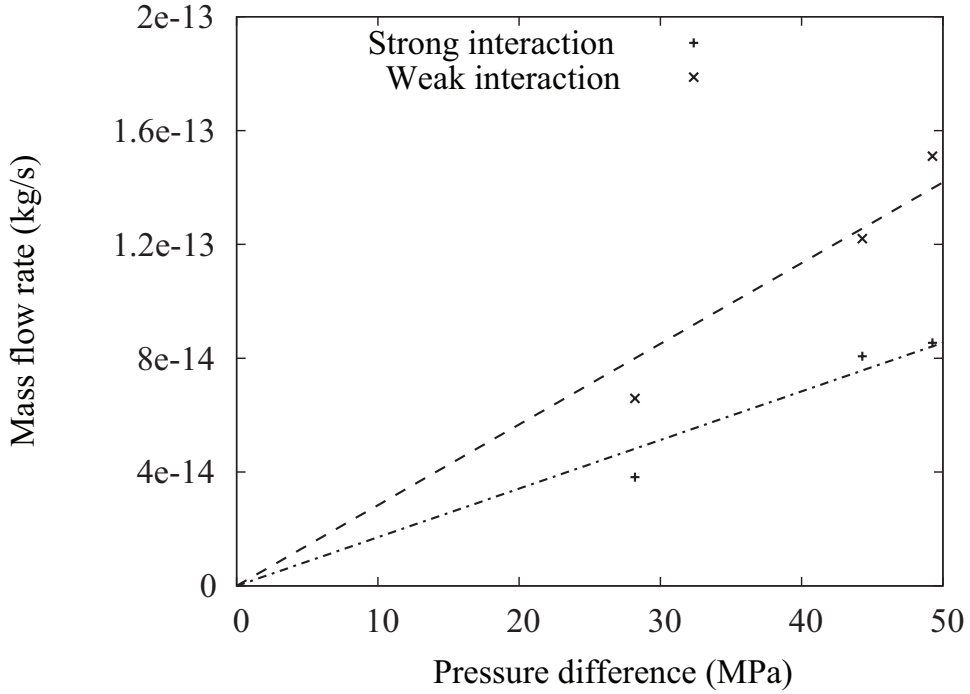

Figure 5.25: Comparison of mass flow rate against pressure difference for different interaction strengths. The dashed lines show the best linear fit for each case.

Fig. 5.25. Hydrodynamic predictions would have higher associated errors in these cases.

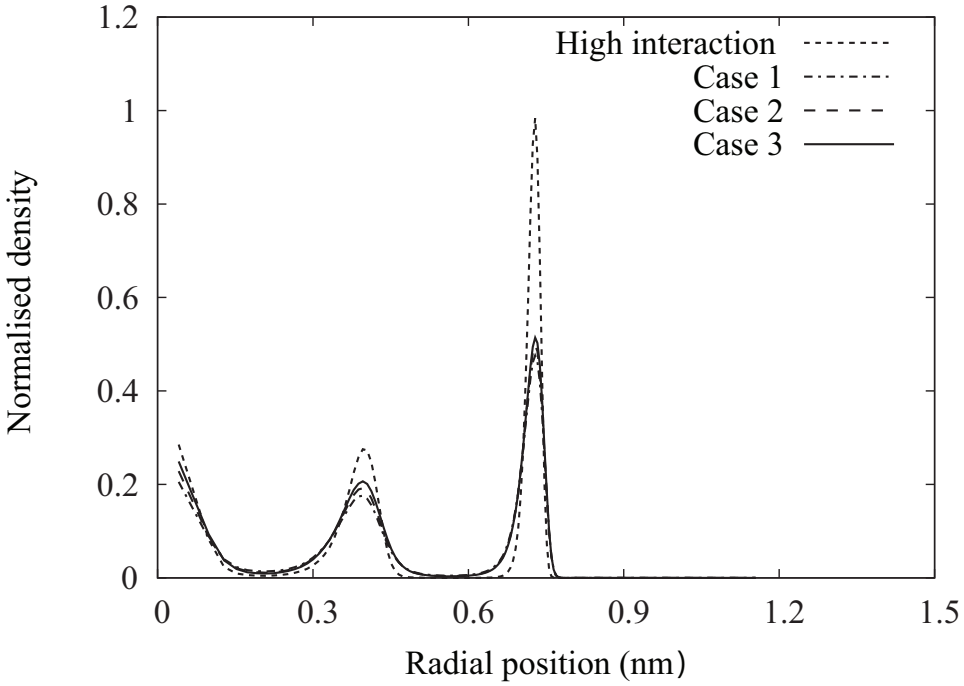

Figure 5.26: Radial density profiles within the CNT.

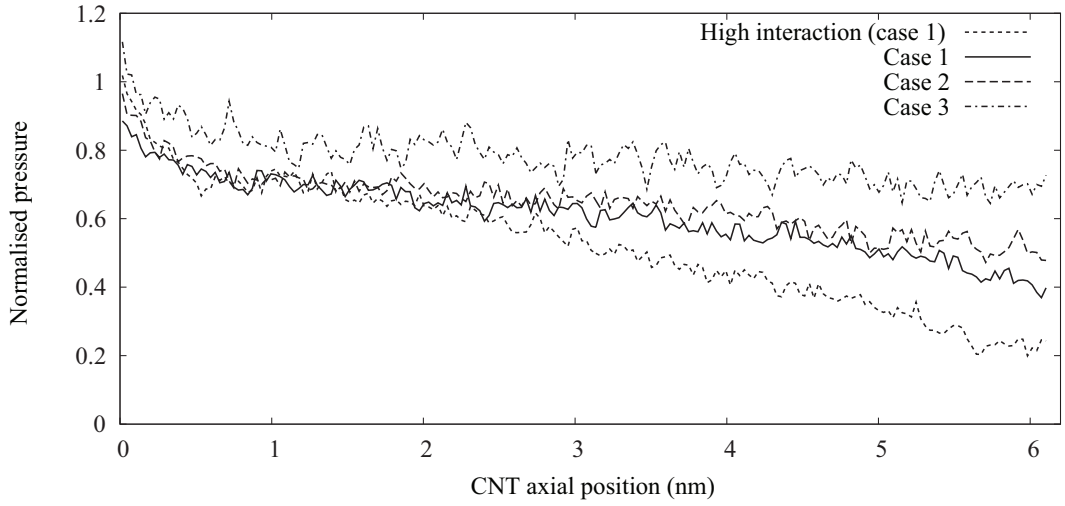

Figure 5.27: Pressure profiles along the CNT with varying interaction strength.

In a previously reported simulation [154], a change in the distance between the liquid and solid boundary was observed when a more hydrophobic interaction was applied. Figure 5.26 shows that we do not see the same effect occurring in

our simulations. One explanation for this may be that the fluid in the CNT is highly confined and mobility is reduced, whereas in the previous study the fluid was contained within walls which were further apart. Reducing the interaction strength has caused the density in the outermost layer to decrease significantly. Although the overall fluid density inside the hydrophobic CNT has been reduced, the fluid velocity is much higher, which in turn has led to an increase in the mass flow rate, as shown in Fig. 5.25.

Figure 5.27 shows the axial pressure profiles along the CNT for the hydrophobic and hydrophilic simulations. Pressure losses are less for a hydrophobic CNT than a hydrophilic one, which has not been shown previously. However, pressure losses are dependent upon the fluid flow rate, as in the hydrophilic cases. These results are in agreement with experimental findings that showed that friction increases with a more hydrophilic interaction between liquid and solids [168].

5.4 Summary

In this chapter we have used recently developed controllers [1] to apply continuum fluid boundary conditions in MD to simulate liquid argon in cross-flow past a CNT, and through a CNT membrane. Advantages of our simulation method are that: it can apply user-specified fluid properties directly, rather than indirectly through other means; it is not dependent upon fully periodic systems; it can accurately generate fluid transport without any geometrical constraints; and it is capable of performing as an essential part of a hybrid continuum-atomistic technique.

We considered the external cross-flow of liquid argon past a CNT, initially in a fully periodic domain, followed by the same CNT in a partially periodic domain. By replacing the periodic boundary conditions in the streamwise direction, we were able to shrink the length of the domain considerably, thus increasing the simulation's computational efficiency. The partially periodic case was $\sim$3 times

faster than the fully periodic simulation. By using a combination of a mass flow inlet and an external boundary force at the outlet, we were able to accurately reproduce the results from the fully periodic case.

The liquid flow of argon through a CNT membrane was investigated using a novel simulation model. Two fluid reservoirs located at either end of the membrane were controlled to be at different densities and were not connected through periodic boundary conditions. This generated the fluid driving force. We used three density (pressure) differences and compared the results with simple analytical hydrodynamic predictions, NS solutions and an independent MD simulation of argon flow through a hydrophilic nanopore.

Hydrodynamic solutions are based upon assumptions of the fluid properties inside a CNT, which are not straightforward to define. The analytical velocity profiles, and those from NS solutions were unable to reproduce the results obtained from our MD simulation. This is because the fluid inside a CNT forms a well-ordered structure and displays different transport mechanisms from bulk flows. We can no longer rely on continuum-based solutions to accurately predict fluid behaviour under extreme confinement, e.g., inside the smallest diameter CNTs.

The effect of changing the interaction strength between the liquid and solid was also examined using MD. We found that as the CNT becomes more hydrophobic, the flow rate of the contained fluid increases under the same pressure difference. The flow through the hydrophilic nanopore (not a CNT) produced the slowest fluid flow rate, while a CNT with a weak solid-liquid interaction led to the highest flow rate. These results support the claim that surface friction decreases when the solid-liquid interaction becomes more hydrophobic.

Chapter 6

Water Transport Through CNTs using OpenFOAM

In this chapter we present results from MD simulations of pressure-driven flow through (7,7) CNTs with and without defects. Cases with no defects are performed to investigate the effect that changing CNT length has on the internal flow dynamics of water. We then include vacancy sites defects (missing carbon atoms) in the CNT structure and discuss how their inclusion alters water transport through the nanotube.

6.1 Water transport through (7,7) CNTs of different lengths

Another important physical characteristic of CNTs is their length. CNT membranes as thin as 2-5 μm can be manufactured [55, 58] but MD simulations are typically performed using CNTs which are only a few nanometers in length. Previous simulations investigating the effect of CNT length were performed using short CNTs where differences in length were only a few nanometers [95, 102, 169]. These reported no significant change in water flow rate. Peng *et al.* [170] demonstrated by experiment that the flow of water through a protein membrane showed

a non-linear dependence on membrane thickness (i.e. nanotube length). Mattia and Gogotsi [3] suggest that the length of the carbon nanotube is the primary determiner of the nature of the flow: in very short CNTs stochastic flow, due to thermal fluctuations, has been observed [132]; in infinitely long CNTs, modelled using periodic boundary conditions, single file diffusion dominates [145], as also seen experimentally. Understanding the influence of length on the flow is of central importance to understanding the nature of CNT flows in general. In the present research, MD simulations are used to investigate water transport along (7,7) CNTs with lengths ranging from 2.5 to 50 nm, in order to assess how the length affects fluid flow velocity, mass flow rate and axial fluid properties.

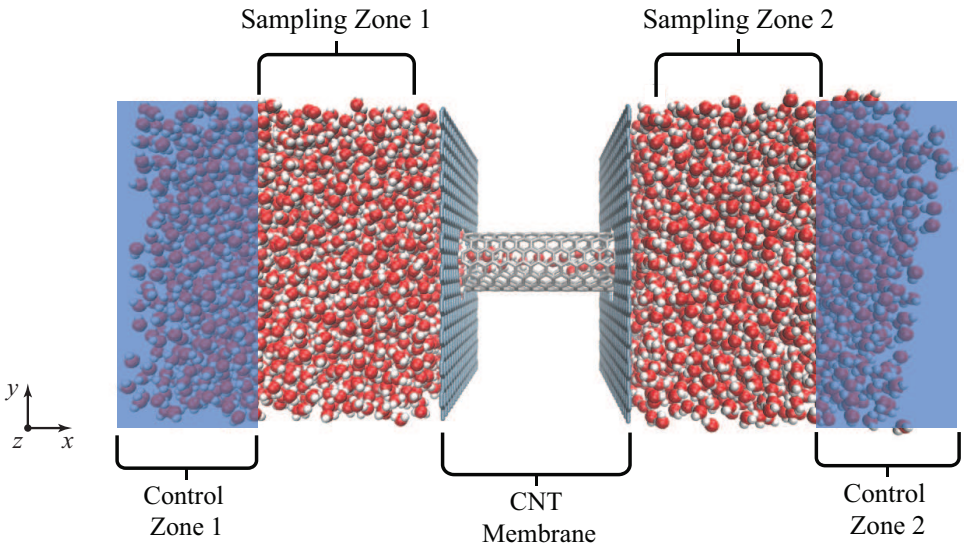

Figure 6.1: Simulation Domain.

The configuration of the pressure-driven flow simulation domain is shown in Fig. 6.1. Two graphene sheets are positioned at the inlet and outlet of the CNT to form a simplified membrane representation. The CNT and graphene sheets are modelled as rigid structures to speed up the MD runs: this has been reported to be a fair approximation in a previous study [109]. Periodic boundary conditions are employed in the y- and z-directions, while non-periodic boundary conditions are applied in the x-direction: the left-hand boundary is a specular-reflective wall, while the right-hand boundary deletes molecules upon collision. The wall helps

control the fluid pressure and density upstream while the deletion patch creates an open system [143]. The rigid TIP4P water model is used with a time-step of 1 fs in all the following simulations.

A pressure difference of 200 MPa is applied across the membrane in all simulations; such a large pressure difference is required to resolve the dynamics of the simulation over a shorter time period due to the large computational cost associated with MD. (Pressure differences of 5-7 MPa are generally used in industrial filtration processes, but the resulting flows rates are too low for MD to accurately resolve over the time accessible by MD.) Berendsen thermostats are applied to both fluid reservoirs to maintain a constant temperature of 298 K and eliminate the contribution of any temperature gradients to the fluid transport. The fluid is not controlled inside the CNT so as not to disturb the dynamics of the contained water molecules. Bernardi *et al.* [121] demonstrated that thermostatting fluid atoms contained within walls which are rigid causes changes in fluid pressure, density and streaming velocity, and so suggests caution when interpreting results from such systems. The maximum variation in water temperature inside any CNT in our simulations was found to be 3.5 K. Both fluid reservoirs have dimensions of $4.4\times4.4\times4.4$ nm^3. The number of molecules in the entire domain ranged from $\sim$7000 to $\sim$13000 for the shortest to the longest CNTs, respectively.

The upstream pressure is controlled using a proportional-integral-derivative (PID) control feedback loop algorithm in addition to adaptive control of mass-flux at the inlet. Downstream of the membrane, pressure is controlled using a pressure-flux technique [153] in order to allow the flow through the system to develop without being over-constrained. These techniques are described in detail in Section 4.2.3

Five different CNT lengths are investigated: 2.5, 5.0, 12.5, 25, and 50 nm. For every simulation, apart from the 50 nm long CNT case, the CNT is closed intially while the reservoirs are filled with water molecules and equilibrated to the correct conditions. After this initial equilibration, the CNT is opened and

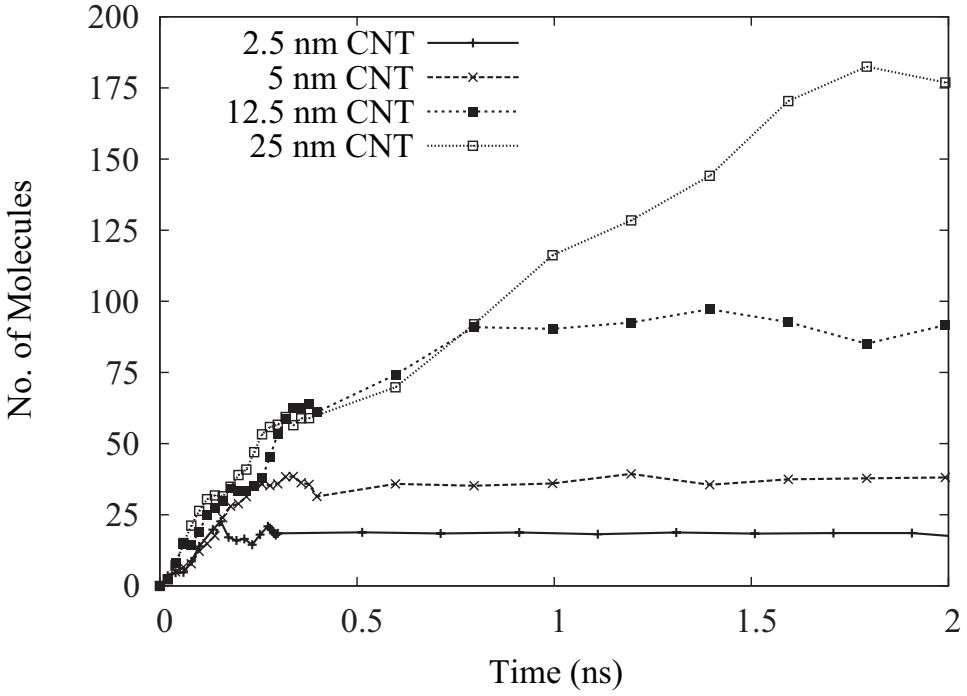

Figure 6.2: Filling dynamics of (7,7) CNTs of different lengths under 200 MPa pressure difference.

allowed to fill naturally, as shown in Fig. 6.2. Once the number of molecules in each CNT has reached a constant value the simulation is allowed to proceed until the flow rate reaches a steady state value. To avoid a long simulation of filling the 50 nm CNT, the water molecule arrangement inside the full 25 nm long CNT is "mapped" into the 50 nm case. This operation is performed twice to fill the entire 50 nm long CNT. This is a fair thing to do since the steady-state number of water molecules in each CNT shows a linear relationship with CNT length, which may be observed in Fig. 6.2. Each simulation is then advanced by a further 2 ns before averaging of properties is performed. This step also allows any unrealistic fluid structures in the 50 nm long CNT, which may exist because of the mapping stage, to dissipate. All data presented below is from a 4 ns averaging period.

The simulations were performed using 64 processors (Intel X5570 2.93 GHz CPU) and took ∼12 days to complete 4 million time steps. The 50 nm CNT simulation was performed using 80 processors to reduce the total simulation time to be the same as the smaller cases. The computational efficiency of the simula-

tions were enhanced by using a particle weighted decomposition method in OpenFOAM. The decomposition of a computational domain is typically performed using the mesh cells where each processor is given an equal number of cells, this is not recommended in this case since there is a large number of molecules in the reservoirs and this is where we want to concentrate the available computing power. The particle weighted decomposition method acts to ensure that each processor receives an equal number of molecules, this improved the processor scaling performance of our simulations which in turn led to a 20% decrease in simulation time over mesh cell decomposition method.

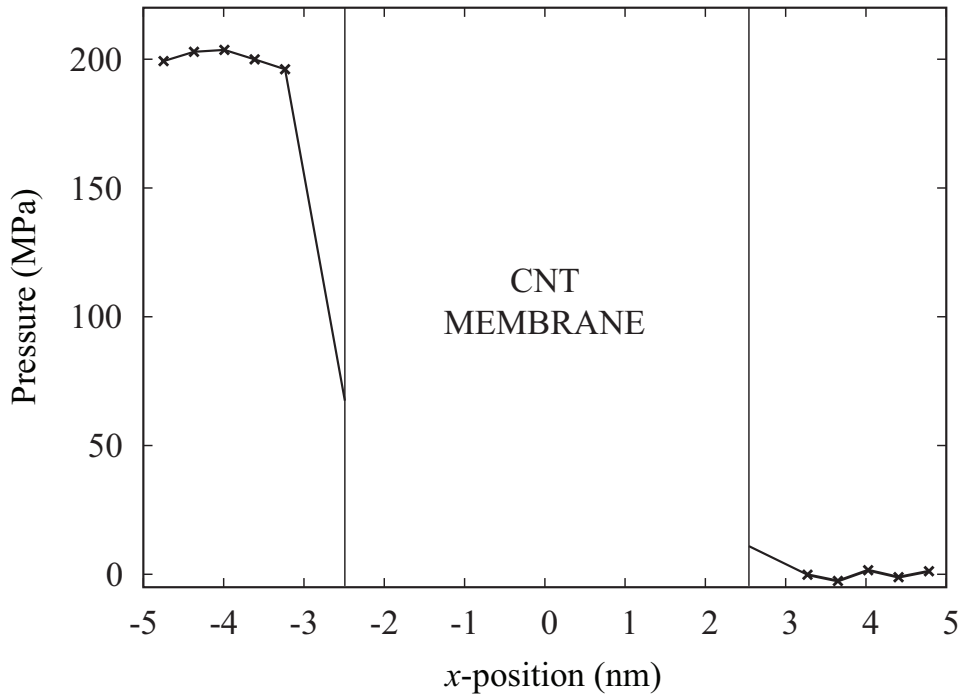

Figure 6.3: MD results of pressure profile across the domain showing the application of a 200 MPa pressure difference.

The same pressure difference of 200 MPa is imposed across all the CNT membranes, see Fig. 6.3, and the downstream reservoir is maintained at atmospheric conditions. Pressure is calculated from the stress tensor using the Irving-Kirkwood method, described in Section 4.1.4. The maximum variation in the applied pressure difference between any of the simulation runs was measured to be 0.8 MPa. The uncertainty in the pressure difference is calculated from the

variation in the mean pressure difference between the two reservoirs.

6.1.1 Flow velocity and mass flow rate results

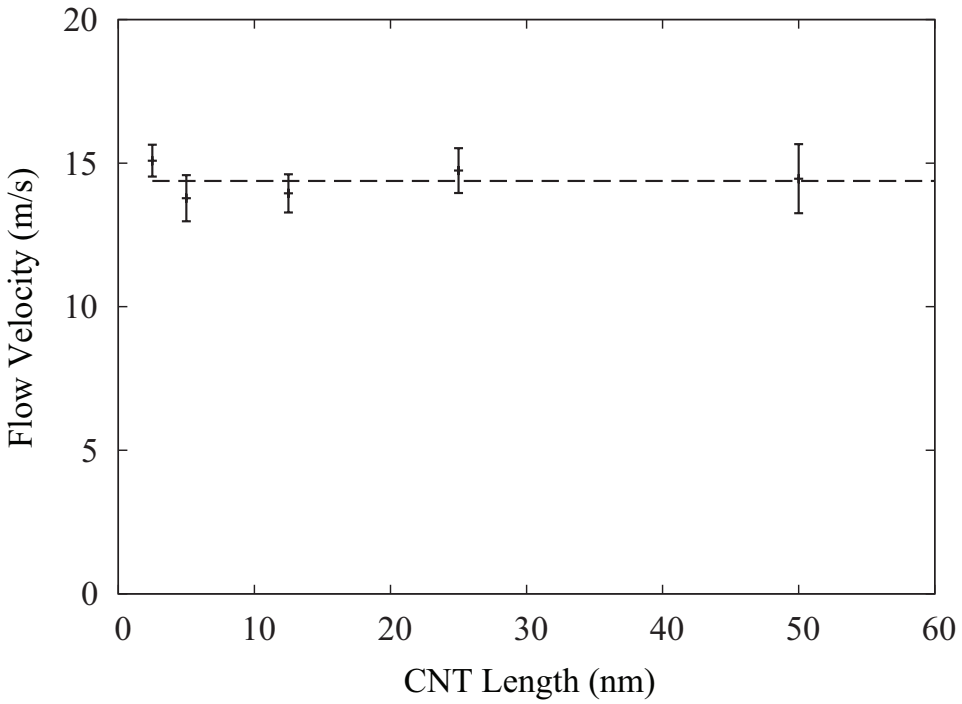

Figure 6.4: Relationship between flow velocity and CNT length under a 200 MPa pressure difference. The horizontal dashed line indicates an average fluid velocity of 14.6 m/s.

The average fluid streaming velocity for the different nanotube lengths under the same applied pressure difference are shown in Fig. 6.4. The fluid velocities are measured within the same 1 nm long region located at the midpoint of each CNT. We find that there is no significant change in the fluid streaming velocity as the CNT length increases from 2.5 nm to 50 nm. In this range of lengths, the average fluid velocity is measured to be 14.6 m/s. Previous studies have found that small changes in nanotube length (a few nanometers longer) had no effect on the fluid flow rate under the same pressure difference [95]. We can confirm that this phenomenon holds for extensions of 20 times the original length.

It has also previously been shown that there is a linear relationship between the applied pressure difference and the resulting fluid mass flow rate and fluid

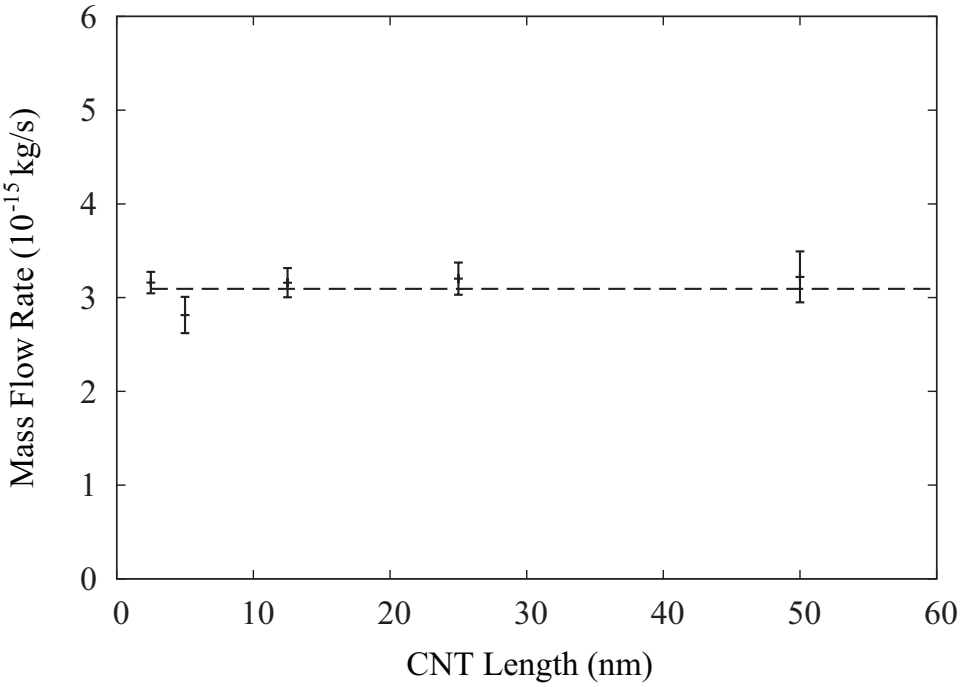

Figure 6.5: Relationship between mass flow rate and CNT length under a 200 MPa pressure difference. The horizontal dashed line indicates an average mass flow rate of 3.11×10^{-15} kg/s.

velocity [95, 136]. By using this relationship we are able to compare our average fluid velocity with that of Thomas and McGaughey [11]. They predicted a flow velocity of 5.2 m/s under a pressure difference of 73.5 MPa for a (7,7) CNT; extrapolating these values would predict a value of 14.2 m/s for a pressure difference of 200 MPa which is in good agreement with the flow velocities presented here.

The result in Fig. 6.4 is seemingly in contradiction to the results of Thomas and McGaughey (see their Fig. 3 in [11]), who observed an increase in flow velocity with applied pressure gradient; in our results the applied pressure gradient ($\Delta P/L$) is also varying, but there is no significant change in flow velocity. The contradiction only arises, however, if one assumes that the pressure gradient alone is sufficient to characterise the driving force of the flow (which is the case in classical fluid mechanics). In fact, our results suggest that, because the nanotube flow velocity is relatively independent of L, it is the pressure drop ΔP which is the characteristic flow driver, not the pressure gradient. This phenomenon has

also been discussed by Corry [95] and Suk and Aluru [99]. If this is the case, the contradiction is resolved: in the simulations of Thomas and McGaughey it is the increased pressure difference (ΔP) that is responsible for the increase in velocity they observed, and not the fact that the pressure gradient was changing; in our simulations, with ΔP fixed, the flow velocity is relatively unaffected.

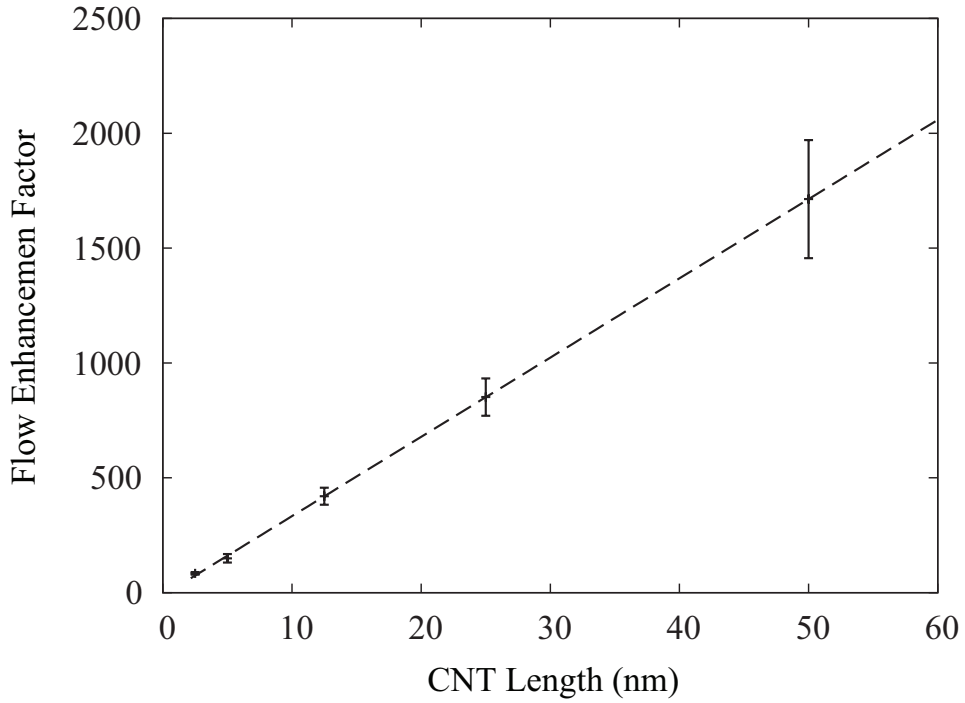

Figure 6.6: Flow enhancement factors (over hydrodynamic predictions) for different CNT lengths.

A similarly constant relationship is present between the mass flow rate and CNT length, shown in Fig. 6.5. As the fluid flow is non-continuum, the net flow rate is measured by averaging the number of molecules which cross a perpendicular plane located at the midpoint of each CNT over a prescribed time period; molecules which cross in the positive x-direction are counted as positive to the flow rate and those which cross in the opposite direction are counted as negative. The average mass flow rate through each CNT we calculated to be 3.11×10^{-15} kg/s. These measured flow rates can be compared to equivalent hydrodynamic

flow rates via the no-slip Hagen-Poiseuille relation for flow in a cylindrical pipe:

$$\dot{m} = \frac{\pi R^4 \rho \Delta P}{8 \mu L}, \tag{6.1}$$

where R is the radius of the CNT, ΔP is the pressure difference, ρ is the fluid density, μ is the dynamic viscosity, and L is the CNT length. The radius used here is related to the volume which the water can occupy inside a CNT. We take the radius within which 95% of the fluid resides, which was found to be 0.186 nm, and the reasons for choosing this value are discussed in Section 6.1.2. Bulk properties for ρ and μ for water at 298 K are used. While this equation is not strictly valid in this sub-continuum flow problem, we wish to make a comparison with hydrodynamic predictions.

The flow enhancement factor, i.e. the ratio of our measured mass flow rate to the hydrodynamic prediction, shows a linear relationship with CNT length, see Fig. 6.6. In contrast to what is predicted by hydrodynamic theory, at these large pressure differences the mass flow rate does not decrease with increasing pipe length but remains constant over the lengths considered in this study. Flow enhancement values are in agreement with those reported by Corry [95] of $\mathcal{O}(10)$ at the shortest lengths, and Thomas and McGaughey [11] of $\mathcal{O}(1000)$ at the longest lengths. The reduction of the flow enhancement factor is not due to a lower mass flow rate in shorter CNTs, as discussed in [11]. On the contrary, the measured mass flow rate in short CNTs is comparable to that in longer CNTs. Therefore at a fixed pressure difference, the flow enhancement factor is directly proportional only to the CNT length.

6.1.2 Radial and axial profiles, inlet and outlet effects

To investigate the radial structure of water in CNTs we measured the mean distribution of radial density for each CNT, see Fig. 6.7. We used 100 cylindrical bins of equal volume, centred radially inside the midpoint of the CNT, and covering a fixed length of 1 nm axially. The density within each bin is measured by summing the mass of water molecules contained over a specified period of time and dividing it by the axial sampling length and the number of averaging time-steps.

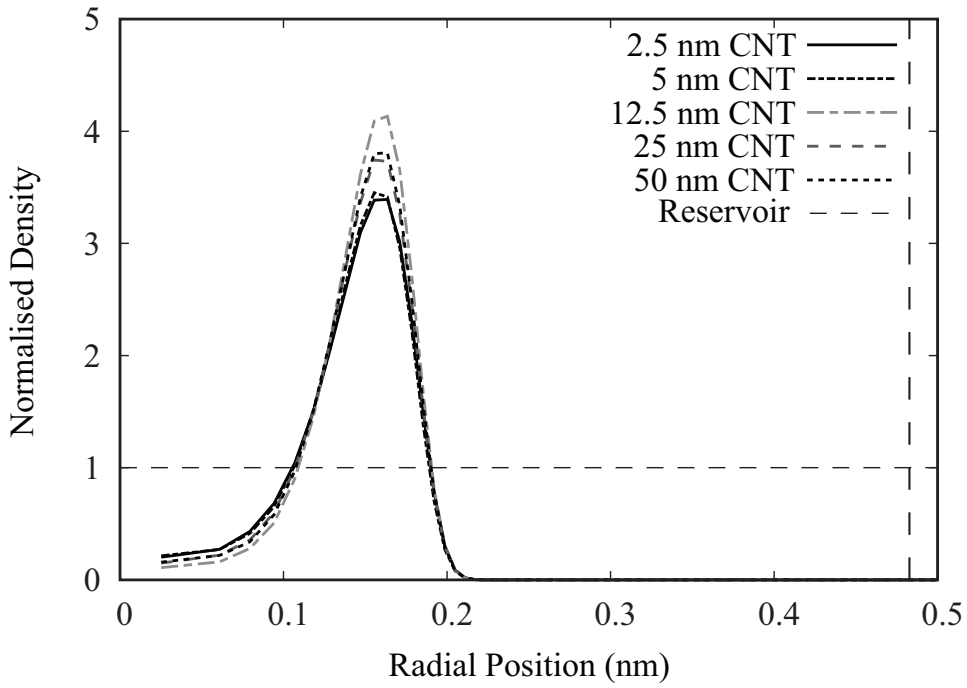

Figure 6.7: Radial density distributions normalised with the reservoir density for CNTs of different lengths. Measurements are taken at the midpoint of each CNT length. The vertical dashed line at the right indicates the position of the CNT surface.

Figure 6.7 shows that the average density profile is annular, also seen in Fig. 6.8, with a peak fluid density much higher than that of the reservoir (measured using the same technique). The total fluid density is dependent upon the definition of the occupied volume of the CNT, for which there is no consistency in the literature [44]. The distance between the peak density radius and the CNT surface corresponds to the interaction length of the Lennard-Jones potential be-

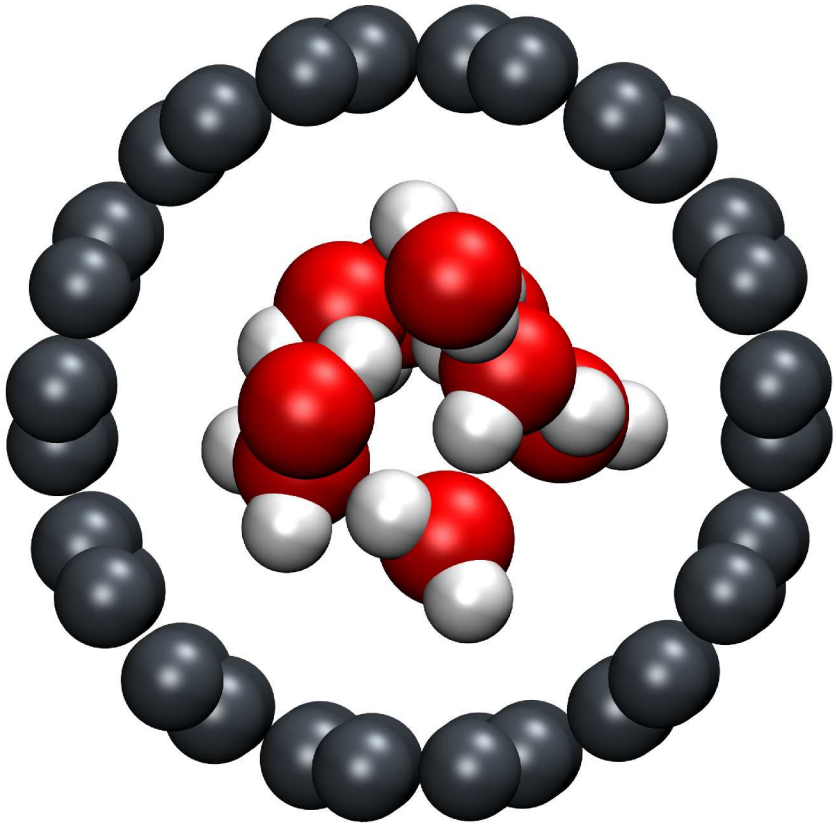

Figure 6.8: TIP4P water inside a 2.5 nm long (7,7) CNT forms an annular structure and shows no signs of ice formation.

tween the carbon and oxygen atoms, σ_{CO}, and is unaffected by changes in CNT length. We consider the occupied volume of the CNT to be where 95% of the water resides which is calculated using the area under the radial density graph. The choice of 95% is arbitrary but makes more physical sense than using either the van der Waals radii of carbon and water or a combination of both values.

It is clear from Fig. 6.7 that even in very short channels molecular ordering is present which may be a result of single or multiple-stranded molecular transport. Mattia and Gogotsi [3] imply that ordered diffusion takes a certain length to develop; if such a minimum length does exist, it must be very small. The minimal

variation in the density peaks between the various CNTs can be explained by small changes in the axial profiles of density, shown in Fig 6.10. We note that our radial density profiles are similar to previous results [44] but the molecular arrangements may differ. The arrangement of water molecules inside CNTs is affected by a number of factors, and the choice of water model has been shown to be one of the most influential [110], as discussed in Section 3.3.

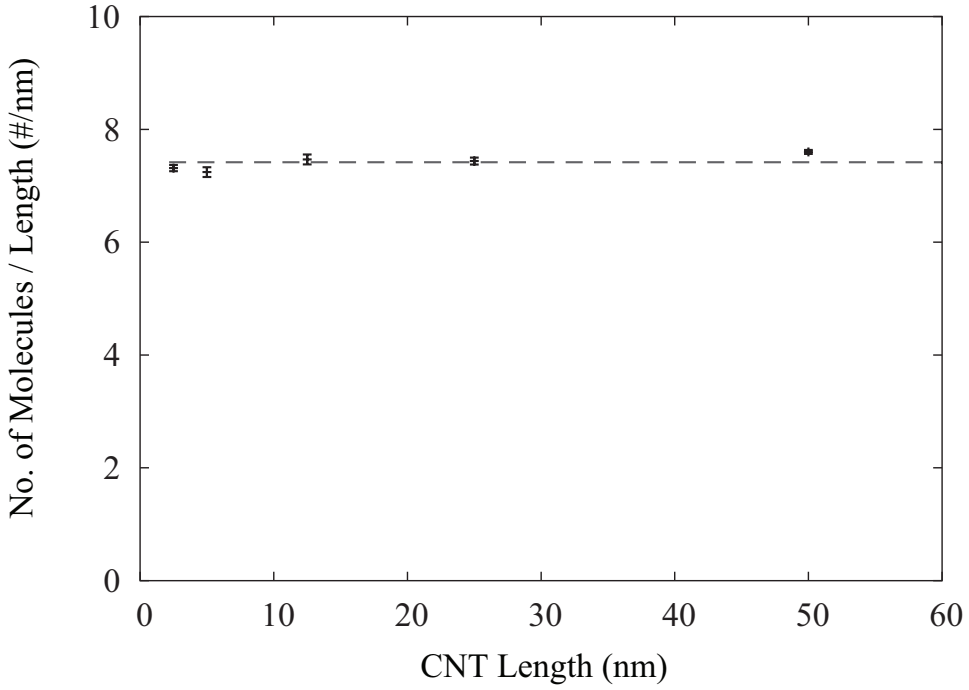

Figure 6.9: The total water density (defined as the number of molecules per nm length) inside (7,7) CNTs with different lengths subject to the same pressure differences. The horizontal dashed line indicates the average value of total density.

The changes in volume between cases are only related to changes in length since the occupied cross-sectional area is the same. Therefore the total density in each case can be related through the average total number of water molecules per unit length in each CNT, as shown in Fig. 6.9. Over the range of lengths considered in this study, the total density of water inside a (7,7) CNT is not affected by changes in nanotube length.

A significant insight into the transport behaviour of water through CNTs of varying length is available through examining the axial profiles of hydrodynamic

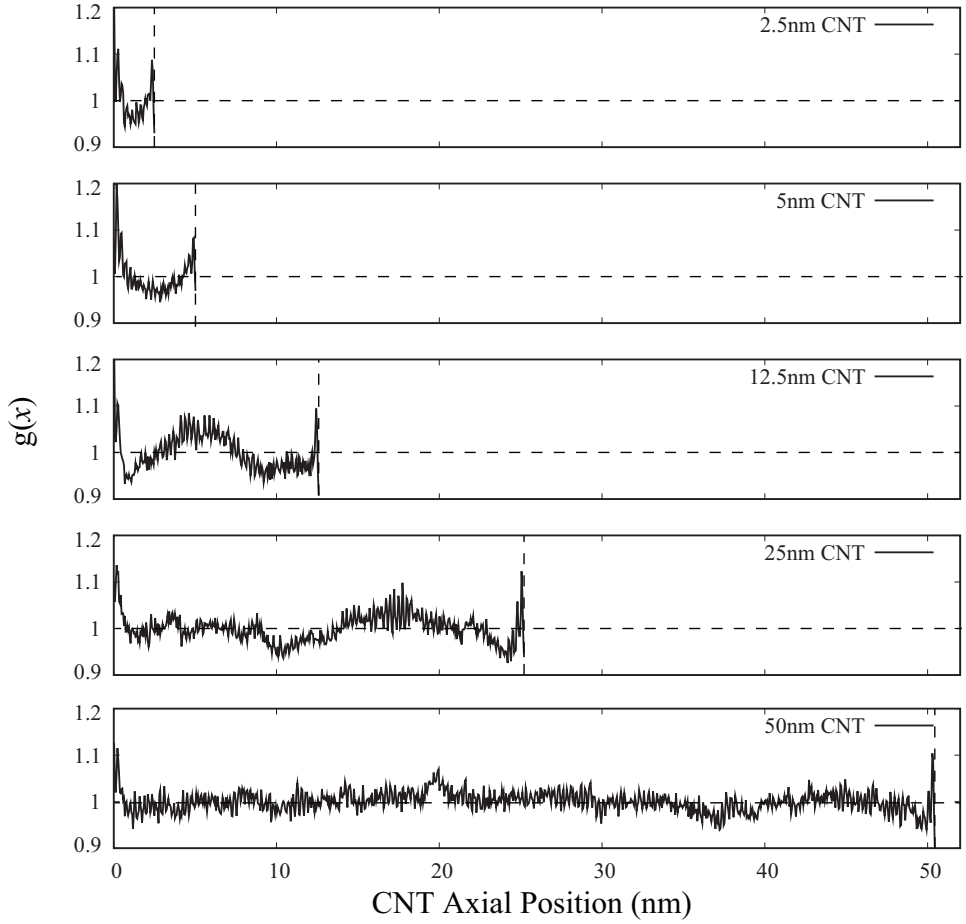

Figure 6.10: Axial distribution functions for various CNT lengths.

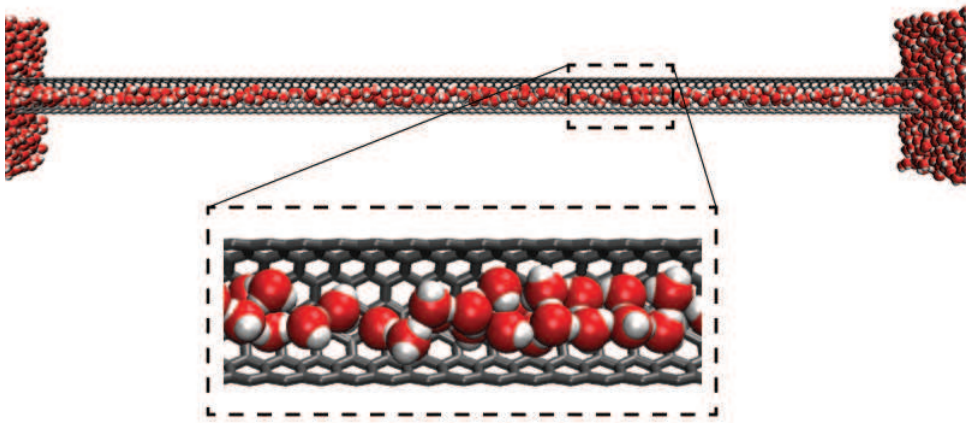

Figure 6.11: Snapshot of water structure inside a 25 nm long (7,7) CNT after 4 ns of simulation time.

properties. The axial distribution function (ADF) in each CNT is measured by using the binning technique described in [118] and is presented in Fig 6.10.

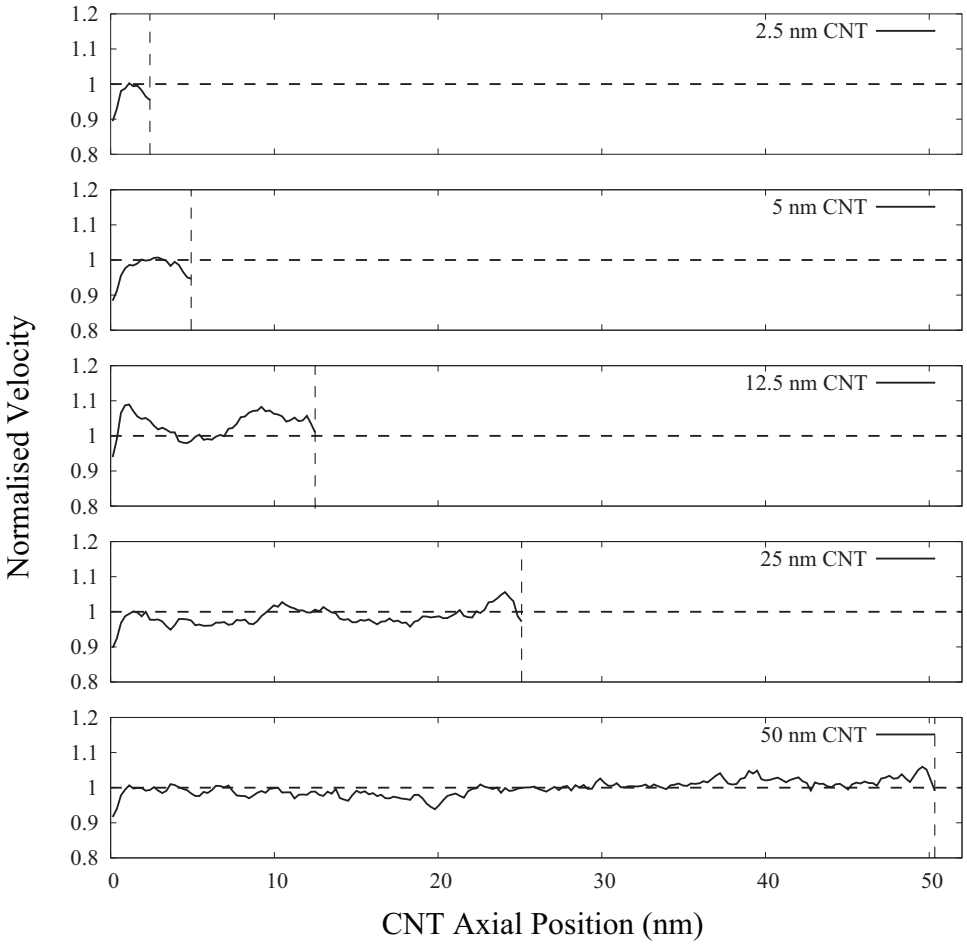

Figure 6.12: Normalised axial velocity profiles for various CNT lengths.

Velocity and pressure profiles measured using standard techniques are shown in Figs. 6.12 and 6.13, respectively. In order to make comparison across the five CNTs, we use the same bin width for all axial profiles, and average over a time-period of 4 ns. We note that temperature profiles remain uniform across all the CNTs at ∼298 K. Pressure errors measured at the inlet/outlet of all the CNTs are within 15% of the reported values.

Water transport along a CNT is subject to inlet/outlet effects which manifest themselves in changes to fluid properties at the entrance and exit regions of the nanotube. The fluid has a higher density in these regions, with a corresponding drop in the fluid velocity. The peaks of the ADFs at the inlet and outlet of all CNTs may be caused by the simplified representation of the membrane, with the

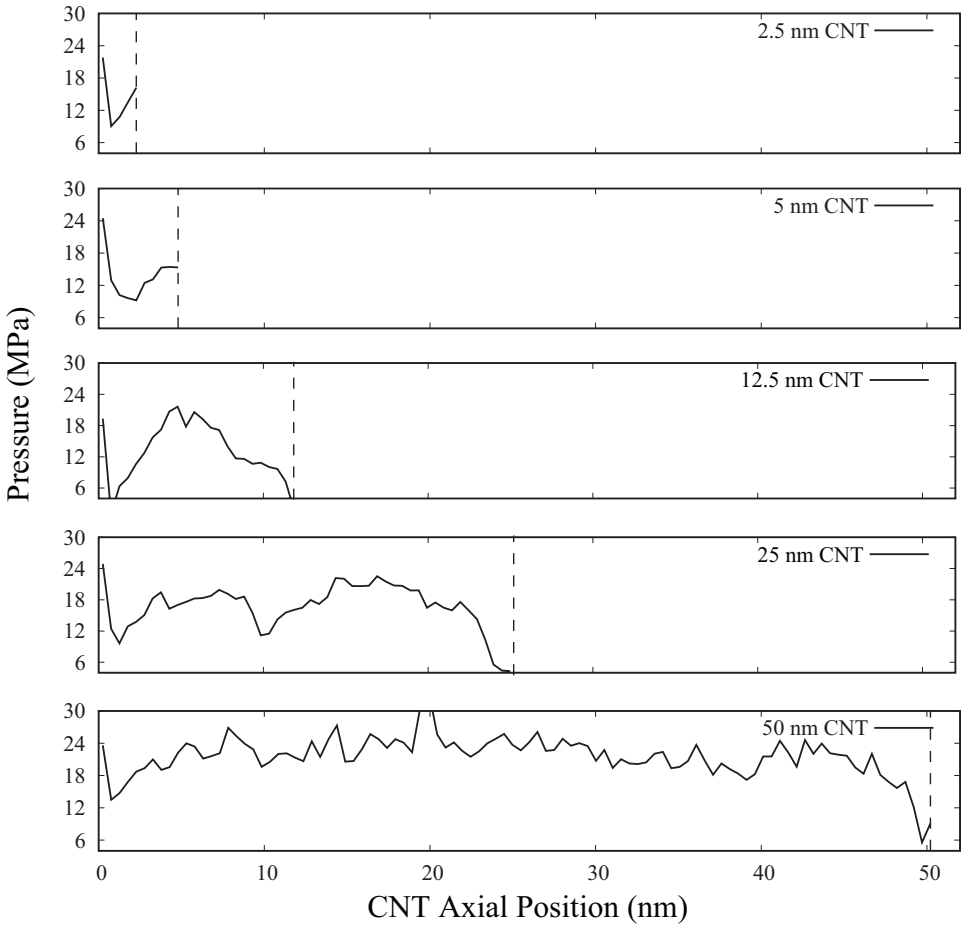

Figure 6.13: Axial pressure profiles for various CNT lengths.

fluid inside the CNT interacting with the membrane walls. We note that this membrane model is commonly used in these types of simulations and that the inlet and outlet conditions are consistent for each CNT. The effect is to cause small dips in the axial density in the shorter CNTs and steady oscillations in the longer CNTs (diminishing in the 50 nm CNT). These slight changes in density do not affect the mass flow rate as the fluid velocity adjusts accordingly to conserve mass flow rate, as seen in Fig. 6.12.

The variations of the ADF in each case may be explained by the fluid structure changing from multiple strands of molecules into a single strand at random locations along the CNT axis, as shown in the simulation snapshot in Fig. 6.11. This means that when multiple strands are present the measured axial density

will be greater.

6.1.3 Frictionless flow

The fact that the CNT length appears to have no influence on the mass flow rate is counter-intuitive from a hydrodynamic perspective (in fact, mass flow rate appears to slightly increase with length in some cases, as seen in Fig. 6.5). Consider the hydrodynamic expression for mass flow rate, Eq. 6.1: at such small scales, we might expect the viscosity to drop, and thus increase the mass flow rate – this is consistent with a hydrodynamic viewpoint. However, we would generally expect the viscosity to be independent of the length of the CNT, and so the question remains: why is mass flow rate constant for every L?

An explanation might be that the flow is effectively frictionless in the nanotube. But this cannot be the case, since a frictionless tube would imply an infinite flow rate for a fixed pressure drop, ΔP. The resolution to this paradox lies in Fig. 6.13. Clearly, the flow in the CNT, for each length, is not frictionless: the pressure at the inlet is greater than the pressure at the outlet in every case. This pressure loss, which results from frictional forces, appears mainly to result from a short development length at the inlet in the shorter CNTs, and a short exit region in the longer CNTs. So, in the longer CNT simulations, central "developed" regions are present that are effectively frictionless in contrast to the entrance/exit regions. As the CNT increases in length, these "frictionless" central regions cover proportionally more of the total CNT length, to the point where extensions in CNT length result in roughly equal extensions to the central frictionless region. This is potentially why, for CNTs above a certain length (greater than the short entrance/exit region), the mass flow rate is relatively unaffected by changes in CNT length. However, the independence on L appears to be evident at the smallest channel lengths considered here; more simulations at smaller channels would be required to confirm this hypothesis.

Another reason why the flow in a CNT appears to behave as effectively fric-

tionless, is because the majority of viscous losses occur in the upstream reservoir, before the inlet (as evidenced by the order of magnitude difference between the inlet pressure and the upstream reservoir pressure, as seen in Fig. 6.13). It is possible that this pressure loss, which dwarfs the total head loss through the CNT, is independent of L since it occurs external to, and upstream of, the CNT. The question that remains unanswered is whether these large external pressure drops are physically realistic or merely an artefact of the MD domain setup for this type of CNT investigation. Either way, the source of these external losses and their role in determining CNT flow rate is vitally important to establish.

Pressure fluctuations are greater inside the CNTs due to the tight packing of the molecules, so any slight variations in density can cause large changes in pressure due to the high gradient of the intermolecular potential at these small molecule separations. These results would benefit from longer averaging periods to reduce the current level of fluctuation.

6.1.4 Hydrogen bonding and orientation

The average number of hydrogen bonds per water molecule is measured in the midpoint region of each CNT and is shown in Fig. 6.14. The criteria for establishing when a hydrogen bond is formed is discussed in detail in Chapter 4. The average number of hydrogen bonds per water molecule was measured to be 2.3, which is in good agreement with previous studies [107, 133]. The amount of hydrogen bonding inside a (7,7) CNT is unaffected by changes in nanotube length, but has been shown previously to be dependent upon CNT diameter [107].

Local hydrogen bond dynamics are investigated using a radial binning technique similar to that for measuring radial density, as discussed previously. This enables the average number of hydrogen bonds relative to CNT radial position to be observed: radial hydrogen bond profiles are shown in Fig. 6.15. The profile remains fairly uniform across the CNT radius with a slight increase towards the CNT axis, however it does not approach a bulk value (3.6) at the axis of

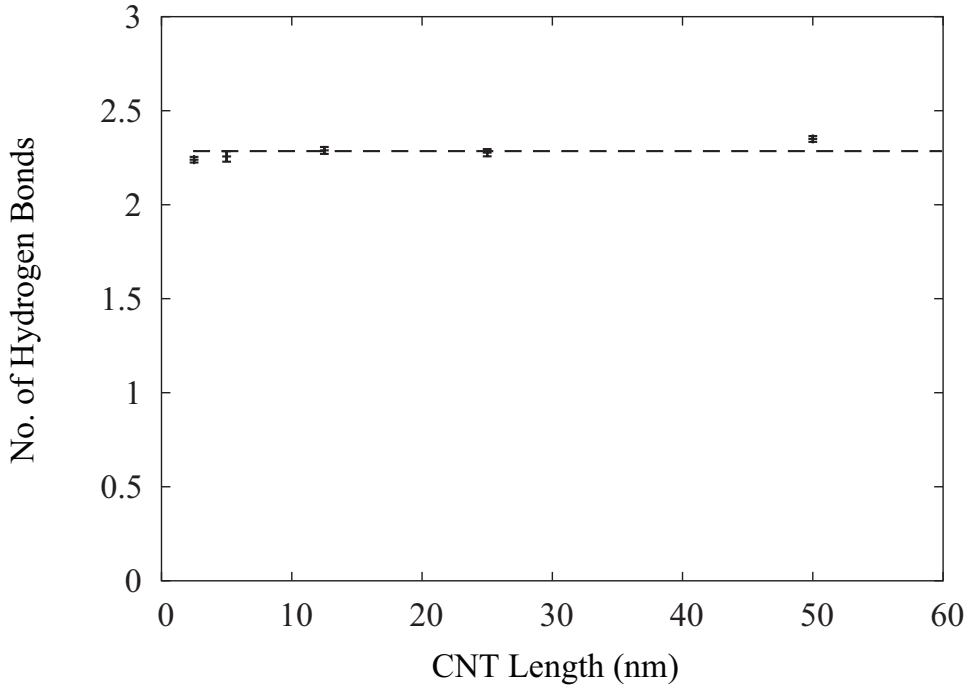

Figure 6.14: Relationship between average number of hydrogen bonds per water molecule and CNT length.

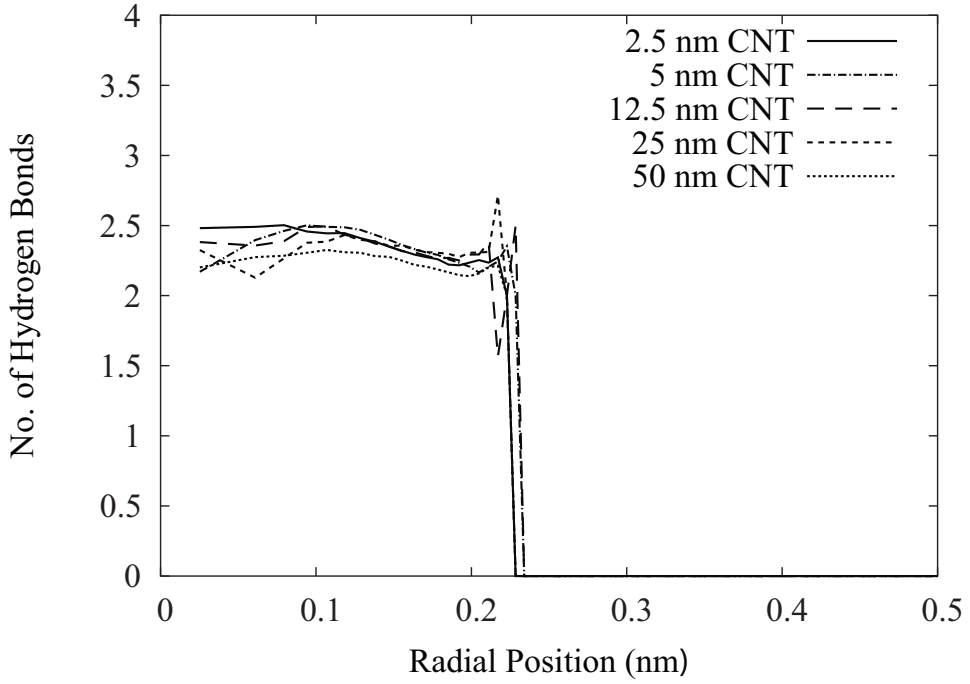

Figure 6.15: Radial hydrogen bonding profiles inside (7,7) CNTs of different lengths.

the CNT as would be expected in larger diameter nanotubes [109]. Hanasaki

and Nakatani [133] investigated radial hydrogen bond profiles in (6,6) and (8,8) CNTs and the results presented here for the (7,7) CNT are located between these profiles. As before, the hydrogen bond network is unaffected by changes in CNT length.

The angle between the water dipole moment and the x-axis is measured at every time-step for water molecules at the inlet, midpoint, and outlet of the 2.5, 12.5 and 50 nm long CNTs, and normalised histograms are created, shown in Fig. 6.16. It is clear from these results that there are two preferred orientations of the water molecules (measured anti-clockwise from the x-axis): 0 degrees and 180 degrees for each CNT length. This means the water dipoles align themselves with the CNT axis and point towards the centre of the CNT at both the inlet and outlet, which suggests a strong coupling between the water molecules in these regions and molecules in the reservoirs. This coupling effect becomes greater in longer CNTs – illustrated by sharp peaks at the inlet and outlet of the 50 nm long CNT, shown in Fig. 6.16c). These results also show that the water molecules flip orientation as they travel down the CNT, which is in agreement with the findings of Xiao-Yan and Hang-Jun [134]. The role that water molecule orientation plays in water transport rates though CNTs remains unclear and further research is required. The dipole orientation may be affected by the simplified electrostatic interaction used in this study, which should be investigated in future work.

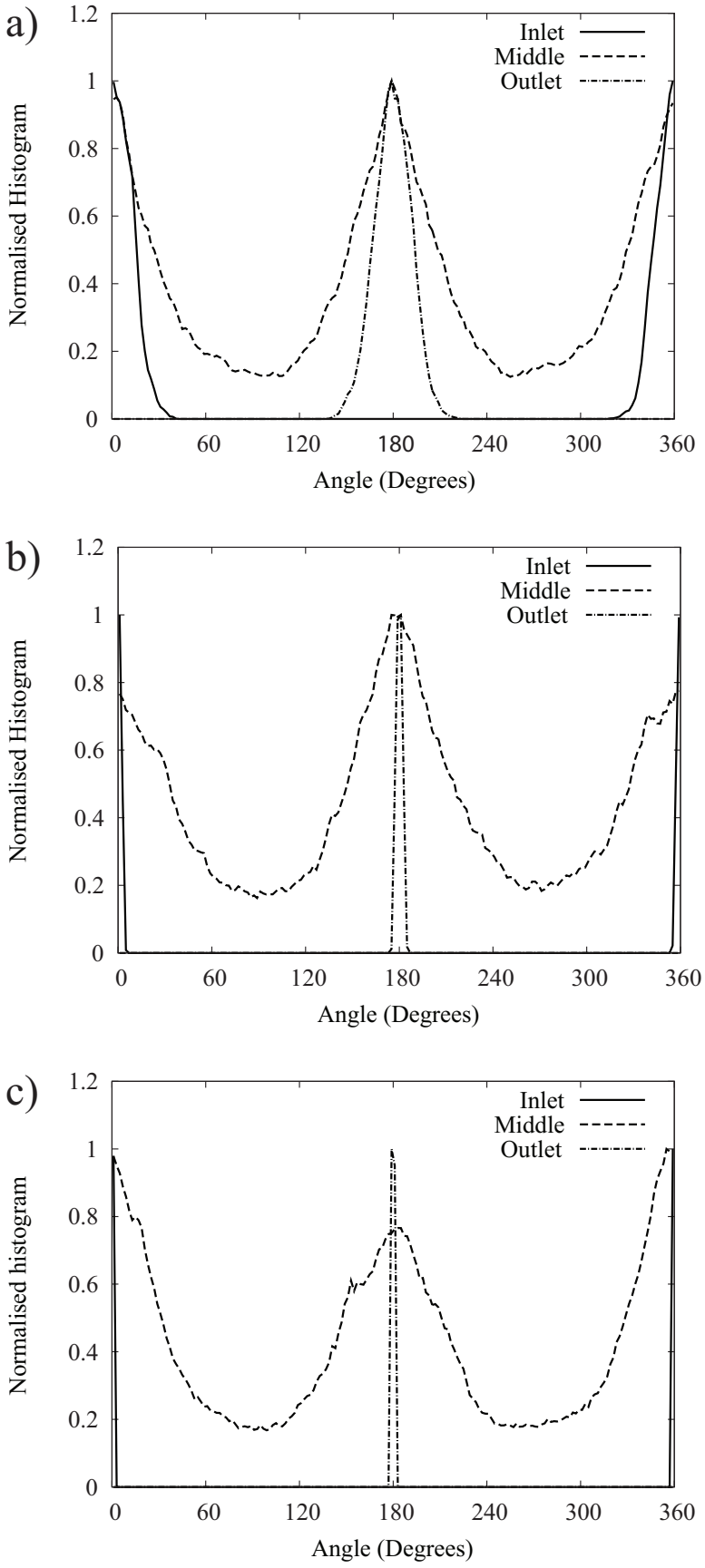

Figure 6.16: Water dipole orientation at the three different locations noted along the a) 2.5 nm, b) 12.5 nm and c) 50 nm long CNT axis.

6.2 Water transport through CNTs with defects

Very few MD studies include defects when modelling CNTs; pristine, defect-free CNTs are commonly studied, as in Section 6.1. This leaves a gap in our understanding of water transport through these nanoscale structures.

CNT defects are, however, commonplace in experiments as it is very difficult to manufacture pristine CNTs, e.g. during the uncapping procedure (typically plasma oxidation) functionalisation defects are produced that have been shown through simulation [69, 70] and experiment [57] to reduce water transport rates. Other defect types that can occur during the manufacturing process are: Stone-Wales topological defects, adatoms, and vacancy sites. Vacancy sites are structural defects that can be mono-vacancies or multi-vacancies in the walls of CNTs [77, 78]. The properties of CNTs, including fluid transport, will be affected by the presence of these defects on their inner-walls and tips.

We have shown in the previous section that the flow enhancement factor, defined as the ratio of the MD simulated mass flow rate to the hydrodynamic prediction, increases linearly with CNT length for a fixed pressure difference. If this trend continues up to the lengths used in experiments, which can be 2-5 μm, then the flow enhancement factor would far exceed those reported from experiments. The inclusion of defects in the present MD study may help to understand the role of defects in flow enhancement.

There are many published papers that assess the change in mechanical properties of CNTs due to the inclusion of defects. Yang *et al.* [78] included functionalised, Stone-Wales, and vacancy type defects in their MD study of the tensile strength of CNTs, and found that their inclusion produced weaker CNTs. They also found that the tensile strength of the CNT became comparable to the lower values reported in experiments, rather than the exceptionally high theoretical values found from calculations assuming defect-free CNTs.

There are only a few reports of the effect of CNT defects on fluid transport. Li *et al.* [76] modelled using MD the permeation of water through CNTs with

Stone-Wales defects. They found that the flow rate decreased with an increasing number of such defects. Kotsalis *et al.* [81] performed MD simulations of water inside CNTs doped with oxygen and hydrogen, and found that the wetting contact angle of water reduced with increasing doping sites, making the CNTs more hydrophilic. CNT functionalisation (tip and core) reduces water transport rates, as discussed previously. To our knowledge, there has been no report of the effect of CNT vacancy site defects on the water transport rate.

We now use MD simulations to investigate water transport through (7,7) single-wall CNTs of a fixed length of 25 nm and examine how changing the number of vacancy defects affects the fluid flow behaviour. The number of defects is quantified by the percentage of carbon atoms which are removed from the original, defect-free structure.

A single-wall CNT with missing carbon atoms would not be a stable structure on its own due to the presence of unsaturated bonds, however such a case is plausible for a multi-wall CNT with an inner shell having the diameter of a single-wall CNT with vacancy sites. For desalination applications, semipermeable CNT membranes will most likely be composed of multi-wall CNTs [3]. Four cases are considered herein: 0%, 5%, 10%, and 20% vacancy defect densities, and we report the effect these have on fluid flow rates, fluid densities and axial pressure profiles.

The simulation method is the same as described in Section 6.1: a pressure difference is created across a CNT membrane using a combination of a PID controller and a pressure flux technique. A time-step of 1 fs is used in all the following simulations. The TIP4P water model is used and the carbon-water interaction is represented by the LJ potential of Werder *et al.* [106]. Electrostatic and Lennard-Jones interactions are smoothly truncated at 1.0 nm.

Single carbon atoms are removed at random places within the original defect-free nanotube structure, until the required percentage of defects is reached. Higher-order vacancy clusters (groups of three or four single defects) occur in the 10% and 20% defect cases. The modelling of the CNT as a rigid structure may there-

fore introduce errors in cases with high defect densities, and this should be the scope of future work

6.2.1 Results and discussion

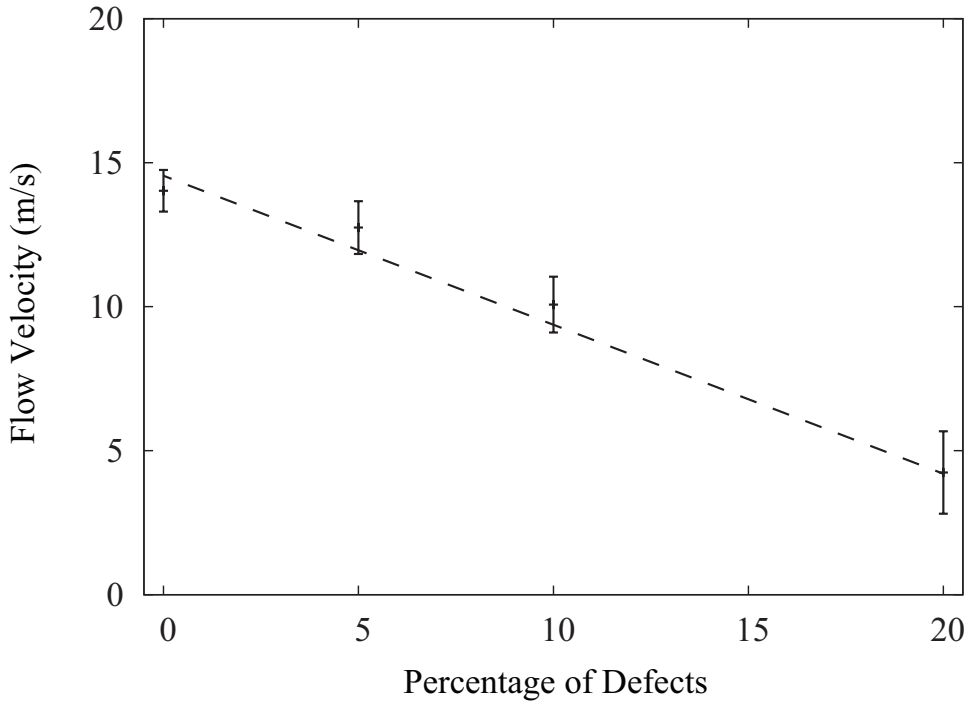

Figure 6.17: Variation of flow velocity with percentage of CNT defects for a 200 MPa pressure difference.

The average fluid streaming velocities for different percentages of vacancy defects under the same applied pressure difference are shown in Fig. 6.17. We find that increasing the number of defects reduces the average fluid velocity through the nanotubes. Small numbers of defects (5%) cause the fluid velocity to reduce by ∼10%, however greater quantities of defects cause a reduction of ∼70%. Defect densities are likely to be less than 10% in CNTs [78] and these results show a significant reduction in fluid velocity may be present in this range.

The net mass flow rate is measured by averaging the number of molecules which cross five equidistant planes inside each CNT over a prescribed time period, and is shown in Fig. 6.18. The mass flow rate decreases with increasing numbers of

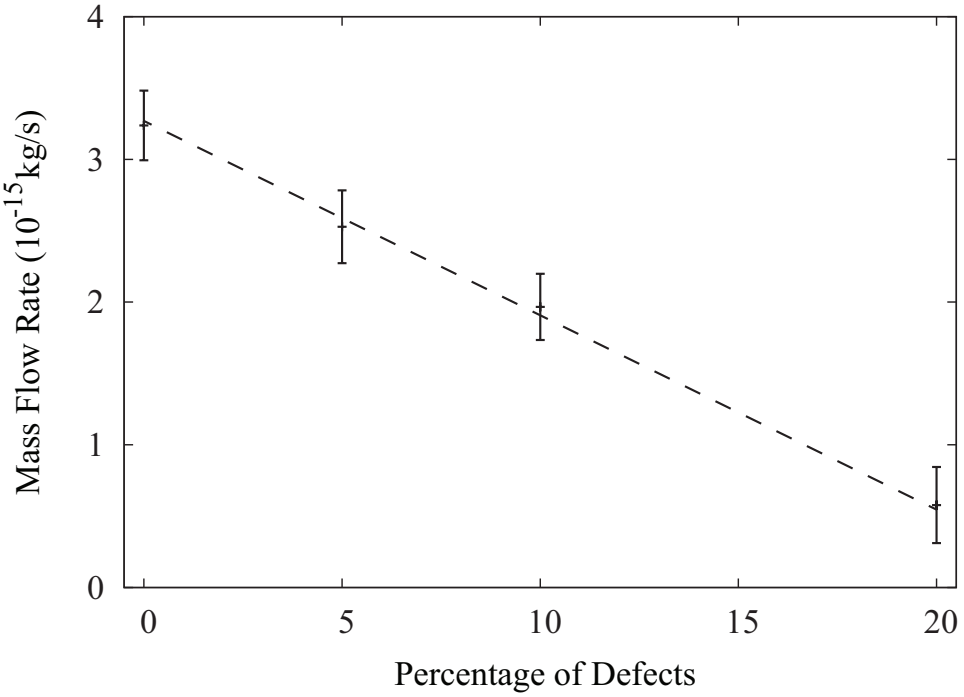

Figure 6.18: Relationship between flow rate and percentage of CNT defects for a 200 MPa pressure difference.

defects, however the effect of including vacancy defects at lower densities is more influential: ∼20% reduction in flow rate for 5% defects, and ∼80% reduction for 20% defects. Increasing the number of vacancy defects causes a linear reduction in the resultant mass flow rate and flow velocity.

The mean distribution of radial water density for each CNT is shown in Fig. 6.19. The average density profile for each case is annular and the peak density occurs at the same radial position, which indicates that the inclusion of vacancy defects has not altered the CNT effective radius. The radial density decreases with increasing numbers of defects, which means that the water molecules are not as tightly packed in the radial direction in CNTs with vacancy defects. The total fluid density is dependent upon the definition of the occupied volume of the CNT which is difficult to define, as discussed previously, but we know that this volume is the same for each CNT in this study since the effective radius and length are consistent in each case. Therefore the total fluid density can be described by the total number of water molecules contained within each CNT, and

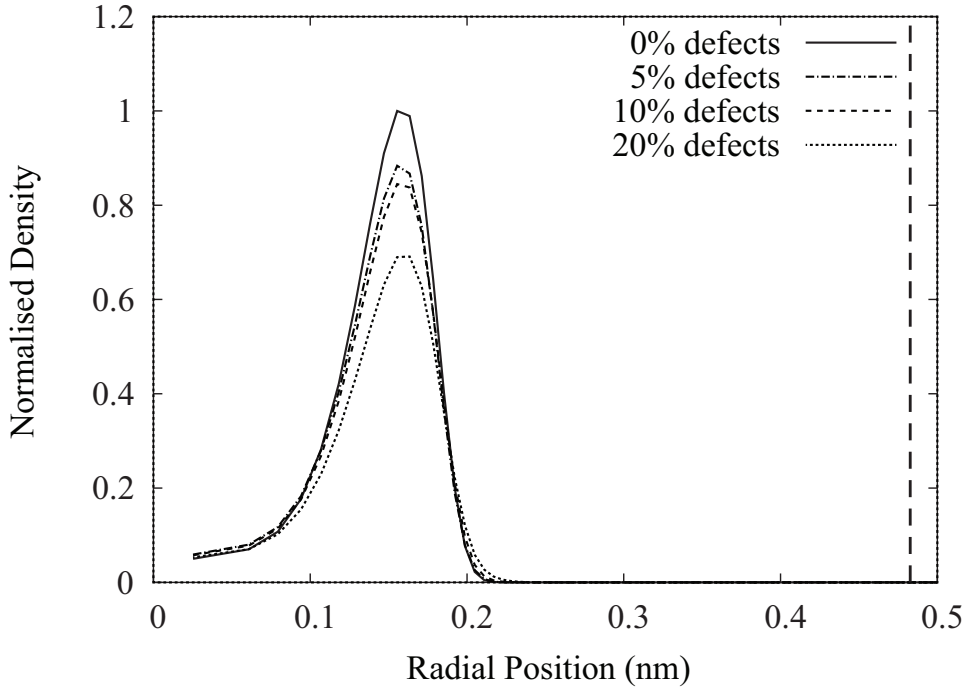

Figure 6.19: Normalised radial water density distributions for CNTs with different numbers of defects present. The vertical dashed line at the right indicates the position of the CNT surface.

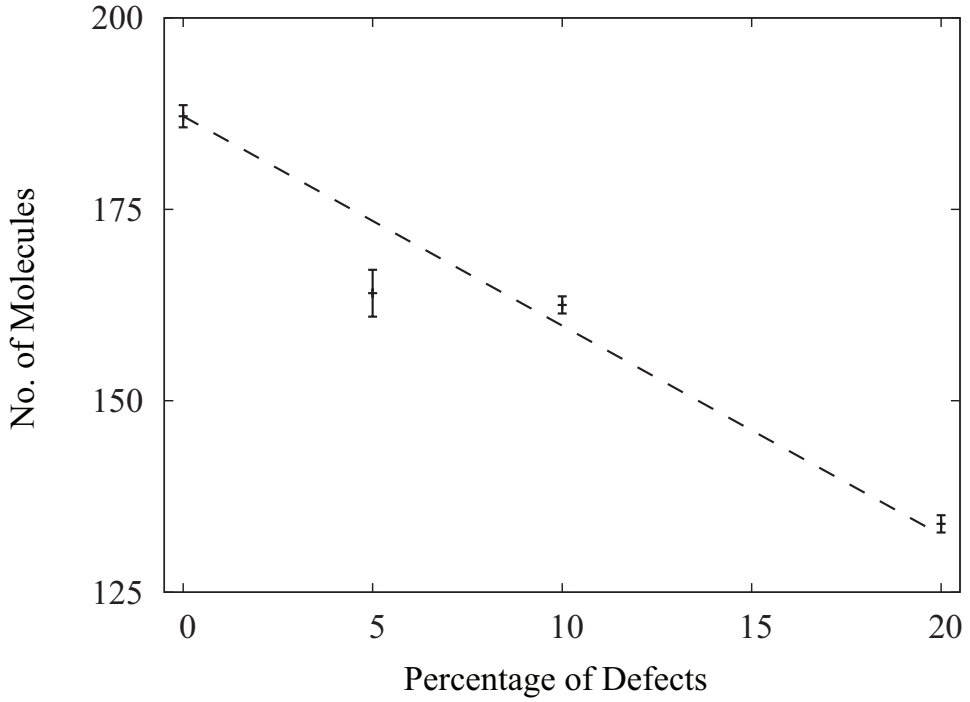

Figure 6.20: Relationship between the average number of water molecules in the CNT and percentage of defects.

is shown in Fig. 6.20. The average number of water molecules inside each CNT decreases with increasing defects; the inclusion of vacancy site defects disrupts the optimum internal fluid structuring so that the number of water molecules that can occupy the CNT is reduced.

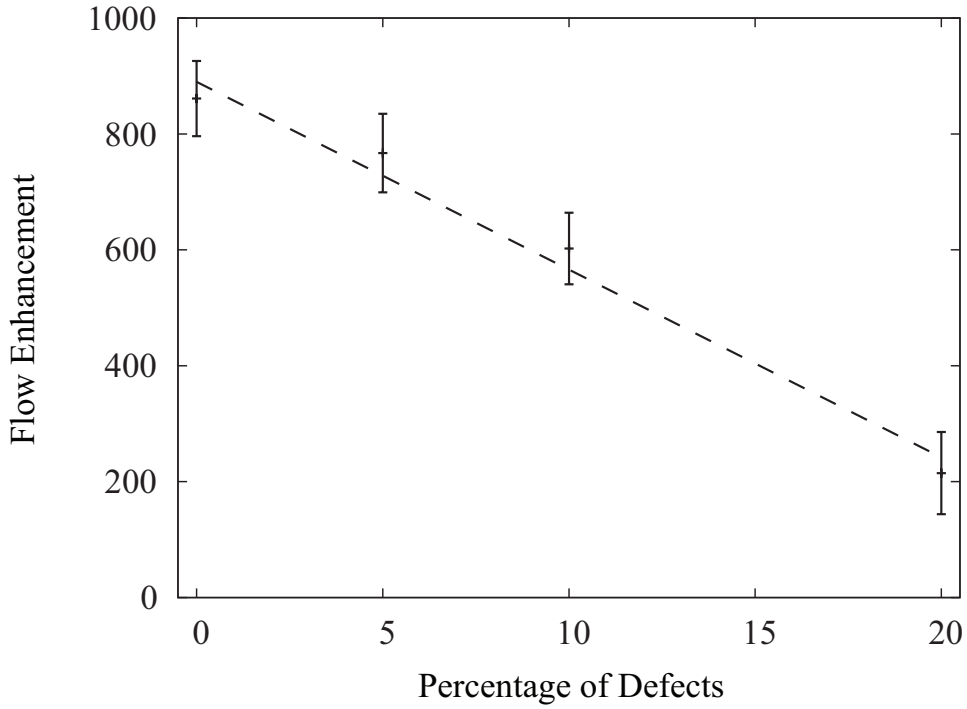

Figure 6.21: Flow enhancement for different percentages of defects, for a 25 nm CNT under a 200 MPa pressure difference.

The measured flow rates can be compared to predicted hydrodynamic flow rates via the no-slip Poiseuille relation, Eq. 6.1, as before. Bulk properties for ρ and μ for water at 298 K are used in the defect-free case and ρ is calculated to include the reductions in density experienced in CNTs with defects. The flow enhancement factor for each case is shown in Fig. 6.21. This non-linear reduction in the flow enhancement factor with increasing number of site defects is caused by the combined lower fluid density and flow velocity.

The ADF of water contained within (7,7) CNTs with different numbers of defects is shown in Fig. 6.22. The ADF in the defect-free case remains constant along the entire length of the CNT, as shown in Section 6.1. Significant deviations are present in cases with vacancy site defects, and as more defects are introduced

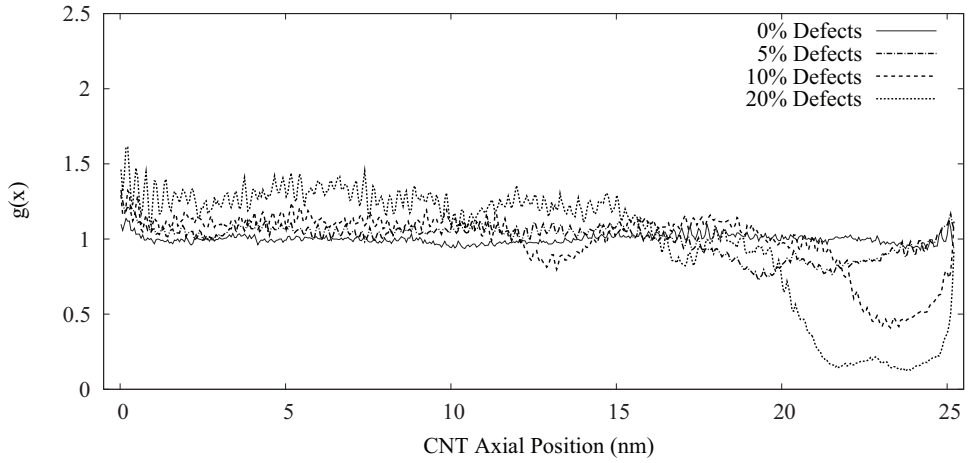

Figure 6.22: Axial distribution function (ADF) of water in CNTs with vacancy site defects.

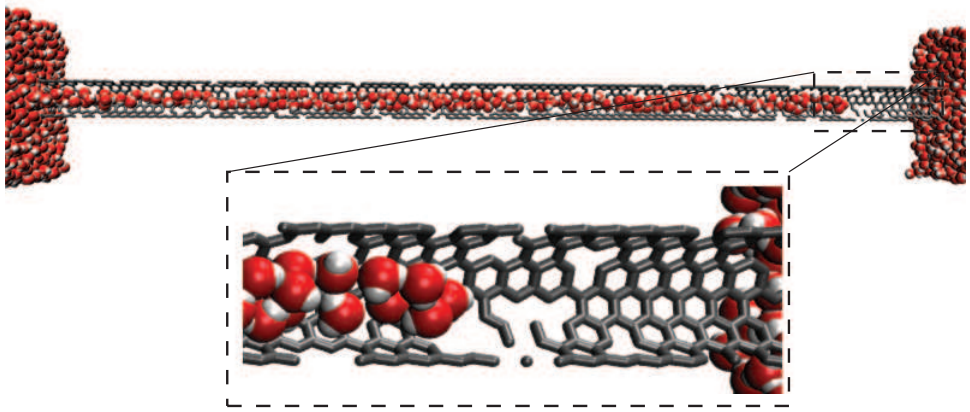

Figure 6.23: Snapshot of water structure inside a (7,7) CNT with 10% vacancy site defects after 4 ns of simulation time.

into the CNT walls, these deviations become greater. The ADF profiles show that water is compressing in certain regions and expanding in others within defective CNTs. These effects are amplified when greater numbers of defects are present. The drops in axial density are representative of breaks in the normally continuous structure of water, which is shown for the 10% defect case in Fig. 6.23. This suggests that the transport mechanism of water in defective CNTs may occur through bursts rather than continuous diffusion, which in turn reduces the fluid flow rate.

The axial velocity profile, shown in Fig. 6.24, is also affected by the inclusion of vacancy site defects. The water streaming velocity remains fairly constant for

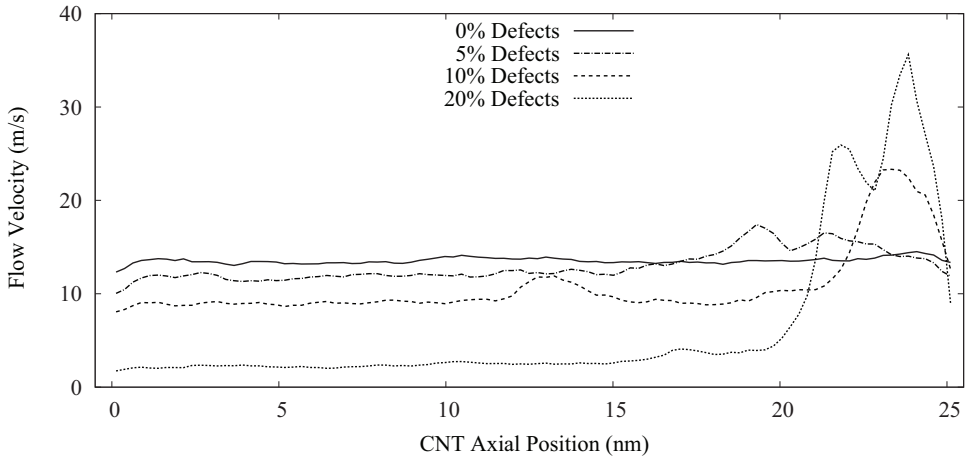

Figure 6.24: Axial velocity profile of water in CNTs with vacancy site defects.

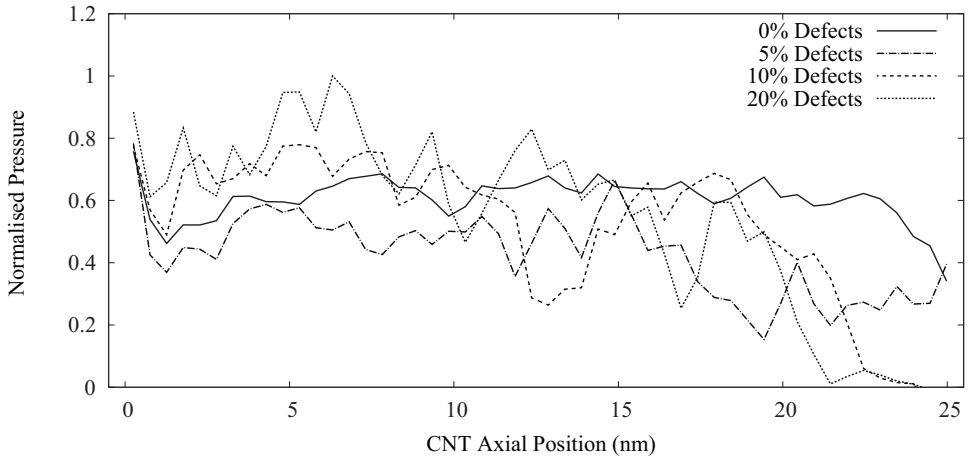

Figure 6.25: Axial pressure profile of water in CNTs with vacancy site defects.

each case along the majority of the length of the CNTs before demonstrating large peaks towards the end of the CNTs in the cases with defects. In these regions the water density is much lower and we would expect the velocity to increase to preserve mass continuity from a macroscopic perspective. However, due to the lower fluid density in this region the accuracy of the velocity measurement will be reduced, which makes drawing conclusions about mass flow conservation difficult due to the uncertainty of the actual velocity profile at this location inside the nanotube.

To further understand why the average fluid velocity decreases when defects are present, we must consider the axial fluid pressure profile along each CNT,

shown in Fig. 6.25. The presence of vacancy site defects causes the pressure profiles to deviate substantially from the frictionless profile present in the 0% defect case (also reported in [105]). The flow becomes more like flow in a rough pipe: the greater pressure losses reduce the average fluid velocity.

6.2.2 Summary

We have reported new results of non-equilibrium MD simulations of water transport through (7,7) CNTs, in particular how changing the CNT length and introducing vacancy site defects affects the internal flow dynamics. Using new fluid pressure MD control techniques we have shown that under the same applied pressure difference an increase in CNT length has a negligible effect on the mass flow rate and fluid flow velocity. This results in larger flow enhancements over hydrodynamic expectations for longer CNTs. At a fixed pressure difference, the flow enhancement factor is directly proportional only to the CNT length.

By examining axial profiles of hydrodynamic properties we have found that entrance and exit effects are significant. Large viscous losses are experienced in these regions, shown by dips in the axial pressure profiles. In longer CNTs, central "developed" regions are present that are effectively frictionless. These regions extend proportionally with the length of the CNT, resulting in mass flow rates which are unaffected by an increase in CNT length.

Including defects reduces the fluid velocity and mass flow rate rate considerably. Mass flow rate is further affected by a reduction in the overall fluid density caused by the presence of the defects. Vacancy sites disrupt the smooth, continuous potential energy landscape a CNT provides, causing greater pressure losses along it, which reduces the overall fluid velocity. Flow enhancement factors are reduced significantly with increasing numbers of defects, which may account to some extent for the over-prediction of fluid flow rates in MD simulations using pristine CNTs when compared with experimental results.

Chapter 7

Conclusions

This thesis provides new insight into the fundamental behaviour of liquids at the nanoscale, based on results from MD simulation. Simulations were performed of liquid argon and water flowing in and around CNTs using existing and novel boundary conditions to generate fluid transport. By utilising continuum-based boundary conditions, we investigated the external flow of argon past a CNT using a fully periodic domain, and one which was non-periodic in one direction. A study of pressure-driven liquid argon through a (16,16) CNT embedded in a solid membrane was performed and compared with hydrodynamic predictions. Water transport through (7,7) CNTs of different lengths was investigated to understand how this physical dimension affects internal fluid behaviour. Finally, the influence of vacancy site defects in (7,7) CNTs on water transport was investigated. The main findings are summarised in the following.

We have extended the original measurement framework of Borg [19] to measure hydrodynamic properties of polyatomic fluids in the OpenFOAM code. A novel procedure for measuring hydrogen bonding of water molecules has been described. We have developed two novel simulation models to generate fluid transport through a nanotube membrane between two fluid reservoirs. The first model controls only the fluid density in the reservoirs to user-defined values, creating a chemical potential across the membrane, which in turn generates a

pressure difference. This technique has been successfully used to create a pressure difference across a CNT membrane using liquid argon as the working fluid. The main disadvantage of this method is that the pressure difference is an output of the system rather than an input. Our second model allows the user to set the required pressure difference explicitly and, by using a deletion patch at the outlet, create an open system which allows flow to develop in the downstream reservoir. Fluid pressure is controlled in the upstream reservoir by using a proportional-integral-derivative (PID) feedback algorithm, which works well at high pressures ($\sim$100 MPa) but can cause instabilities in a simulation at low fluid pressures ($\sim$1 MPa). The downstream reservoir is typically at atmospheric conditions, therefore we use a pressure control technique adapted from hybrid CFD-MD simulations that applies a constant external force and has been shown to work well at low pressures. However, this method requires a trial and error procedure to set the fluid to the correct conditions. We used this model to simulate water transport through CNT membranes.

Using the recently developed controllers of Borg *et al.* [1], we have applied continuum fluid boundary conditions in MD to simulate liquid argon flow past a CNT and through a CNT membrane. These simulation techniques are not dependent upon periodic boundary conditions and can be adopted in future hybrid continuum-atomistic simulations. We studied the external flow of liquid argon past a CNT, initially in a fully periodic domain, followed by the same CNT in a smaller, partially-periodic domain. By replacing the periodic boundary conditions in the streamwise direction, we were able to shrink the length of the domain considerably thus increasing the simulation's computational efficiency: the partially periodic case was $\sim$3 times faster than the fully periodic simulation. By using a combination of a mass flow inlet and an external boundary force at the outlet, we were able to accurately reproduce the results from the fully periodic case. We also found that in both cases the velocity profile across the CNT deviated from what would be expected at the macroscale due to fluid layering around

the CNT.

We have investigated the liquid flow of argon through a CNT membrane using two fluid reservoirs with density and temperature control only. We simulated three density (pressure) differences and compared the results with hydrodynamic predictions, NS solutions and an MD simulation of argon flow through a hydrophillic nanopore reported in [165]. The hydrodynamic predictions are based upon assumptions of fluid density and viscosity inside a CNT that are difficult to define for a highly confined fluid. The predicted hydrodynamic velocity profiles, with and without slip terms, and those from the NS solutions did not match the results obtained from our MD simulation. This is because the fluid inside a CNT forms a well-ordered structure, which leads to transport mechanisms that are different from those under bulk (macroscale) conditions. Therefore, for this flow configuration, and certainly for smaller diameter CNTs, we can no longer rely on continuum-based solutions to accurately predict the fluid behaviour.

The effect of changing the interaction strength between the liquid and CNT was also examined using the same simulation setup. We found that as the CNT becomes more hydrophobic it increases the flow rate of argon under the same pressure difference. The flow through the hydrophillic nanopore [165] produced the smallest mass flow rate, while a CNT with the weakest solid-liquid interaction led to the largest flow rate. Experimental reports indicate that, as the solid-liquid interaction decreases, the surface friction decreases [168] which is in agreement with our results. We found that a more hydrophobic CNT led to lower fluid pressure losses (friction) along its length.

Results of MD simulations of pressure-driven water transport through (7,7) CNTs, with lengths ranging from 2.5 nm to 50 nm have been reported. A constant pressure difference was applied in each simulation, created using a PID controller and a pressure flux technique, as described previously. We found that under the same applied pressure difference an increase in CNT length had a negligible effect on the mass flow rate and fluid flow velocity. This means that longer

CNTs have higher flow enhancement factors. For a fixed pressure difference, the flow enhancement factor is directly proportional only to the CNT length. Axial profiles of hydrodynamic properties demonstrated that entrance and exit effects are significant in this flow problem. Large viscous losses are experienced in these regions, and are shown by dips in the axial pressure profiles. In longer CNTs, central "developed" regions are present that are effectively frictionless. These regions extend proportionally with the length of the CNT, resulting in mass flow rates that are seemingly unaffected by an increase in CNT length.

Finally, we have shown, using MD simulations, how changing the number of vacancy site defects within the surface of a (7,7) CNT affects the internal flow dynamics of water. A pressure difference was generated across a 25 nm CNT by the same techniques as described above. We found that including vacancy site defects reduces the fluid velocity and mass flow rate rate considerably. As the number of defects increases, the velocity and mass flow rate decrease. Mass flow rate is also affected by a reduction in the overall fluid density in the CNT caused by the presence of the defects. The inclusion of vacancy sites leads to greater pressure losses as the fluid travels along the CNT, which reduces the overall fluid velocity. Flow enhancement factors are reduced significantly with increasing numbers of defects, which may account to some extent for the over-prediction of fluid flow rates in MD simulations (using pristine CNTs) when compared with experimental results.

CNTs have created an exciting new field of fluid dynamics where conventional assumptions (e.g. continuum assumption) no longer apply and we must re-think how fluids behave when under extreme confinement. MD will continue to provide vital results which will compliment advances in physical experiments enabling more observations and measurements to be produced. CNTs have a huge potential in the future of nanoscale fluid dynamics, particularly for desalination applications. The efficient transport of water through CNTs, owing to their low friction, and their reported salt rejection capabilities make them, in theory, a

viable alternative to existing membrane designs.

7.1 Future work

This research opens a number of avenues for future investigations:

1. A necessary requirement is the inclusion of a more accurate electrostatic interaction technique in the OpenFOAM code. This will allow accurate MD simulations of systems with inhomogeneous charge distributions to be performed. The recommended electrostatics method is the particle-mesh Ewald technique, which has been adapted for systems with periodicity in two-dimensions [171]. This would then enable our simulation model for pressure-driven flow to be applied to water/ion mixtures to evaluate, e.g., the salt rejection performance of CNT membranes. Our simulation model is robust and can be adapted to a variety of applications, such as desalination, where the presence of periodic boundary conditions cannot accurately model the effect of concentration polarisation [69].

2. It would be useful to perform MD simulations of pressure-driven water flow through CNTs (embedded within a membrane) with a variety of defects, such as functionalisation of the inner wall and tips (which would also require an accurate electrostatics algorithm). This work would provide further insight into which type of CNT defects most affect the water mass flow rate and salt rejection capability. Specific functional groups have been shown to improve salt rejection capabilities of CNT membranes with only a small decrease in the resulting water flow rate [69].

3. The existing MD solver should be adapted to exploit graphical processing units (GPUs) to handle the most computationally demanding aspects of the MD algorithm, i.e. force computations. This step alone accounts for 70% of the entire workload of an MD simulation. By dispatching this

function on a GPU, rather than a standard central processing unit (CPU), we can reduce the computational demands of MD significantly [172–176]. The CPU would function normally until the force computation step, at which point the CPU would pass the particle positions to the GPU and the forces would be calculated via, e.g., the OpenMM library [172] that was created specifically for molecular modelling on GPUs. The calculated forces would then be passed back to the CPU (OpenFOAM) and the MD algorithm would advance as normal. The OpenMM library includes accurate electrostatic interaction algorithms as standard, but only for fully periodic systems. OpenMM cannot be used independently to run MD simulations and the coupling with OpenFOAM requires coding at the GPU level which is very difficult and time-consuming. A deep understanding of the complex GPU memory hierarchy is also required since communication will involve passing large amounts of data back and forth between the GPU and CPU.

4. The computational gains from using GPUs for MD would potentially allow us to simulate CNTs that are micrometres in length, bridging the gap between length scales used in MD simulations and physical experiments. This would determine at which point, if any, the flow rate decreases with increasing CNT length.

5. Performing a number of MD simulations using a selection of boundary conditions to generate pressure driven water flow through CNTs would identify the effect that different boundary conditions have on mass flow rate and pressure/density distributions across the domain. This would provide information on which technique is most appropriate for this flow problem, as a wide variety of techniques are adopted in the literature and no single study has compared their performance.

6. Improved water-carbon Lennard-Jones interaction parameters are required for each water model. More specifically, it would be possible to use the

techniques of Werder *et al.* [106] to fit the parameters for the TIP4P/2005, which in a recent study has been shown to be the most promising rigid, non-polarisable model [177].

7. Currently the only way to reduce statistical noise associated with MD measurements in OpenFOAM is to use long averaging periods (large numbers of time steps). Future developments may include more elegant approaches to reduce these fluctuations, such as the field estimator technique [178] or variance reduction [179], which may enable meaningful averages to be obtained over shorter averaging periods.

8. Extend the external flow case presented in this work to investigate superhydrophobic surfaces (most likely CNTs) which will have industrial applications in drag reduction of sea vessels and aircraft.

9. Work more closely with experimental researchers on a joint project investigating desalination membranes of the future. The limitation in the application of CNT membranes lies in their manufacturing process: large scale production of membranes containing CNTs with diameters less then 1 nm may not be possible. However, larger diameter CNTs, which are easier to manufacture, can be used for desalination by tuning their functionalisation which enhances their salt rejection capabilities. MD would be used to establish which characteristics (e.g. types of functionalisation groups, boron nitiride nanotubes rather than CNTs) will produce the most efficient desalination membranes.

References

[1] M. K. Borg, G. B. Macpherson, and J. M. Reese. Controllers for imposing continuum-to-molecular boundary conditions in arbitrary fluid flow geometries. *Molecular Simulation*, 36(10):745 – 757, 2010.

[2] J. K. Holt, H. G. Park, Y. Wang, M. Stadermann, A. B. Artyukhin, C. P. Grigoropoulos, A. Noy, and O. Bakajin. Fast mass transport through sub-2-nanometer carbon nanotubes. *Science*, 312(5776):1034–1037, 2006.

[3] D. Mattia and Y. Gogotsi. Static and dynamic behavior of liquids inside carbon nanotubes. *Microfluidics and Nanofluidics*, 5:289–305, 2008.

[4] A.K. and Soper. The radial distribution functions of water and ice from 220 to 673 k and at pressures up to 400 mpa. *Chemical Physics*, 258(2-3):121 – 137, 2000.

[5] J. A. Thomas and A. J. H. McGaughey. Density, distribution, and orientation of water molecules inside and outside carbon nanotubes. *Journal of Chemical Physics*, 128(8):084715, 2008.

[6] W. Tang and S. G. Advani. Drag on a nanotube in uniform liquid argon flow. *Journal of Chemical Physics*, 125(17):1–8, 2006.

[7] J. C. T. Eijkel and A. van den Berg. Nanofluidics: what is it and what can we expect from it? *Microfluidics and Nanofluidics*, 1(3):249–267, 2005.

[8] T.R. Hennessy M. Ciofalo, M.W. Collins. Modelling nanoscale fluid dynamics and transport in physiological flows. *Medical Engineering & Physics*, 18(6):437–451, 1996.

[9] D. Mijatovic, J.C.T. Eijkel, and A. Berg van den. Technologies for nanofluidic systems: top-down vs. bottom-up — a review. *Lab on a Chip*, 5(5):492–500, 2005.

[10] K. P. Travis, B. D. Todd, and D. J. Evans. Departure from navier-stokes hydrodynamics in confined liquids. *Physical Review E*, 55(4):4288–4295, 1997.

[11] J. A. Thomas and A. J. H. McGaughey. Water flow in carbon nanotubes: transition to subcontinuum transport. *Physical Review Letters*, 102(18):184502, 2009.

[12] Z. Wang, N. Koratkar, L. Ci, and P. M. Ajayan. Combined micro-/nanoscale surface roughness for enhanced hydrophobic stability in carbon nanotube arrays. *Applied Physics Letters*, 90(14):143117, 2007.

[13] G. Hu and D. Li. Multiscale phenomena in microfluidics and nanofluidics. *Chemical Engineering Science*, 62(13):3443 – 3454, 2007.

[14] C. Choong, W. I. Milne, and K. B. K. Teo. Review: carbon nanotube for microfluidic lab-on-a-chip application. *International Journal of Material Forming*, 1(2):117–125, 2008.

[15] K. P. Lee, T. C. Arnot, and D. Mattia. A review of reverse osmosis membrane materials for desalination-development to date and future potential. *Journal of Membrane Science*, 370(1-2):1–22, 2011.

[16] H. Daiguji. Ion transport in nanofluidic channels. *Chemical Society Reviews*, 39: 901–911, 2010.

[17] A. Favre-Reguillon, G. Lebuzit, J. Foos, A. Guy, M. Draye, and M. Lemaire. Selective concentration of uranium from seawater by nanofiltration. *Industrial & Engineering Chemistry Research*, 42(23):5900–5904, 2003.

[18] S. Ghosh, A. K. Sood, and N. Kumar. Carbon nanotube flow sensors. *Science*, 299(5609):1042–1044, 2003.

[19] M. K. Borg. *Hybrid Molecular-Continuum Modelling of Nano-Scale Flows*. University of Strathclyde, 2010.

[20] D. C. Rapaport. *The art of molecular dynamics simulation*. Cambridge, 2nd edition, 2004.

[21] L. Verlet. Computer "experiments" on classical fluids. i. thermodynamical properties of lennard-jones molecules. *Physical Review*, 159:98–103, 1967.

[22] D.C. Allen and D.J. Tildesley. *Computer simulation of liquids*. Oxford University Press, 2nd edition, 1987.

[23] A. Dullweber, B. Leimkuhler, and R. McLachlan. Symplectic splitting methods for rigid body molecular dynamics. *Journal of Chemical Physics*, 107(15):5840–5851, 1997.

[24] Jean-Paul Ryckaert, Giovanni Ciccotti, and Herman J. C. Berendsen. Numerical integration of the cartesian equations of motion of a system with constraints: molecular dynamics of n-alkanes. *Journal of Computational Physics*, 23(3):327 – 341, 1977.

[25] OpenFOAM Foundation. http://www.openfoam.org, 2011.

[26] G. B. Macpherson, N. Nordin, and H. G. Weller. Particle tracking in unstructured, arbitrary polyhedral meshes for use in cfd and molecular dynamics. *Communications in Numerical Methods in Engineering*, 25(3):263 – 273, 2009.

[27] G. B. Macpherson and J. M. Reese. Molecular dynamics in arbitrary geometries: Parallel evaluation of pair forces. *Molecular Simulation*, 34(1):97 – 115, 2008.

[28] E. L. Pollock and Jim Glosli. Comments on p3m, fmm, and the ewald method for large periodic coulombic systems. *Computer Physics Communications*, 95(2-3): 93 – 110, 1996.

[29] A. Y. Toukmaji and J. A. Board. Ewald summation techniques in perspective: a survey. *Computer Physics Communications*, 95(2-3):73 – 92, 1996.

[30] Markus Deserno and Christian Holm. How to mesh up ewald sums. i. a theoretical and numerical comparison of various particle mesh routines. *Journal of Chemical Physics*, 109(18):7678–7693, 1998.

[31] DL_POLY_2 User Manual. http://www.cse.scitech.ac.uk/ccg/software/dl_poly/, 2011.

[32] NAMD. http://www.ks.uiuc.edu/research/namd/, 2011.

[33] LAMMPS. http://lammps.sandia.gov/, 2001.

[34] Amber. http://ambermd.org/, 2011.

[35] T. A. Andrea, W. C. Swope, and H. C. Andersen. The role of long ranged forces in determining the structure and properties of liquid water. 79(9):4576–4584, 1983.

[36] D. van der Spoel and P. J. van Maaren. The origin of layer structure artifacts in simulations of liquid water. *Journal of Chemical Theory and Computation*, 2(1): 1–11, 2006.

[37] S. V. Nedea, A. J. H. Frijns, A. A. van Steenhoven, A. J. Markvoort, and P. A. J. Hilbers. Hybrid method coupling molecular dynamics and monte carlo simulations to study the properties of gases in microchannels and nanochannels. *Physical Review E*, 72(1):016705, Jul 2005.

[38] T. Werder, J.H. Walther, and P. Koumoutsakos. Hybrid atomistic-continuum method for the simulation of dense fluid flows. *Journal of Computational Physics*, 205(1):373 – 390, 2005.

[39] T. Yen, C. Soong, and P. Tzeng. Hybrid molecular dynamics-continuum simulation for nano/mesoscale channel flows. *Microfluidics and Nanofluidics*, 3(6): 665–675, 2007.

[40] Q. Li and G. He. An atomistic-continuum hybrid simulation of fluid flows over superhydrophobic surfaces. *Biomicrofluidics*, 3(2):022409, 2009.

[41] W. Ren and W. E. Heterogeneous multiscale method for the modeling of complex fluids and micro-fluidics. *Journal of Computational Physics*, 204(1):1 – 26, 2005.

[42] G. B. Macpherson. *Molecular Dynamics Simulation in Arbitrary Geometries for Nanoscale Fluid Mechanics*. PhD thesis, 2008.

[43] S. Iijima. Helical microtubules of graphitic carbon. *Nature*, 354(6348):56–58, 1991.

[44] A. Alexiadis and S. Kassinos. Molecular simulation of water in carbon nanotubes. *Chemical Reviews*, 108(12):5014–5034, 2008.

[45] S. Iijima and T. Ichihashi. Single-shell carbon nanotubes of 1-nm diameter. *Nature*, 363(6430):603–605, 1993.

[46] M. S. Dresselhaus, G. Dresselhaus, J. C. Charlier, and E. Hernndez. Electronic, thermal and mechanical properties of carbon nanotubes. *Philosophical Transactions of the Royal Society of London. Series A:Mathematical, Physical and Engineering Sciences*, 362(1823):2065–2098, 2004.

[47] V. N. Popov. Carbon nanotubes: properties and application. *Materials Science and Engineering: R: Reports*, 43(3):61 – 102, 2004.

[48] R. H. Baughman, A. A. Zakhidov, and W. A. de Heer. Carbon nanotubes–the route toward applications. *Science*, 297(5582):787–792, 2002.

[49] E. Joselevich, H. Dai, J. Liu, K. Hata, and A. H Windle. Carbon nanotube synthesis and organization. *Carbon Nanotubes*, 111(2008):101–164, 2008.

[50] P. J. F. Harris, E. Hernndez, and B. I. Yakobson. Carbon nanotubes and related structures: New materials for the twenty-first century. 72(3):415–415, 2004.

[51] J. W. Seo, E. Couteau, P. Umek, K. Hernadi, P. Marcoux, B. Luki, C. Mik, M. Milas, R. Gal, and L. Forr. Synthesis and manipulation of carbon nanotubes. *New Journal of Physics*, 5(1):120, 2003.

[52] J. K. Holt. Carbon nanotubes and nanofluidic transport. *Advanced Materials*, 21 (35):3542–3550, 2009.

[53] D. Mattia, M. P. Rossi, B. M. Kim, G. Korneva, H. H. Bau, and Y. Gogotsi. Effect of graphitization on the wettability and electrical conductivity of cvd-carbon nanotubes and films. *Journal of Physical Chemistry B*, 110(20):9850–9855, 2006.

[54] S. A. Miller, V. Y. Young, and C. R. Martin. Electroosmotic flow in template-prepared carbon nanotube membranes. *Journal of the American Chemical Society*, 123(49):12335–12342, 2001.

[55] B. J. Hinds, N. Chopra, T. Rantell, R. Andrews, V. Gavalas, and L. G. Bachas. Aligned multiwalled carbon nanotube membranes. *Science*, 303(5654):62–65, 2004.

[56] M. Majumder, N. Chopra, R. Andrew, and B. J. Hinds. Nanoscale hydrodynamics: enhanced flow in carbon nanotubes. *Nature*, 438:44, 2005.

[57] M. Majumder, N. Chopra, and B. J. Hinds. Mass transport through carbon nanotube membranes in three different regimes: Ionic diffusion and gas and liquid flow. *ACS Nano*, 5(5):3867–3877, 2011.

[58] J. K. Holt, A. Noy, T. Huser, D. Eaglesham, and O. Bakajin. Fabrication of a carbon nanotube-embedded silicon nitride membrane for studies of nanometer-scale mass transport. *Nano Letters*, 4(11):2245–2250, 2004.

[59] F. Fornasiero, H. G. Park, J. K. Holt, M. Stadermann, C. P. Grigoropoulos, A. Noy, and O. Bakajin. Ion exclusion by sub-2-nm carbon nanotube pores. *Proceedings of the National Academy of Sciences*, 105(45):17250–17255, 2008.

[60] C. Lam, J. T. James, R. McCluskey, S. Arepalli, and R. L. Hunter. A review of carbon nanotube toxicity and assessment of potential occupational and environmental health risks. *Critical Reviews in Toxicology*, 36(3):189–217, 2006.

[61] W. Wenseleers, S. Cambr, J. ?ulin, A. Bouwen, and E. Goovaerts. Effect of water filling on the electronic and vibrational resonances of carbon nanotubes: Characterizing tube opening by raman spectroscopy. *Advanced Materials*, 19(17): 2274–2278, 2007.

[62] S. Cambré, B. Schoeters, S. Luyckx, E. Goovaerts, and W. Wenseleers. Experimental observation of single-file water filling of thin single-wall carbon nanotubes down to chiral index (5,3). *Physical Review Letters*, 104(20):207401, 2010.

[63] S. Sinha, M. P. Rossi, D. Mattia, Y. Gogotsi, and H. H. Bau. Induction and measurement of minute flow rates through nanopipes. 19(1):013603, 2007.

[64] S. S. Ray, P. Chando, and A. L. Yarin. Enhanced release of liquid from carbon nanotubes due to entrainment by an air layer. *Nanotechnology*, 20(9):095711, 2009.

[65] M. Whitby, L. Cagnon, M. Thanou, and N. Quirke. Enhanced fluid flow through nanoscale carbon pipes. *Nano Letters*, 8(9):2632–2637, 2008.

[66] M. Majumder, N. Chopra, and B. J. Hinds. Effect of tip functionalization on transport through vertically oriented carbon nanotube membranes. *Journal of the American Chemical Society*, 127(25):9062–9070, 2005.

[67] F. Du, L. Qu, Z. Xia, L. Feng, and L. Dai. Membranes of vertically aligned superlong carbon nanotubes. *Langmuir*, 27(13):8437–8443, 2011.

[68] X. Qin, Q. Yuan, Y. Zhao, S. Xie, and Z. Liu. Measurement of the rate of water translocation through carbon nanotubes. *Nano Letters*, 11(5):2173–2177, 2011.

[69] B. Corry. Water and ion transport through functionalised carbon nanotubes: implications for desalination technology. *Energy & Environmental Science*, 4: 751–759, 2011.

[70] M. Majumder and B. Corry. Anomalous decline of water transport in covalently modified carbon nanotube membranes. *Chemical Communications*, 47:7683–7685, 2011.

[71] A. Striolo. Water self-diffusion through narrow oxygenated carbon nanotubes. *Nanotechnology*, 18(47):475704, 2007.

[72] D. B. Mawhinney, V. Naumenko, A. Kuznetsova, J. T. Yates, J. Liu, and R. E. Smalley. Surface defect site density on single walled carbon nanotubes by titration. *Chemical Physics Letters*, 324(1-3):213 – 216, 2000.

[73] T. W. Ebbesen. Wetting, filling and decorating carbon nanotubes. *Journal of Physics and Chemistry of Solids*, 57(6-8):951 – 955, 1996. Proceeding of the 8th International Symposium on Intercalation Compounds.

[74] A.J. Stone and D.J. Wales. Theoretical studies of icosahedral c60 and some related species. *Chemical Physics Letters*, 128(5-6):501 – 503, 1986.

[75] Q. Lu and B. Bhattacharya. Effect of randomly occurring stonewales defects on mechanical properties of carbon nanotubes using atomistic simulation. *Nanotechnology*, 16(4):555, 2005.

[76] S. Li, P. Xiu, H. Lu, X. Gong, K. Wu, R. Wan, and H. Fang. Water permeation across nanochannels with defects. *Nanotechnology*, 19(10):105711, 2008.

[77] A. Hashimoto, K. Suenaga, A. Gloter, K. Urita, and S. Iijima. Direct evidence for atomic defects in graphene layers. *Nature*, 430(7002):870–873, 2004.

[78] M. Yang, V. Koutsos, and M. Zaiser. Size effect in the tensile fracture of single-walled carbon nanotubes with defects. *Nanotechnology*, 18(15):155708, 2007.

[79] M. Terrones, A. Filho, and A. Rao. Doped carbon nanotubes: Synthesis, characterization and applications. 111:531–566, 2008.

[80] J. H. Walther, T. Werder, R. L. Jaffe, P. Gonnet, M. Bergdorf, U. Zimmerli, and P. Koumoutsakos. Water-carbon interactions iii: The influence of surface and fluid impurities. *Phys. Chem. Chem. Phys.*, 6:1988–1995, 2004.

[81] E. M. Kotsalis, E. Demosthenous, J. H. Walther, S. C. Kassinos, and P. Koumoutsakos. Wetting of doped carbon nanotubes by water droplets. *Chemical Physics Letters*, 412(4-6):250–254, 2005.

[82] TubeGen Online Version 3.3. http://turin.nss.udel.edu/research/tubegenonline.html.

[83] G. B. Macpherson, M. K. Borg, and J. M. Reese. Generation of initial molecular dynamics configurations in arbitrary geometries and in parallel. *Molecular Simulation*, 33(15):1199 – 1212, 2008.

[84] J. K. Holt. Methods for probing water at the nanoscale. *Microfluidics and Nanofluidics*, 5(4):425–442, 2008.

[85] B. Guillot. A reappraisal of what we have learnt during three decades of computer simulations on water. *Journal of Molecular Liquids*, 101(1-3):219 – 260, 2002.

[86] H. J. C. Berendsen, J. P. M. Postma, W. F. van Gunsteren, and J. Hermans. Interaction models for water in relation to protein hydration. *Intermolecular Forces*, pages 331–342, 1981.

[87] H. J. C Berendsen, J. R. Grigera, and T. P. Straatsma. The missing term in effective pair potentials. *Journal of Physical Chemistry*, 91(24):6269–6271, 1987.

[88] W. L. Jorgensen, J. Chandrasekhar, J. D. Madura, R. W. Impey, and M. L. Klein. Comparison of simple potential functions for simulating liquid water. *Journal of Chemical Physics*, 79(2):926–935, 1983.

[89] W. L. Jorgensen and J. D. Madura. Temperature and size dependence for monte carlo simulations of tip4p water. *Molecular Physics*, 56(6):1381–1392, 1985.

[90] M. W. Mahoney and W. L. Jorgensen. A five-site model for liquid water and the reproduction of the density anomaly by rigid, nonpolarizable potential functions. *Journal of Chemical Physics*, 112(20):8910–8922, 2000.

[91] C. Vega, E. Sanz, and J. L. F. Abascal. The melting temperature of the most common models of water. *Journal of Chemical Physics*, 122(11):114507, 2005.

[92] H. Yu and W. F. van Gunsteren. Accounting for polarization in molecular simulation. *Computer Physics Communications*, 172(2):69 – 85, 2005.

[93] J. A. Thomas and A. J. H. McGaughey. Reassessing fast water transport through carbon nanotubes. *Nano Letters*, 8(9):2788–2793, 2008.

[94] J. A. Thomas, A. J. H. McGaughey, and O. Kuter-Arnebeck. Pressure-driven water flow through carbon nanotubes: insights from molecular dynamics simulation. *International Journal of Thermal Sciences*, 49(2):281–289, 2010.

[95] B. Corry. Designing carbon nanotube membranes for efficient water desalination. *Journal of Physical Chemistry B*, 112(5):1427–1434, 2008.

[96] H.A. Zambrano, J.H. Walther, P. Koumoutsakos, and I.F. Sbalzarini. Thermophoretic motion of water nanodroplets confined inside carbon nanotubes. *Nano Letters*, 9(1):66–71, 2009.

[97] J. Shiomi and S. Maruyama. Water transport inside a single-walled carbon nanotube driven by a temperature gradient. *Nanotechnology*, 20(5):055708 (5pp), 2009.

[98] G. Zuo, R. Shen, S. Ma, and W. Guo. Transport properties of single-file water molecules inside a carbon nanotube biomimicking water channel. *ACS Nano*, 4 (1):205–210, 2010.

[99] M. E. Suk and N. R. Aluru. Water transport through ultrathin graphene. *Journal of Physical Chemistry Letters*, 1(10):1590–1594, 2010.

[100] J. L. Rivera and F. W. Starr. Rapid transport of water via a carbon nanotube syringe. *Journal of Physical Chemistry C*, 114(9):3737–3742, 2010.

[101] B. Mukherjee, P. K. Maiti, C. Dasgupta, and A. K. Sood. Single-file diffusion of water inside narrow carbon nanorings. *ACS Nano*, 4(2):985–991, 2010.

[102] T. A. Beu. Molecular dynamics simulations of ion transport through carbon nanotubes. i. influence of geometry, ion specificity, and many-body interactions. *Journal of Chemical Physics*, 132(16):164513, 2010.

[103] J. Su and H. Guo. Control of unidirectional transport of single-file water molecules through carbon nanotubes in an electric field. *ACS Nano*, 5(1):351–359, 2011.

[104] M. D. Ma, L. Shen, J. Sheridan, J. Zhe Liu, Chao Chen, and Quanshui Zheng. Friction of water slipping in carbon nanotubes. *Physical Review E*, 83(3):036316, Mar 2011.

[105] W. D. Nicholls, M. K. Borg, D. A. Lockerby, and J. M. Reese. Water transport through (7,7) carbon nanotubes of different lengths using molecular dynamics. *Microfluidics and Nanofluidics*, 12:257–264, 2012.

[106] T. Werder, J. H. Walther, R. Jaffe, T. Halicioglu, and P. Koumoutsakos. On the water-carbon interaction for use in molecular dynamics simulations of graphite and carbon nanotubes. *Journal of Physical Chemistry B*, 107(41):1345–1352, 2003.

[107] J. Wang, Y. Zhu, J. Zhou, and X. Lu. Diameter and helicity effects on static properties of water molecules confined in carbon nanotubes. *Physical Chemistry Chemical Physics*, 6:829–835, 2004.

[108] M. J. Longhurst and N. Quirke. The environmental effect on the radial breathing mode of carbon nanotubes in water. *Journal of Chemical Physics*, 124(23):234708, 2006.

[109] S. Joseph and N. R. Aluru. Why are carbon nanotubes fast transporters of water? *Nano Letters*, 8(2):452–458, 2008.

[110] A. Alexiadis and S. Kassinos. Influence of water model and nanotube rigidity on the density of water in carbon nanotubes. *Chemical Engineering Science*, 63(10): 2793 – 2797, 2008.

[111] R. Wan, H. Lu, J. Li, J. Bao, J. Hu, and H. Fang. Concerted orientation induced unidirectional water transport through nanochannels. *Physical Chemistry Chemical Physics*, 11:9898–9902, 2009.

[112] C. Dellago and G. Hummer. Kinetics and mechanism of proton transport across membrane nanopores. *Physical Review Letters*, 97(24):245901, 2006.

[113] J. Kofinger, G. Hummer, and C. Dellago. Single-file water in nanopores. *Physical Chemistry Chemical Physics*, 13:15403–15417, 2011.

[114] B. Mukherjee, P. K. Maiti, C. Dasgupta, and A. K. Sood. Strong correlations and fickian water diffusion in narrow carbon nanotubes. *Journal of Chemical Physics*, 126(12):124704, 2007.

[115] G. Hummer, J. C. Rasaiah, and J. P. Noworyta. Water conduction through the hydrophobic channel of a carbon nanotube. *Nature*, 414:188–190, 2001.

[116] W. H. Noon, K. D. Ausman, R. E. Smalley, and J. Ma. Helical ice-sheets inside carbon nanotubes in the physiological condition. *Chemical Physics Letters*, 355 (5-6):445 – 448, 2002.

[117] R. J. Mashl, S. Joseph, N. R. Aluru, and E. Jakobsson. Anomalously immobilized water: A new water phase induced by confinement in nanotubes. *Nano Letters*, 3(5):589–592, 2003.

[118] Y. Liu, Q. Wang, T. Wu, and L. Zhang. Fluid structure and transport properties of water inside carbon nanotubes. *Journal of Chemical Physics*, 123(23):234701, 2005.

[119] A. Alexiadis and S. Kassinos. The density of water in carbon nanotubes. *Chemical Engineering Science*, 63(8):2047–2056, 2008.

[120] S. C. Gay, E. J. Smith, and A. D. J. Haymet. Dynamics of melting and stability of ice 1h: Molecular-dynamics simulations of the SPC/E model of water. *Journal of Chemical Physics*, 116(20):8876–8880, 2002.

[121] S. Bernardi, B. D. Todd, and D. J. Searles. Thermostating highly confined fluids. *Journal of Chemical Physics*, 132(24):244706, 2010.

[122] J. H. Walther, R. Jaffe, T. Halicioglu, and P. Koumoutsakos. Carbon nanotubes in water: structural characteristics and energetics. *Journal of Physical Chemistry B*, 105(41):9980–9987, 2001.

[123] F. Zhu, E. Tajkhorshid, and K. Schulten. Pressure-induced water transport in membrane channels studied by molecular dynamics. *Biophysical Journal*, 83(1): 154 – 160, 2002.

[124] J. Garate, N. J. English, and J. M. D MacElroy. Static and alternating electric field and distance-dependent effects on carbon nanotube-assisted water self-diffusion across lipid membranes. *Journal of Chemical Physics*, 131(11):114508, 2009.

[125] R. Radhakrishnan and K. E. Gubbins. Quasi-one-dimensional phase transitions in nanopores: Pore-pore correlation effects. *Physical Review Letters*, 79(15): 2847–2850, Oct 1997.

[126] J. Tomlinson-Phillips, J. Davis, D. Ben-Amotz, D. Spangberg, L. Pejov, and K. Hermansson. Structure and dynamics of water dangling oh bonds in hydrophobic hydration shells. comparison of simulation and experiment. *Journal of Physical Chemistry A*, 115(23):6177–6183, 2011.

[127] A. Luzar and D. Chandler. Hydrogen bond kinetics in liquid water. *Nature*, 379 (6560):55–57, 1996.

[128] D. Laage and J. T. Hynes. A molecular jump mechanism of water reorientation. *Science*, 311(5762):832–835, 2006.

[129] A. Alexiadis and S. Kassinos. Self-diffusivity, hydrogen bonding and density of different water models in carbon nanotubes. *Molecular Simulation*, 34(7):671–678, 2008.

[130] F N Keutsch and R J Saykally. Water clusters: Untangling the mysteries of the liquid, one molecule at a time. *Proceedings of the National Academy of Sciences of the United States of America*, 98(19):10533–10540, 2001.

[131] L. Ojamaee and K. Hermansson. Ab initio study of cooperativity in water chains: Binding energies and anharmonic frequencies. *Journal of Physical Chemistry*, 98 (16):4271–4282, 1994.

[132] A. Kalra, S. Garde, and G. Hummer. Osmotic water transport through carbon nanotube membranes. *Proceedings of the National Academy of Sciences of the United States of America*, 100(18):10175–10180, 2003.

[133] I. Hanasaki and A. Nakatani. Flow structure of water in carbon nanotubes: Poiseuille journal article or plug-like? *Journal of Chemical Physics*, 124(14): 144708, 2006.

[134] Z. Xiao-Yan and L. Hang-Jun. The structure and dynamics of water inside armchair carbon nanotube. *Chinese Physics*, 16(2):335, 2007.

[135] C. Song and B. Corry. Intrinsic ion selectivity of narrow hydrophobic pores. *Journal of Physical Chemistry B*, 113(21):7642–7649, 2009.

[136] M. E. Suk, A. V. Raghunathan, and N. R. Aluru. Fast reverse osmosis using boron nitride and carbon nanotubes. *Applied Physics Letters*, 92(13):133120, 2008.

[137] N. G. Hadjiconstantinou, A. L. Garcia, M. Z. Bazant, and G. He. Statistical error in particle simulations of hydrodynamic phenomena. *Journal of Computational Physics*, 187(1):274 – 297, 2003.

[138] M. W. Tysanner and A. L. Garcia. Measurement bias of fluid velocity in molecular simulations. *Journal of Computational Physics*, 196(1):173 – 183, 2004.

[139] M. Shibahara and K. Takeuchi. A molecular dynamics study on the effects of nanostructural clearances on thermal resistance at a liquid water-solid interface. *Journal of Physics: Conference Series*, 191(1):012008, 2009.

[140] J. H. Irving and J. G. Kirkwood. The statistical mechanical theory of transport processes. iv. the equations of hydrodynamics. 18(6):817–829, 1950.

[141] S.T. O'Connell and P.A. Thompson. Molecular dynamics—continuum hybrid computations: a tool for studying complex fluid flows. *Physical Review E*, 52(6): R5792–R5795, 1995.

[142] R. Delgado-Buscalioni and P. V. Coveney. Continuum-particle hybrid coupling for mass, momentum, and energy transfers in unsteady fluid flow. *Physical Review E*, 67(4):1–13, 2003.

[143] E. G. Flekkøy, R. Delgado-Buscalioni, and P. V. Coveney. Flux boundary conditions in particle simulations. *Physical Review E*, 72(2):026703, 2005.

[144] H. J. C. Berendsen, J. P. M. Postma, W. F. van Gunsteren, A. DiNola, and J. R. Haak. Molecular dynamics with coupling to an external bath. *Journal of Chemical Physics*, 81(8):3684–3690, 1984.

[145] A. Striolo. The mechanism of water diffusion in narrow carbon nanotubes. *Nano Letters*, 6(4):633–639, 2006.

[146] J. Koplik, J. R. Banavar, and J. F. Willemsen. Molecular dynamics of poiseuille flow and moving contact lines. *Physical Review Letters*, 60(13):1282–1285, 1988.

[147] J. Li, D. Liao, and S. Yip. Coupling continuum to molecular-dynamics simulation: Reflecting particle method and the field estimator. *Phys. Rev. E*, 57(6):7259–7267, Jun 1998.

[148] C. Huang, K. Nandakumar, P. Y. K. Choi, and L. W. Kostiuk. Molecular dynamics simulation of a pressure-driven liquid transport process in a cylindrical nanopore using two self-adjusting plates. *Journal of Chemical Physics*, 124(23): 1–8, 2006.

[149] C. Huang, P. Y. K. Choi, K. Nandakumar, and L. W. Kostiuk. Investigation of entrance and exit effects on liquid transport through a cylindrical nanopore. *Physical Chemistry Chemical Physics (Incorporating Faraday Transactions)*, 10: 186–192, 2008.

[150] M. Firouzi, K. M. Nezhad, T. T. Tsotsis, and M. Sahimi. Molecular dynamics simulations of transport and separation of carbon dioxide–alkane mixtures in carbon nanopores. *The Journal of Chemical Physics*, 120(17):8172–8185, 2004.

[151] R. Delgado-Buscalioni and P. V. Coveney. Usher: An algorithm for particle insertion in dense fluids. *Journal of Chemical Physics*, 119(2):978–987, 2003.

[152] G. D. Fabritiis, R. Delgado-Buscalioni, and P. V. Coveney. Energy controlled insertion of polar molecules in dense fluids. *Journal of Chemical Physics*, 121 (24):12139–12142, 2004.

[153] G. D. Fabritiis, R. Delgado-Buscalioni, and P. V. Coveney. Multiscale modeling of liquids with molecular specificity. *Physical Review Letters*, 97(13):134501, 2006.

[154] G. Nagayama and P. Cheng. Effects of interface wettability on microscale flow by molecular dynamics simulation. *International Journal of Heat and Mass Transfer*, 47(3):501 – 513, 2004.

[155] K. P. Travis and K. E. Gubbins. Poiseuille flow of lennard-jones fluids in narrow slit pores. *Journal of Chemical Physics*, 112(4):1984–1994, 2000.

[156] J. L. Xu and Z. Q. Zhou. Molecular dynamics simulation of liquid argon flow at platinum surfaces. *Heat and Mass Transfer*, 40:859–869, 2004.

[157] A. Ziarani and A. Mohamad. A molecular dynamics study of perturbed poiseuille flow in a nanochannel. *Microfluidics and Nanofluidics*, 2:12–20, 2006.

[158] S. Supple and N. Quirke. Rapid imbibition of fluids in carbon nanotubes. *Physical Review Letters*, 90(21):214501, May 2003.

[159] A. I. Skoulidas, D. M. Ackerman, J. K. Johnson, and D. S. Sholl. Rapid transport of gases in carbon nanotubes. *Physical Review Letters*, 89:185901, 2002.

[160] D. M. Ackerman, A. I. Skoulidas, D. S. Sholl, and J. K. Johnson. Diffusivities of argon and neon in carbon nanotubes. *Molecular Simulation*, 29(10-11):677–684, 2003.

[161] J. Cannon and O. Hess. Fundamental dynamics of flow through carbon nanotube membranes. *Microfluidics and Nanofluidics*, 8:21–31, 2010.

[162] J. Delhommelle and P. Millie. Inadequacy of the lorentz-berthelot combining rules for accurate predictions of equilibrium properties by molecular simulation. *Molecular Physics*, 99(8):619–625, 2001.

[163] Z. Mao and S. B. Sinnott. A computational study of molecular diffusion and dynamic flow through carbon nanotubes. *The Journal of Physical Chemistry B*, 104(19):4618–4624, 2000.

[164] National Institute of Standards and Technology (U.S.). NIST chemistry webbook [http://webbook.nist.gov/chemistry/].

[165] C. Huang, P. Y. K. Choi, K. Nandakumar, and L. W. Kostiuk. Comparative study between continuum and atomistic approaches of liquid flow through a finite length cylindrical nanopore. *Journal of Chemical Physics*, 126(22):224702, 2007.

[166] A. Mansouri, C. Scheuerman, S. Bhattacharjee, D. Y. Kwok, and L. W. Kostiuk. Transient streaming potential in a finite length microchannel. *Journal of Colloid and Interface Science*, 292(2):567 – 580, 2005.

[167] Z. Liu, S. Liang, C. Zhang, and N. Guan. Viscous heating for laminar liquid flow in microtubes. *Journal of Thermal Science*, 20:268–275, 2011. 10.1007/s11630-011-0469-2.

[168] H. Y. Wu and P. Cheng. An experimental study of convective heat transfer in silicon microchannels with different surface conditions. *International Journal of Heat and Mass Transfer*, 46(14):2547 – 2556, 2003.

[169] G. Portella, P. Pohl, and B. L. De Groot. Invariance of single-file water mobility in gramicidin-like peptidic pores as function of pore length. *Biophysical Journal*, 92(11):3930–3937, 2007.

[170] X. Peng, J. Jin, Y. Nakamura, T. Ohno, and I. Ichinose. Ultrafast permeation of water through protein-based membranes. *Nature Nanotechnology*, 4(6):353–357, 2009.

[171] M. Kawata and U. Nagashima. Particle mesh ewald method for three-dimensional systems with two-dimensional periodicity. *Chemical Physics Letters*, 340(1-2):165 – 172, 2001.

[172] M. S. Friedrichs, P. Eastman, V. Vaidyanathan, M. Houston, S. Legrand, A. L. Beberg, D. L. Ensign, C. M. Bruns, and V. S. Pande. Accelerating molecular dynamic simulation on graphics processing units. *Journal of Computational Chemistry*, 30(6):864–872, 2009.

[173] W. Liu, B. Schmidt, G. Voss, and W. Mller-Wittig. Molecular dynamics simulations on commodity GPUs with CUDA. *High Performance Computing*, pages 185 – 196, 2007.

[174] C. I. Rodrigues, D. J. Hardy, J. E. Stone, K. Schulten, and W. W. Hwu. GPU acceleration of cutoff pair potentials for molecular modeling applications. *Proceedings of the 5th conference on Computing frontiers*, pages 273–282, 2008.

[175] D. J. Hardy, J. E. Stone, and K. Schulten. Multilevel summation of electrostatic potentials using graphics processing units. *Parallel Computing*, 35(3):164 – 177, 2009. Revolutionary Technologies for Acceleration of Emerging Petascale Applications.

[176] John E. Stone, James C. Phillips, Peter L. Freddolino, David J. Hardy, Leonardo G. Trabuco, and Klaus Schulten. Accelerating molecular modeling applications with graphics processors. *Journal of Computational Chemistry*, 28 (16):2618–2640, 2007.

[177] C. Vega and J. L. F. Abascal. Simulating water with rigid non-polarizable models: a general perspective. *Physical Chemistry Chemical Physics*, 13:19663–19688, 2011.

[178] J. Eapen, J. Li, and S. Yip. Statistical field estimators for multiscale simulations. *Physical Review E*, 72:056712, 2005.

[179] H. A. Al-Mohssen and N. G. Hadjiconstantinou. Low-variance direct monte carlo simulations using importance weights. *ESAIM: Mathematical Modelling and Numerical Analysis*, pages 1069–1083, 2010.